Dynamic Strength of Silica Glasses at High Pressures and Strain Rates

Thesis by

Christian Kettenbeil

In Partial Fulfillment of the Requirements for the
Degree of
Doctor of Philosophy

CALIFORNIA INSTITUTE OF TECHNOLOGY
Pasadena, California

2019
Defended November 16, 2018

Christian Kettenbeil
ORCID: 0000-0003-0301-3678

ACKNOWLEDGEMENTS

I would like to express my sincere gratitude to my Ph.D. advisor, Prof. Guruswami Ravichandran, whose insight, guidance, and continued support were invaluable over the course of this work. I also want to thank Dr. Michael Mello, whose passion for experimental mechanics was contagious. I'm very grateful for our early discussions on interferometry which provided a great start into the project. I was very fortunate to work with Prof. Rodney Clifton and Dr. Tonia Jiao, who hosted me for two weeks at their laboratory at Brown University and taught me how to conduct pressure-shear plate impact experiments. Both Rod and Tonia supported me throughout my experimental campaign with valuable advice and encouragement. I owe a special thank you to Dr. Zev Lovinger, who was fundamental to the success of the experiments and finite element simulations. Zev helped me overcome many challenges with the PSPI setup, was never afraid of getting his hands dirty in the lab and made the overall experience much more enjoyable.

I would also like to thank Petros Arakelian, who was extremely helpful with getting the setup working again after damage to the gun barrel rendered it unusable. I'm also greatly indebted to Ali Kiani and Joe Haggerty at the Galcit machine shop, who helped me when parts broke, got jammed or needed replacing and always manufactured my parts to the highest standards. I greatly appreciate the help I received at the Kavli Nanoscience Institute at Caltech by Matthew Hunt, Alex Wertheim, and Guy DeRose, who accommodated my unconventional requests. I would also like to acknowledge the extremely fruitful discussion with Kent Wallace that lead to the design of the fiber-optics system.

I would like to thank Prof. Ares Rosakis and Prof. Kaushik Bhattacharya for their time and willingness to serve on my committee. I would like to acknowledge all past and present members of the Ravi/Kaushik group who have been wonderful research partners throughout the past years. I thank the staff at Galcit, especially Cheryl Gause, Jamie Meighen-Sei and Donna Mojahedi, who have endured my constant stream of orders for parts and lab supplies. I would like to thank my family and friends from all over the world who have provided the support often required when research becomes tedious.

Finally, my warmest love goes to Eloïse for her understanding, patience, and encouragement and for sharing this journey with me.

ABSTRACT

Understanding the behavior of silica glasses at high pressures and strain rates is of great importance for geological processes and highly relevant to many technological applications including high-powered laser-matter interactions in optical elements and impact/blast damage in defense systems. Materials typically experience large inelastic deformations at high pressures, which are strongly affected by strength-related phenomena such as work hardening, damage and thermal softening. The pressure-shear plate impact experiment (PSPI) provides detailed information on the pressure and strain rate dependent strength properties of materials subjected to uniaxial compression. However, its range of attainable pressures has so far been limited and the assumptions required for its analysis become invalid at pressures beyond the Hugoniot elastic limit of the anvil materials. In this dissertation, a high-pressure PSPI (HP-PSPI) technique is developed that greatly extends the range of attainable experimental conditions by achieving higher terminal projectile velocities in a powder gun setup. A novel fiber-optic heterodyne transverse velocimeter (HTV) is developed to enable the use of robust frequency-based data reduction techniques, which reduce the effect of signal noise and light coupling losses. A forward analysis method, based on finite element simulations, is employed to match the experimentally observed material response during HP-PSPI experiments on soda-lime glass samples while considering the inelastic deformation of the utilized tungsten carbide anvils. Symmetric HP-PSPI experiments on tungsten carbide revealed a loss of strength at normal stresses exceeding 25 GPa, which hint at active damage or softening mechanisms under nominally uniaxial strain compression. A pressure-dependent strain softening model transitions soda-lime glass from an intact strength of 2.8 GPa, below strains of 10-30%, to a failed granular state following extensive inelastic shear deformation, which accurately predicts the measured response over a wide range of stresses (9-21 GPa) and strain rates ($3{\cdot}10^5$-$2{\cdot}10^7$ s^{-1}). Extending the range of previously attainable pressures and strain rates in PSPI experiments, combined with more robust diagnostics and analysis tools, will greatly benefit our understanding of material strength in extreme environments and enables the investigation of material behavior in a currently unexplored range of pressures and strain rates.

PUBLISHED CONTENT AND CONTRIBUTIONS

[1] C. Kettenbeil, M. Mello, T. Jiao, R.J. Clifton, and G. Ravichandran. "Pressure-Shear Plate Impact Experiments on Soda-Lime Glass at Pressures Beyond 20 GPa". In: *Dynamic Behavior of Materials, Volume 1*. Springer International Publishing, 2019, pp. 163–165. DOI: https://doi.org/10.1007/978-3-319-95089-1_30.
C.K. performed the experiments, prepared the experimental data, and wrote the manuscript.

[2] Z. Lovinger, C. Kettenbeil, M. Mello, and G. Ravichandran. "Inelastic Behavior of Tungsten-Carbide in Pressure-Shear Impact Shock Experiments Beyond 20 GPa". In: *Dynamic Behavior of Materials, Volume 1*. Springer International Publishing, 2019, pp. 65–67. DOI: https://doi.org/10.1007/978-3-319-95089-1_8.
C.K. performed the experiments, prepared the experimental data, and participated in writing the manuscript.

[3] M. Mello, C. Kettenbeil, M. Bischann, Z. Lovinger, and G. Ravichandran. "Heterodyne Diffracted Beam Photonic Doppler Velocimeter (DPDV) for Pressure-Shear Shock Experiments". In: *Dynamic Behavior of Materials, Volume 1*. Springer International Publishing, 2019, pp. 73–76. DOI: https://doi.org/10.1007/978-3-319-95089-1_10.
C.K. designed the optical system, developed the velocimetry diagnostics, conducted the validation experiments, prepared the experimental data, and participated in writing the manuscript.

[4] C. Kettenbeil, M. Mello, M. Bischann, and G. Ravichandran. "Heterodyne transverse velocimetry for pressure-shear plate impact experiments". In: *Journal of Applied Physics* 123 (2018), p. 125902. DOI: 10.1063/1.5023007.
C.K. designed the optical system, developed the velocimetry diagnostics, conducted the validation experiments, prepared the experimental data, and wrote the manuscript.

[5] C. Kettenbeil, M. Mello, T. Jiao, R.J. Clifton, and G. Ravichandran. "Pressure-shear plate impact experiment on soda-lime glass at a pressure of 30 GPa and strain rate of $4{\cdot}10^7$ $s^{\check{}1}$". In: *AIP Conference Proceedings* 1979 (2018), p. 070019. DOI: 10.1063/1.5044828.
C.K. developed the experimental setup, performed the experiment, prepared the experimental data, and wrote the manuscript.

[6] M. Mello, C. Kettenbeil, M. Bischann, and G. Ravichandran. "Heterodyne diffracted beam photonic Doppler velocimeter (DPDV) for measurement of transverse and normal particle velocities in pressure-shear plate impact experiments". In: *AIP Conference Proceedings* 1979 (2018), p. 160017. DOI: 10.1063/1.5045016.

C.K. designed the optical system, developed the velocimetry diagnostics, conducted the validation experiments, prepared the experimental data, and participated in writing the manuscript.

TABLE OF CONTENTS

LIST OF ILLUSTRATIONS

LIST OF TABLES

Chapter 1

INTRODUCTION

1.1 Motivation

Silica is the second most abundant material in the earth's crust and hence has a strong influence on many geological processes on the planet. The formation and properties of high-density polymorphs of silica, found in close proximity to large meteoroid impacts on earth, remain relatively unexplored on relevant time scales [1]. Silica glasses are also central to many technological applications such as optical elements (e.g. windows, lenses, optical fibers), as a structural material, transparent armor and microelectronics (MEMS). Within these applications, high-powered laser-matter interactions and impact of silica structural elements create high pressures and strain rates that require the knowledge of the material response under these extreme conditions [2].

Materials at higher pressures will display strength related phenomena such as plasticity, damage, and failure processes, which often dominate the material response and are therefore essential for modeling material behavior. In general, the dynamic strength of materials is a function of a number of parameters such as the thermodynamic state of the studied material (pressure, temperature, density), its loading history and its strain rate. Figure 1.1 (a) and (b) show the dependence of the yield strength of pure aluminum on strain rate and hydrostatic pressure, respectively. Many materials exhibit a strong rate hardening effect as strain rates exceed $10^4 - 10^5$ s^{-1}, which, in metals, is caused by the shift from thermally activated dislocation motion past obstacles [3] to a phonon drag mechanism [4].

Pressure-induced phase transformations add further complexity to characterizing the strength of materials, as structural changes on an atomistic scale may lead to very different material behavior. A phase transformation from on amorphous silica glass to a dense, crystalline phase named stishovite has been observed at stresses above 18.9 [6] and 36 GPa [2].

Due to the complex relationships of material strength on the aforementioned parameters, experiments have to be carried out over a wide range of conditions to develop reliable models for the simulation of various dynamic loading events. The simulations of automobile collisions and bird-strike events on aircraft engines and

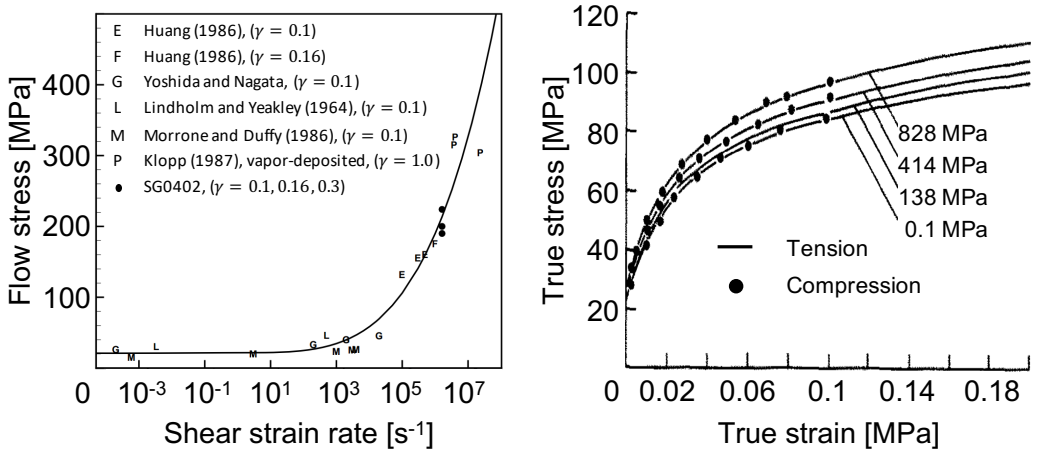

(a) (b)

Figure 1.1: Yield strength of pure aluminum (1100-0) as a function of strain rate [3] and hydrostatic pressure [5].

structures requires the knowledge of the dynamic strength at strain rates of $\sim 10^3$ s^{-1} [7]. The manufacturing time of mechanical engineering components can be drastically reduced by using high-speed machining techniques, which can give rise to strain rates of up to 10^5 s^{-1} [8]. Armor materials subjected to ballistic impact can experience pressures of several GPa with typical strain rates ranging between $10^5 - 10^6$ s^{-1} [9]. Even at pressures above 10 TPa [10], strength is thought to affect the behavior of materials through hydrodynamic instabilities in inertial confinement fusion experiments [11].

1.2 Strength Measurement Techniques at High Pressures and Strain Rates

Experiments at high pressures and strain rates typically generate uniaxial strain conditions through normal [12] and pressure-shear plate impact (PSPI) [13], laser ablation [11], explosive detonations [14] and magnetically applied loading [15]. By assuming a Tresca or von Mises yield criterion, the yield strength Y of materials in uniaxial strain can be obtained by

$$\sigma - \sigma_t = \pm Y, \tag{1.1}$$

where σ and σ_t represent the longitudinal and lateral (transverse) stress, respectively. However, conventional configurations of the aforementioned experiments yield no direct information on the lateral stress component σ_t.

A technique that directly aims to measure the lateral stress component, using in-material piezoresistive gauges, is depicted in Fig. 1.2. A longitudinal and a lateral stress gauge are used simultaneously to determine the current yield strength Y according to Eq. 1.1. This technique's main advantage is the straightforward analysis of material strength. However, there are multiple issues that limit the application of this technique including the calibration and interpretation of the transverse gauge measurements, highlighted by Rosenberg [16], its limited stress range [17], a low temporal resolution due to long signal rise times [18] and the effect of the gauge's presence on the actual strength measurement.

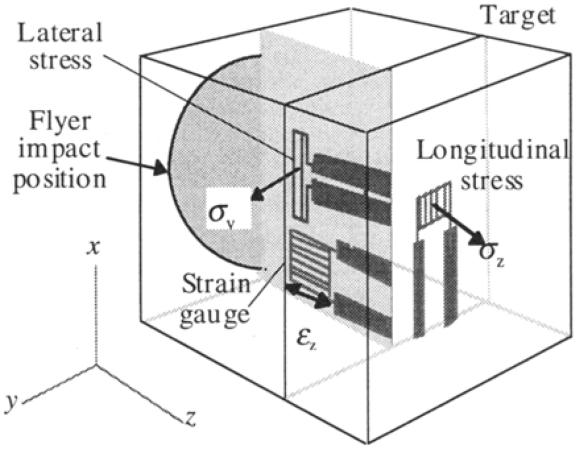

Figure 1.2: Schematic of in-material gauge technique with longitudinal and transverse arrangement of piezoresistive manganin gauges for stress measurements [18].

The self-consistent method, introduced by Lipkin and Asay [12], infers material strength solely from measured free surface normal velocities during reshock and release experiments [12]. Intersecting the extrapolated release and reshock response to the initial shocked state yields a longitudinal stress σ_{max} and σ_{min} as illustrated in Fig. 1.3. The material yield strength at the initial Hugoniot state can, therefore, be estimated by [12]

$$Y = \frac{3}{4}(\sigma_{max} - \sigma_{min}). \tag{1.2}$$

In contrast to the in-material gauge technique, the self-consistent method is not intrusive and is not limited by the admissible stress range of the gauges. It can, therefore, be used for a large range of experimental conditions making it the prevalent method for strength determination in plate impact shock [12, 19–22] and magnetically-driven, isentropic compression experiments [23]. The techniques' relatively low

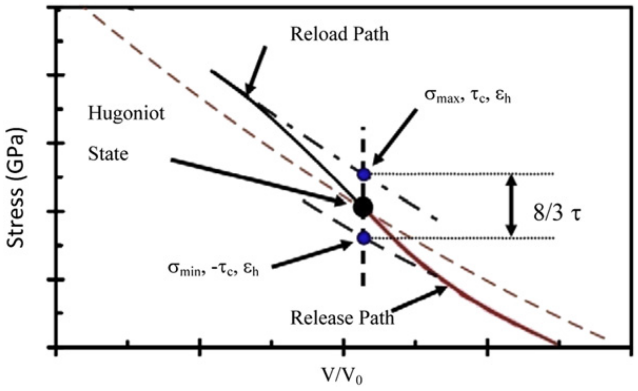

Figure 1.3: Strength determination from reshock and release experiments [19] with the shear strength τ ($Y/2$ in uniaxial strain)

strength sensitivity constitutes its main drawback, which stems from its reliance on two measurements with associated errors that can attain a considerable fraction of the measured material strength.

With the advent of efficient modeling tools and increased processing power, numerical simulations are able to reveal the dynamic strength of materials under more complicated loading conditions. The growth of initial perturbations by Rayleigh-Taylor instabilities, introduced by Barnes [14] using explosive loading techniques, and Richtmyer-Meshkov [11] instabilities, as shown in Fig. 1.4, provides an indirect measure of material strength. Due to their dependence on accurate constitutive relations, hydrodynamic instability experiments are typically employed for strength model calibration and validation rather than the identification of unknown material behavior.

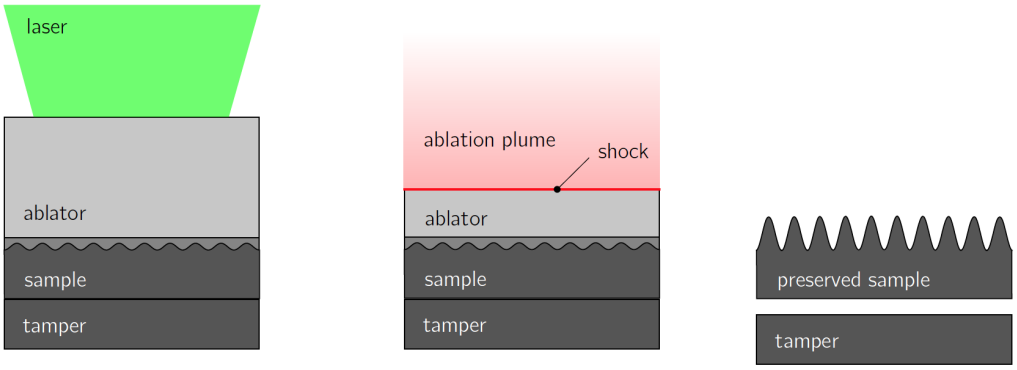

Figure 1.4: Schematic of a laser-driven shock experiment utilizing Richtmyer-Meshkov instability to measure material strength [11].

1.3 Pressure-Shear Plate Impact Experiments

The technique to probe the dynamic strength of materials at high pressures and strain rates employed in this study is the Pressure-Shear Plate Impact (PSPI) Experiment [13]. This technique, as shown in Fig. 1.5, generates both pressure and shear waves by impacting inclined flyer and target plates.

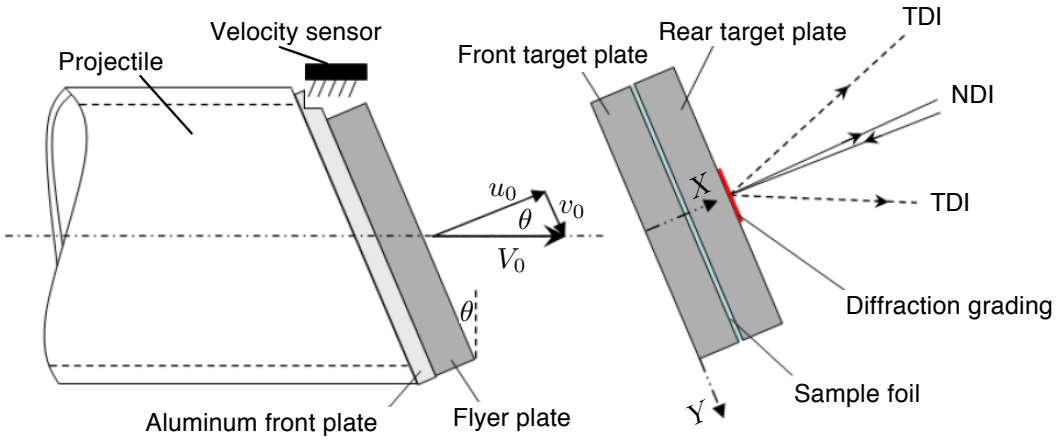

Figure 1.5: Schematic of a Pressure-Shear Plate Impact Experiment in the sandwiched configuration [3].

Normal and transverse velocimetry diagnostics measure the corresponding free surface velocity components to infer the time-resolved sample response. The high strain rate PSPI configuration sandwiches a thin sample foil, typically between 1-300 μm thick, between anvil plates, which remain elastic. The x-t diagram depicted in Fig. 1.6 visualizes the wave propagation of both pressure and shear waves that reverberate inside the sample material until a uniform stress state is achieved.

Assuming linear elastic material behavior for the flyer and target plates, an assumption that will be relaxed in Section 7.1, the normal u_{fs} and transverse v_{fs} velocities at the free surface can be shifted in time to obtain the velocities at the sample interface [3].

After the sample achieves a uniform stress state, its normal σ_s and shear stress τ_s are given by

$$\sigma_s = -\frac{(\rho c_1)_T u_{fs}}{2} \tag{1.3}$$

and

$$\tau_s = -\frac{(\rho c_2)_T v_{fs}}{2}, \tag{1.4}$$

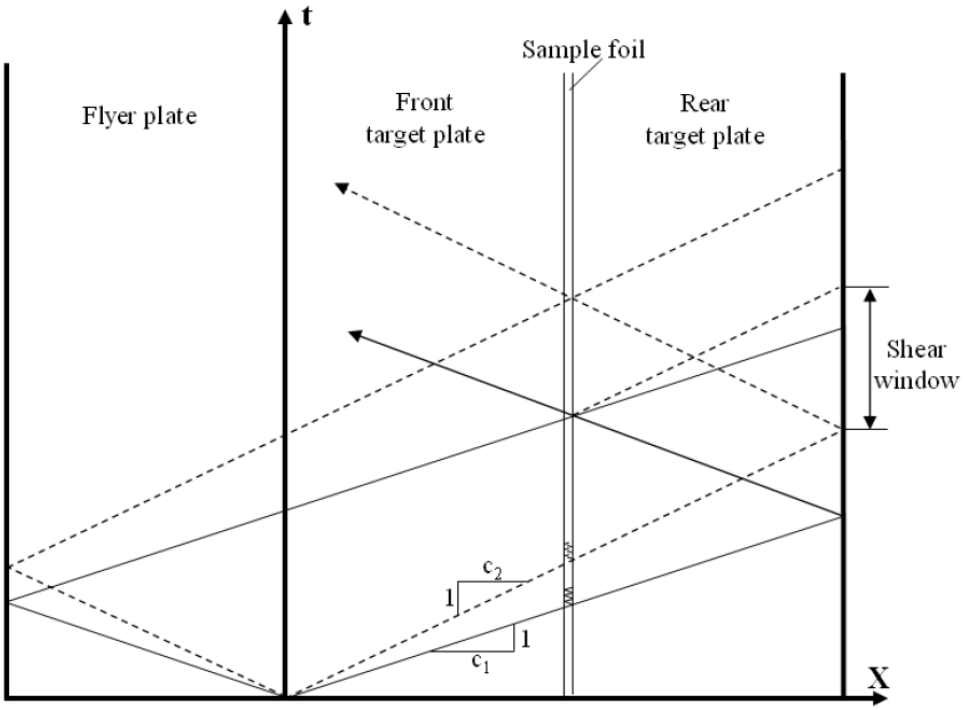

Figure 1.6: Propagation of normal and shear waves during PSPI experiments [3]

where ρ is the density and c_1 and c_2 represent the elastic longitudinal and shear wave speeds of the target anvil material denoted by the index T, respectively. Assuming flyer and target plates with identical impedance, both the shear strain rate $\dot{\gamma}$ and shear strain γ are given by

$$\dot{\gamma} = \frac{v_0 - v_{fs}}{h} \tag{1.5}$$

$$\gamma = \int \dot{\gamma} dt, \tag{1.6}$$

where v_0 represents the transverse component of the impact velocity and h is the sample thickness. The transient reverberations of normal and shear waves inside the sample are illustrated in Fig. 1.7 (a) and (b), respectively. Fig. 1.7 (b) illustrates how the shear strength of the sample material τ is directly related to the measured transverse velocity at the free surface of the rear target plate v_{fs}.

A significant advantage of PSPI experiments over other strength measurement techniques is the high sensitivity of the sample layer's shearing resistance on its strength at high pressures and strain rates. Moreover, the addition of the transverse velocity measurement removes ambiguities in the determination of underlying hardening

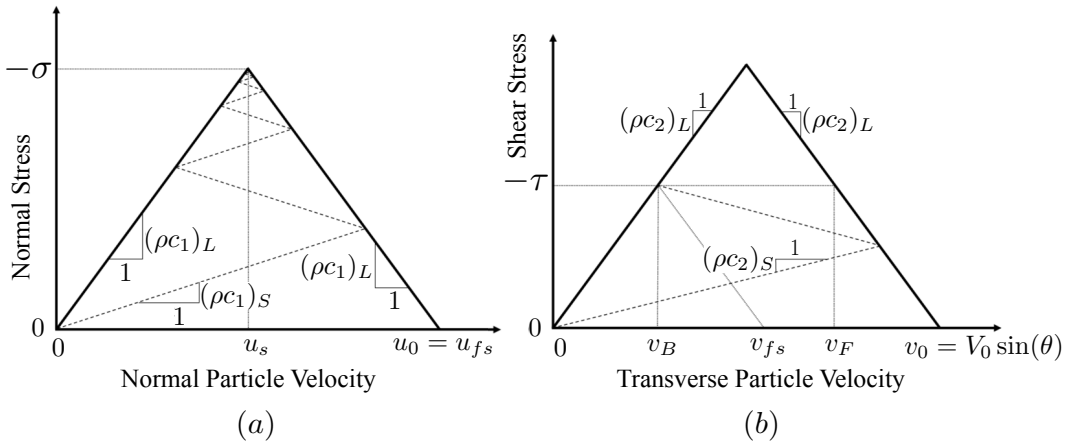

Figure 1.7: (a) Normal and (b) shear wave reverberations inside sandwiched sample material [3].

mechanisms by imposing further restrictions on constitutive models that can explain the measured material behavior.

Abou-Sayed and Clifton pioneered the PSPI technique at Brown University, which has been used to study metals [3], ceramics [24], powders [25], polymers [26], and lubricants [27] at shear strain rates of $10^5 - 10^7$ s^{-1}. Since the classical PSPI analysis technique relies on linear-elastic wave propagation within the anvil materials, most investigations were conducted at pressures below the HEL of Hampden steel plates, 2.8 GPa [24] and tungsten carbide, 6.6±0.5 [28]. The employed single-stage gas guns enable projectile velocities of up to 480 m/s, which results in normal stresses of 21 GPa using high-impedance tungsten carbide anvil plates. In an effort to extend the PSPI technique to strength measurements at higher pressures, the impact velocity has to be increased, which motivates the development of a high-pressure PSPI setup (HP-PSPI) described in Chapter 4.

1.4 Organization of Thesis

The layout of this thesis is as follows. Chapter 2 provides a background on the experimentally observed material behavior of silica glasses at high pressures, including the observed pressure-induced phase transformation, the "failure wave" phenomenon and the dynamic strength of silica glasses.

Chapter 3 presents a molecular dynamics study of the strength of silica glass across the stishovite phase transformation. Silica glass samples, obtained through a quenching process, are subjected to uniaxial shock compression using the multi-scale shock technique. Following the nucleation and coalescence of the crystalline stishovite

phase, a simple shear deformation is applied in order to probe the shearing response of the samples. Strength measurements obtained before the coalescence of grains indicate a partially molten state of the high-density amorphous phase providing a mechanism for the phase transformation on nanosecond timescales.

Chapter 4 describes the development of the high-pressure pressure-shear plate impact (HP-PSPI) experimental setup. A powder gun, which enables the acceleration of projectiles to velocities exceeding 2000 m/s, greatly extends the attainable pressure range of pressure-shear plate impact (PSPI) experiments. The diagnostic system for the simultaneous measurement of normal and transverse velocities, including the novel fiber-optic, heterodyne transverse velocimeter (HTV), and its implementation into the experimental setup are presented. Furthermore, the anvil material selection and considerations for the specimen design are outlined.

Chapter 5, provides a detailed account of the development of the HTV diagnostic. The design of the optical system including the diffraction grating and fiber-optics probes is presented, which reduces light coupling losses due to impact tilt and target normal displacement during PSPI experiments. Normal plate impact experiments on *Y*-cut quartz validate the theoretical interferometer sensitivities and show the efficacy of the novel HTV diagnostic.

Chapter 6 illustrates the results obtained from symmetric HP-PSPI experiments on tungsten carbide and soda-lime glass samples characterized in a sandwiched PSPI configuration. The shearing resistance of tungsten carbide is shown to be significantly reduced at normal stresses above 25 GPa indicating active softening or damage mechanisms under uniaxial strain compression. The pressure-shear response of soda-lime glass is presented for a wide range of normal stresses (9-21 GPa) and strain rates ($3{\cdot}10^5$-$2{\cdot}10^7$ s^{-1}).

Chapter 7 provides a detailed description of the numerical modeling, which enables the inference of strength properties during PSPI experiments at pressures exceeding the Hugoniot elastic limit of the employed anvil plates. A discussion of the spreading and attenuation of shear waves in yielding anvil materials provides a practical guideline for determining the required anvil to sample strength ratio for successful HP-PSPI experiments. Inelastic deformations in tungsten carbide are modeled by a plasticity-based approach, which is in good agreement with experimental results at pressures of 14.1 GPa. A pressure-dependent strain softening model for soda-lime glass is shown to accurately predict the experimental observations.

The implications of the experimental and numerical results are discussed in Chapter 8, while a summary and possible directions for future work are outlined in Chapter 9.

Chapter 2

MATERIAL BEHAVIOR OF SILICA GLASSES AT HIGH PRESSURES

Due to their geological and technological significance, silica glasses have been extensively studied under quasi-static and dynamic loading. The following chapter provides a summary of the material behavior relevant to the study of the inelastic deformation of silica glasses at high pressures and strain rates.

2.1 Uniaxial Compression Behavior

The majority of shock compression experiments in uniaxial strain on silica glasses focus on the determination of their equation of state. Figure 2.1 summarizes the Hugoniot measurements for multiple compositions of silica glass. The results for fused silica, borosilicate, and soda-lime glass all display a negative curvature in stress - volume space termed the "compressibility anomaly" which is responsible for their characteristic nonlinear elastic ramp loading in shock compression experiments [29].

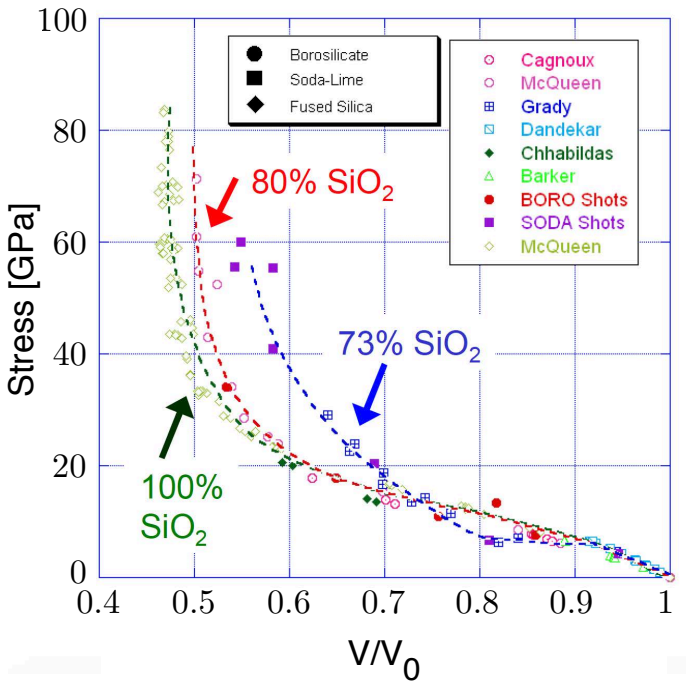

Figure 2.1: Comparison of the stress - volume (Hugoniot) response of fused silica, borosilicate, and soda-lime glass [29].

The mechanisms behind the unique behavior of silica glasses in shock compression experiments are relatively unexplored owing to the difficulty of obtaining accurate atomistic information on nanosecond timescales. Experimental results obtained during quasi-static conditions are discussed to provide insights into the fundamental material behavior that is assumed to persist to some extent during dynamic loading conditions.

In situ Raman scattering during diamond anvil cell tests revealed that the "compressibility anomaly" within the elastic regime of fused silica stems from reversible atomistic rearrangements that resemble the beta to alpha cristobalite transition. This process results in a unique reduction in the elastic moduli from atmospheric conditions to a pressure of 3 GPa [30].

At pressures between 9 - 25 GPa fused silica exhibits large permanent densification ratios in excess of 20%, which is attributed to gradual changes from 4 to 5 coordinated silicon atoms [31]. These irreversible atomic rearrangements coincide with a reduction in average ring size and Si-O-Si bond angles [30]. Beyond pressures of 25 GPa, the permanent densification mechanisms are saturated and additional compression is accommodated by a reversible transition to a 6-fold coordination [30].

2.2 Pressure Induced Phase Transformations

The coinciding pressure-volume response of shock loaded crystalline and fused silica above 30 GPa led researchers to conclude that the same polymorphs, described in Table 2.1, could be present in both materials within this pressure range [1, 32].

	Stishovite	$CaCl_2$-type
	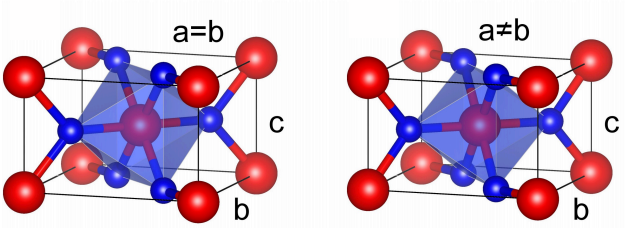	
Stable pressure range (T = 0K)	10 - 50 GPa [33, 34]	50 - 90 GPa [34]

Table 2.1: Unit cells of high-pressure silica polymorphs hypothesized to occur during shock experiments (tetragonal stishovite and orthorhombic $CaCl_2$-type) [35].

Crystalline silica (quartz) was found to transition to a high-density octahedral polymorph named stishovite when subjected to quasi-static compression [36]. However,

only trace amounts of stishovite were found in shock recovered fused silica samples, due to melting upon pressure release during plate impact experiments [6].

Schmitt and Ahrens [1] reported the first experimental observation of the nucleation of stishovite crystals from an amorphous silica glass during shock compression. Temperature measurements depicted in Fig. 2.2 (a) coincide with melting temperatures of stishovite at corresponding pressures (≈3000K). The low emittance in the temperature measurements and visible hotspots in framing camera photographs support a heterogeneous shock deformation mechanism first proposed by Grady [37], which is depicted in Fig. 2.2 (b). Based on the analysis of shock recovered samples, Anan'in [38] suggested that shock compression of silica above its HEL leads to fragmentation into blocks, whose relative motion and corresponding frictional heating result in a network of silica melt surrounding solid material. The higher atomic mobility of the silica melt could then enable the nucleation of the high-pressure stishovite phase on shock compression time scales [1].

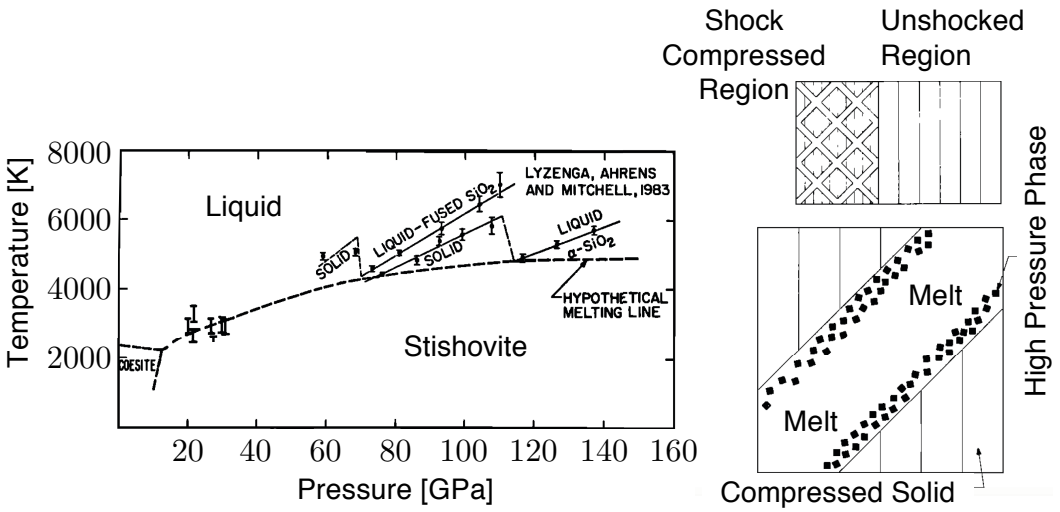

Figure 2.2: (a) Temperature measurements indicating the localized nucleation of crystalline stishovite during shock compression experiments on fused silica at pressures of 20 to 30 GPa [1]. (b) Mechanism of heterogeneous inelastic deformation during shock compression, proposed by Grady [37]. Localized melting enables nucleation of high-pressure silica polymorphs [1].

In-situ x-ray diffraction techniques utilized during laser-driven shock experiments provided the first direct evidence of the phase transformation from a tetrahedrally connected amorphous silica glass to an octahedral network of crystalline

stishovite [6]. Figure 2.3 (a) highlights the formation of diffraction peaks at a transition pressure of 18.9 GPa. However, diffraction signatures obtained during two-stage light gas gun experiments, depicted in Fig. 2.3 (b), observe the amorphous to crystalline phase transformation at normal stresses exceeding 36 GPa [2].

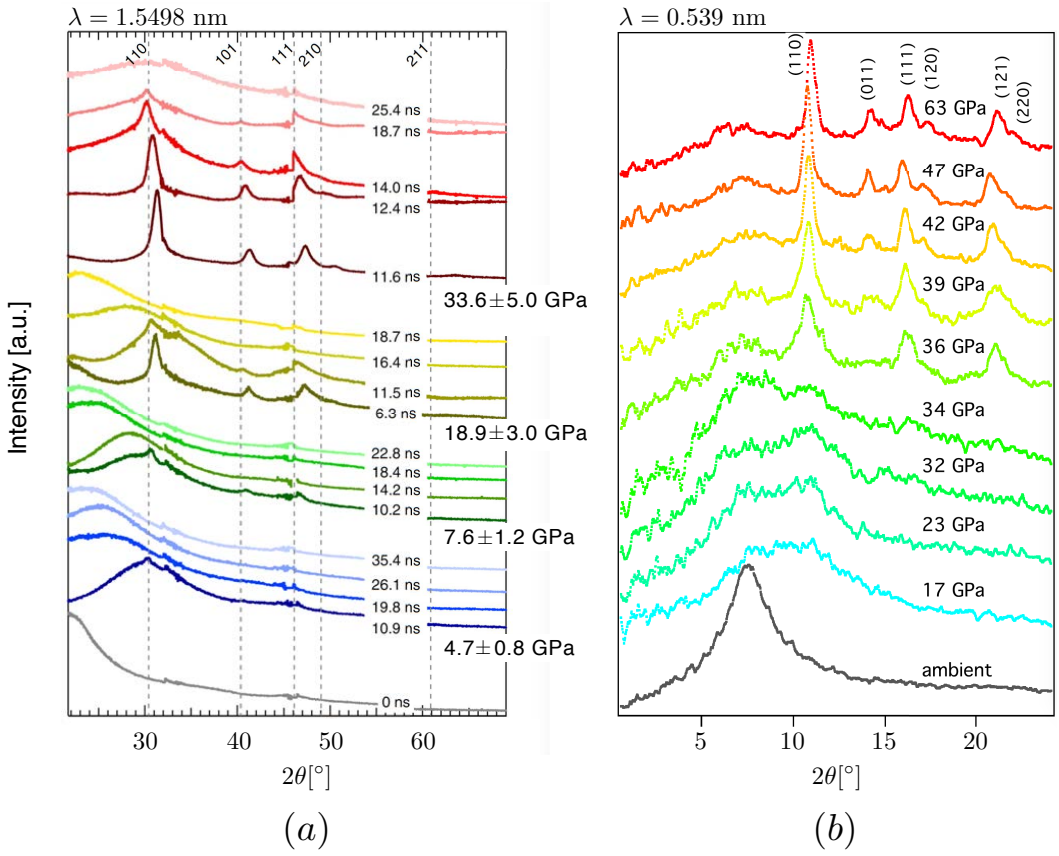

Figure 2.3: In-situ x-ray diffraction measurements on fused silica during (a) laser ablation loading [39] and (b) 2-stage light gas gun experiments [2]. Both experiments observed the formation of distinct stishovite diffraction peaks.

Figure 2.3 (a) additionally shows the azimuthally integrated diffraction pattern for several stages of release. As hypothesized from the analysis of recovered samples, stishovite will transition back to a permanently densified amorphous phase within nanoseconds of shock release [39].

In contrast to the quasi-static behavior of crystalline silica, no additional phase transition from stishovite towards a $CaCl_2$ like structure was observed in measurements at normal stresses between 36 and 63 GPa [2]. This observation is consistent with reported molecular dynamics simulations [40], which found no evidence of a $CaCl_2$ like phase. The timescales (ns$-\mu$s) and temperatures of shock experiments at this

pressure (>3000 K) might not be conducive to the formation of the orthorhombic phase, which is driven by an elastic instability [41] highlighted in Fig. 2.4 (b). It should be noted that the transition manifests itself through broadening of the (120) and (121) diffraction peaks. As the measurements were obtained at pressures only slightly above the 50 GPa transition pressure in crystalline silica, observed in diamond anvil cell experiments, these subtle changes might have not been detectable. Furthermore, the proximity to shock melting, which occurs at pressures of 70 GPa in fused silica [42], could affect atomic rearrangements in comparison to observations made at room temperature.

2.3 Measurements of Material Strength

Quasi-Static Strength of Fused Silica

Non-hydrostatic diamond anvil cell compression experiments can provide a lower bound on the quasi-static yield strength of materials at pressures exceeding 50 GPa [41, 43]. Figure 2.4 (a) displays diamond anvil cell strength measurements collected on fused silica, which illustrate the intimate link between the previously discussed atomic rearrangements and the strength of silica glass [44]. Meade and Jeanloz [43] observed a drastic reduction in strength for pressures of up to 9 GPa followed by a recovery within the range of permanent densification. Subsequent to attaining a peak strength of 4.28 GPa at a pressure of 27 GPa, a linear decrease to a residual strength of 0.32 GPa was measured at a pressure of 65 GPa.

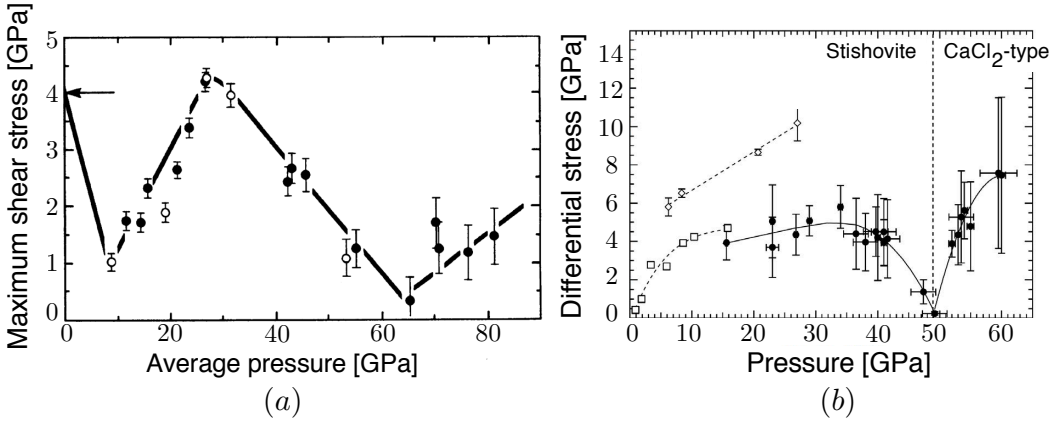

Figure 2.4: Diamond anvil cell strength measurement obtained on (a) fused silica [43] and (b) polycrystalline stishovite [41].

This behavior differs significantly from diamond anvil cell strength measurements carried out on polycrystalline stishovite samples, as depicted in Fig. 2.4 (b). An

elastic instability during the transition from the stishovite crystal to a $CaCl_2$-type structure, manifesting itself through a vanishing shear modulus at the transition pressure [35], leads to a complete loss of strength at a pressure of 50 GPa. Although Meade and Jeanloz [43] do not provide a mechanism for the strength loss at 65 GPa, displayed in Fig. 2.4 (a), an analogous transition to a $CaCl_2$ type phase at slightly higher pressures could account for the observed strength reduction.

Failure Waves

One explanation for the unique material behavior of soda-lime glass at pressures exceeding its HEL was given by Kanel et al. [45], who was the first to observe an anomalous recompression wave during normal plate impact experiments on soda-lime glass. They attributed this feature, as depicted in Fig. 2.5 (a) and (b), to a reflection at a failure front, which coined the term "failure waves" for this phenomenon. Ever since the introduction of the hypothesis, there has been a continued debate about the existence of failure waves and a search for their underlying deformation mechanism [46–49].

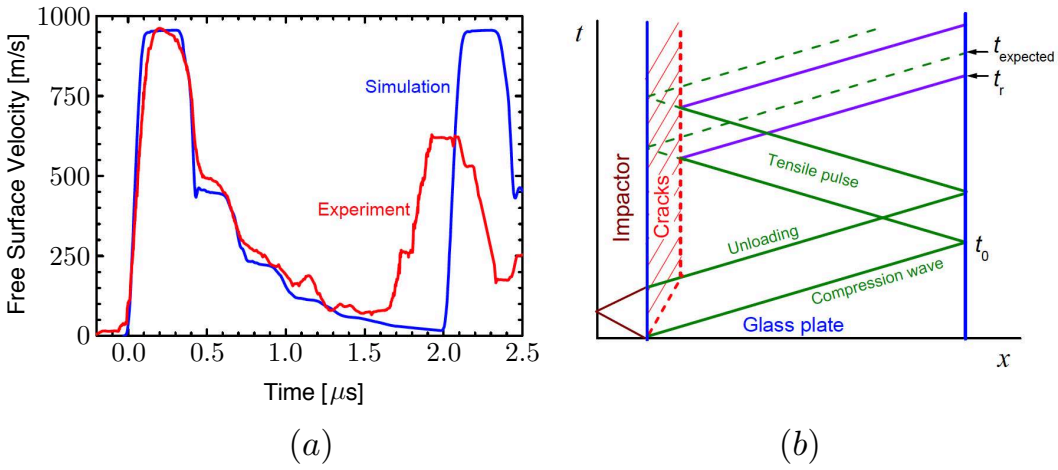

Figure 2.5: (a) Early recompression wave in normal plate impact experiment when compared to simulated response. (b) x-t diagram illustrating the proposed "failure wave" hypothesis [45].

A myriad of investigations followed the discovery of the anomalous inelastic behavior of soda-lime glass during shock compression experiments. Shear [47–49] and spall strength measurements [48] seemed to confirm the interpretation of a propagating failure front, as precipitous strength losses in both loading conditions were observed following shock compression to pressures between 4 and 8 GPa. The occurrence of a propagating failure front for shock pressures in close proximity to

the HEL is in agreement with the heterogeneous deformation mechanism discussed in Section 2.2.

Grady and Chhabildas [50] repeatedly found that shock compression of soda-lime glass to stresses of 4.6-4.7 GPa, depicted in Fig. 2.6 (a), resulted in chaotic rear surface velocity signatures characterized by dips of more than 25 m/s. They hypothesized that stress relaxation associated with permanent densification and inelastic shear deformation could be the cause for this anomalous behavior. Figure 2.6 (a) also depicts early velocity signatures which precede the elastic wave arrival, which were likely shifted in time for the purpose of comparing the different experiments.

Additional support for the failure wave hypothesis came from high-speed images, shown in Fig. 2.5 (b), which depicted the propagation of a dark region illustrating refractive index changes that suggest the nucleation of damaged material under shock compression [18].

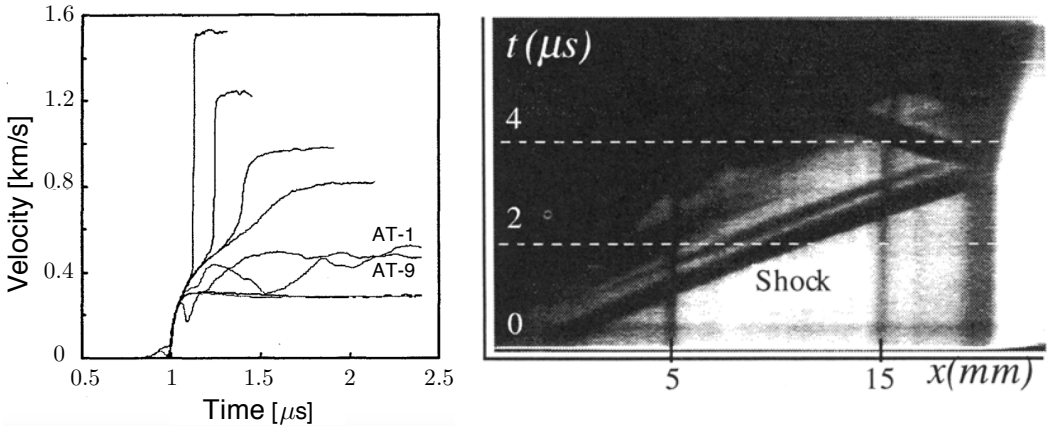

(a) (b)

Figure 2.6: (a) Free surface velocity traces of normal plate impact experiments on soda-lime glass samples under varying impact conditions, showing aberrant behavior observed in experiments AT-1 and AT-9 [50]. (b) Streak camera image of a shock loaded soda-lime glass sample at a pressure of 5 GPa, displaying index of refraction changes indicative of damage nucleation [47].

A phase transformation of soda-lime glass could be considered as an alternative interpretation for the occurrence of "failure waves". A mechanism for this hypothesis is provided by the formation of long-range order observed during diamond anvil cell experiments on soda-lime glass at pressures of 5 GPa, which resulted in similar atomistic rearrangements as in fused silica at pressures above 10 GPa [51]. The horizontal section of the Hugoniot curve of soda-lime glass, depicted in Fig. 2.1,

provides additional support for this hypothesis as a large change in compressibility is a tell-tale sign of phase transformations in materials undergoing shock compression [52]. Simha and Gupta [49] interpret the anomaly as time-dependent inelastic deformation, which is assumed to be affected by a phase transformation, and discount previous interpretations of a propagating failure front.

Dynamic Strength of Soda-Lime Glass

The first investigations on the dynamic strength of silica glasses were conducted on soda-lime glass using the in-material manganin gauge technique [47, 49]. These studies focused on the strength between material yield ($\approx$ 4 GPa) and pressures of 10 GPa to study the "failure wave" phenomenon (see Section 2.3). Figure 2.7 shows the inferred yield strength from two studies that both differentiated between an initial and "failed" or final strength state. Bourne and Rosenberg [47] observe a linear increase of the intact strength up to normal stresses of 6 GPa at which a peak strength of 4 GPa is measured. The experiments conducted by Simha and Gupta [49] suggest a lower, largely pressure-independent, intact strength of 2.8 GPa. This large discrepancy could be caused by the inherent limitations of the in-material manganin gauge technique, discussed in Section 1.2. Both investigations revealed a pressure-dependent failed strength of 1.5 to 2.3 GPa, which coincides with the intact strength in Simha and Gupta's experiments for mean stresses of 8 GPa.

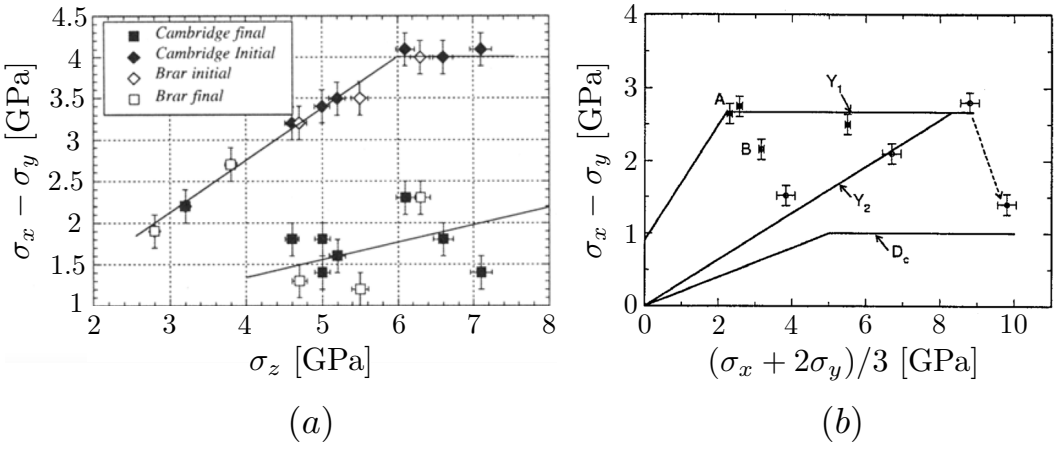

Figure 2.7: The development of intact and failed strength of soda-lime glass as measured by (a) Bourne and Rosenberg as a function of normal stress [47] and (b) its dependence on mean stress as obtained by Simha and Gupta [49].

The strength measurements of the failed state are considerably higher than the flow stress of approximately 250 MPa obtained by Vogler et al. [17] during PSPI

experiments on silica sand, which suggests that a considerable amount of cohesion remains behind the failure front of the aforementioned experiments.

Sundaram [24] conducted pressure-shear plate impact (PSPI) experiments on 5 μm thick vapor deposited soda-lime glass layers sandwiched between steel or tungsten carbide anvil plates at normal stresses of 2.5, 3.5 and 5.7 GPa. He observed that the strength of soda-lime glass, within this pressure range, is constrained by a shear-induced failure at a shear strain of 200%. The calculated shear strain rate and corresponding shear strain are based on Eqs. 1.5 and 1.6, which assume that the sandwiching target plates remain linear elastic. However, significant rounding of the normal velocity traces, depicted in Fig. 2.8 (a), indicate that the steel rear anvil plates might have undergone inelastic deformation. Yielding anvil plates give rise to the spreading of shear waves, as discussed in Section 7.1, which leads to large discrepancies for strain calculations using Eqs. 1.5 and 1.6. Figure 2.8 (b) depicts the measured transverse velocities and corresponding shear stresses, which attain peak values in the range of 460 (SS9702) to 580 MPa (SS9703).

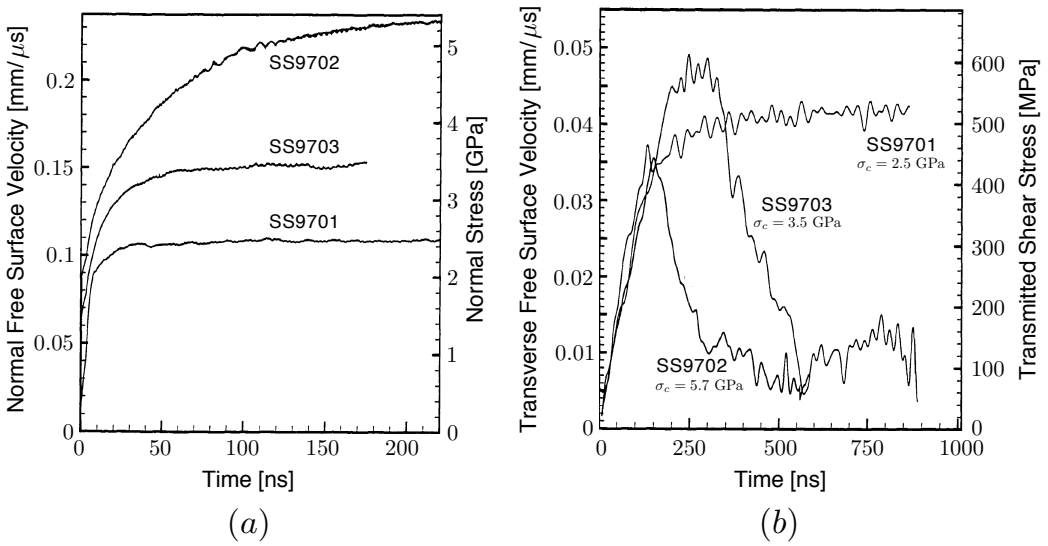

Figure 2.8: (a) Normal and (b) transverse free surface velocities with corresponding stresses, measured during PSPI experiments on a 5 μm thick, vapor deposited, soda-lime glass layer sandwiched between anvil plates [24].

Material strength measurements based on the shock release behavior of soda-lime glass were conducted by Alexander [29] over a wide range of pressures. The evolution of the pressure-dependent strength, shown in Fig. 2.9, qualitatively resembles the quasi-static strength of fused silica measured in diamond anvil cells (see

Fig. 2.4). A complete loss of shear strength in the pressure range of 4 to 6 GPa is reminiscent of previous observations made during investigations of the "failure wave" phenomenon [18, 48, 49]. However, the absence of a finite, failed strength is unaccounted for and could be an artifact of the low strength sensitivity of the employed technique (see Section 1.2). The strength recovers to a peak value of approximately 3.9 GPa at a pressure of 20 GPa and is extrapolated to be lost at a pressure of 55 GPa. Heterogeneous shock deformation, as discussed in Section 2.2, could account for a gradual reduction in strength with increasing shock pressure as the volume fraction of localized melt increases. A three-wave structure in the normal velocity measurements indicating a phase transformation at 60 GPa was interpreted as shock melting indicating that a homogeneously molten state has been attained.

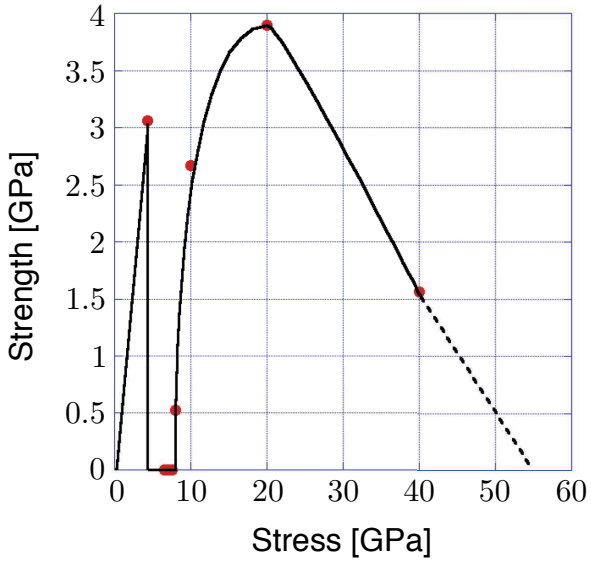

Figure 2.9: Dynamic strength measurements conducted on soda-lime glass using release wave experiments [29].

Chapter 3

MOLECULAR DYNAMICS STUDY OF THE STRENGTH OF SILICA GLASSES

3.1 Motivation

Molecular dynamics simulations are a valuable tool for observing atomistic processes and bridge the gap between quantum mechanical methods such as the density functional theory and continuum simulations based on microstructural models. As described in Section 2.2, fused silica was found to transition from an amorphous tetrahedrally-connected phase to a crystalline octahedral silica network called stishovite during laser-driven [6, 39] and normal plate impact shock experiments [2]. Gleason et al. [6] observed the pressure-induced stishovite phase transformation at pressures of 18.9 and 33.6 GPa, while Tracy et al. [2] reported the formation of diffraction peaks between 36 and 63 GPa. The phase transformation, in both experimental campaigns, occurred on nanosecond timescales, which makes it amenable to study with molecular dynamics simulations. The molecular dynamics calculations described in the following sections are performed using Sandia National Laboratories Large-scale Atomic/Molecular Massively Parallel Simulator (LAMMPS) [53].

3.2 Background

Shen et al. [40] observed the previously described stishovite phase transformation during molecular dynamics simulations by subjecting a fused silica glass sample to uniaxial shock compression. The multi-scale shock technique (MSST)[54], which will be described further in Section 3.3, was utilized to apply appropriate shock jump conditions to the molecular dynamics system. Their results depicted in Fig. 3.1, indicate the homogeneous nucleation of stishovite grains, which experience an initial "explosive growth" phase followed by grain coalescence with maximum grain sizes of approximately 8 nm. Shock pressures between 51 and 62 GPa were reported to be conducive to the nucleation and grain growth within a 1.5 ns simulation window. In accordance with experimental observations [2], x-ray diffraction patterns obtained from the shocked samples show no diffraction peaks associated with the formation of a $CaCl_2$ like structure [40].

Figure 3.2 illustrates the relative potential energy for α-quartz, fused silica, and stishovite [55]. The atomistic arrangement of the high-density silica polymorph

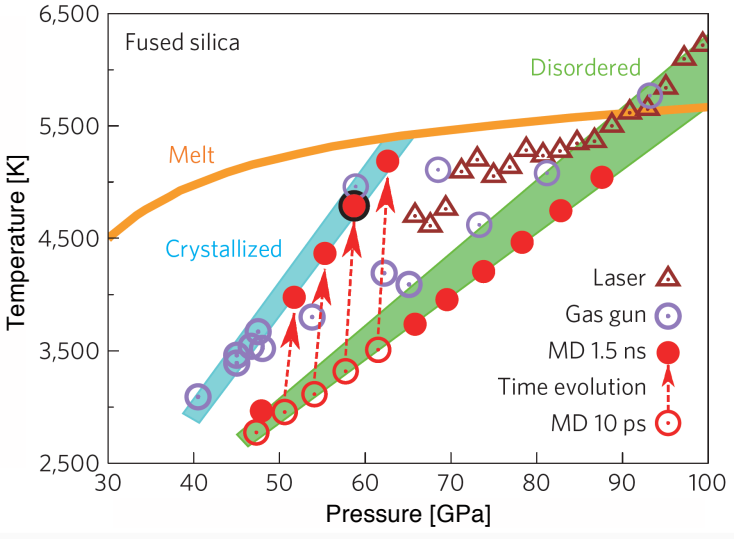

Figure 3.1: Comparison of shock-induced phase transformation in molecular dynamics simulations with experimentally obtained temperature and pressure measurements [40].

becomes energetically favorable above pressures of 50 GPa when compared to amorphous fused silica and α-quartz. However, beyond favorable energetics, transition

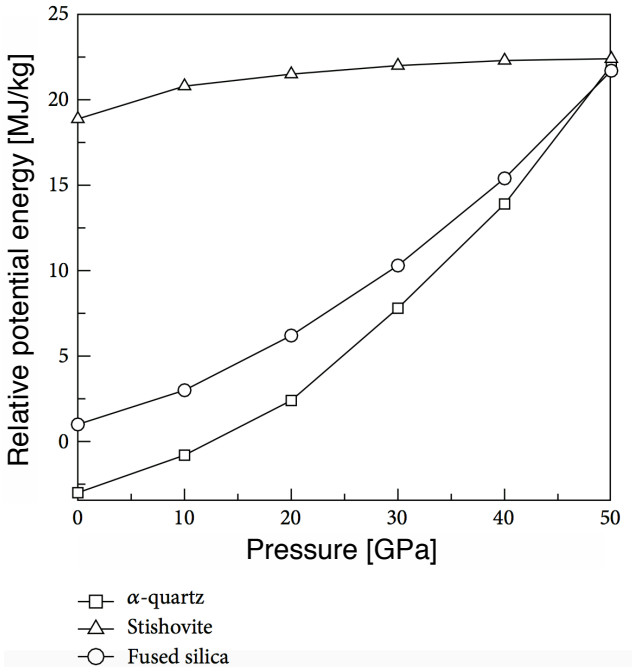

Figure 3.2: Relative potential energies of α-quartz, fused silica, and stishovite as a function of pressure [55].

barriers and transformation kinetics have to accommodate the phase transformation. A longstanding argument against the formation of stishovite grains in silica glasses, within shock experiment timescales ($100 - 10^3$ ns), is that the diffusion of atoms in solid-solid phase transformations occurs on slower timescales [56]. However, shock experiments on iron revealed that solid-solid phase transformations on shock experiment timescales (ns$-\mu$s) can occur for the case of martensitic phase transformations, which involve a collective displacement of atoms below the nearest-neighbor spacing [56].

3.3 Methods

Silica Glass Force Fields

The interaction of atoms in molecular dynamics simulations is based on a potential, which describes the forces atoms exert on each other. The pairwise potential proposed by van Beest, Kramer, and van Santen (BKS) [57], employed here, computes interatomic forces between atoms spaced apart within a cutoff region $r < r_c$. Coulomb interactions beyond cutoff distances are evaluated by a long-range k-space solver utilizing the particle-particle particle-mesh method [58]. The BKS potential is replaced by a repulsive short-distance interaction, for $r < r_m$, to avoid the fusion of particles due to the potential's unphysical divergent behavior at small distances [40]. The full description of the employed force field is as follows:

$$r_{ij} = \begin{cases} \kappa(r_{ij} - r_{ij}^m)^2 + w_{ij} & r_{ij} < r_{ij}^m \\ \frac{q_i q_j}{r_{ij}} e^2 + A_{ij} \exp(-\frac{r_{ij}}{\rho_{ij}}) - \frac{C_{ij}}{r_{ij}^6} - \left(A_{ij} \exp(-\frac{r_c}{\rho_{ij}}) - \frac{C_{ij}}{r_c^6}\right) & r_{ij}^m \leq r_{ij} \leq r_c \\ \frac{q_i q_j}{r_{ij}} e^2 & r_c < r_{ij} \end{cases}$$

where the indices i, j are associated with properties of either silicon or oxygen atoms, q_i represents the partial charges ($q_O = -1.2, q_{Si} = 2.4$), and e is the electric charge of one electron whereas A_{ij}, C_{ij}, $\kappa = 100$ eV·Å^2, and ρ_{ij} are interaction parameters. Continuity across interatomic distances is enforced through the additive constant w_{ij} at $r_{ij} = r_{ij}^m$ and by subtracting the Buckingham term from the BKS potential at $r_{ij} = r_c$. This modification has been shown to not affect the elastic or shock behavior of silica [40] in the conditions studied here. Isolated instances of particle fusion do occur without the short-range potential during the preparation of the glass sample at 6000 K, which is detailed in Section 3.3. Table 3.1 shows the employed BKS potential parameters.

i-j	A_{ij} [eV]	ρ_{ij} [Å]	C_{ij} [eV·Å^6]	r_{ij}^m [Å]	w_{ij} [eV]
O-O	1388.773	0.36232	175	1.439	20.782
Si-Si	-	-	-	-	-
Si-O	18003.7572	0.20521	133.5381	1.1936	-27.305

Table 3.1: Parameters of modified BKS force field [40].

Multi-Scale Shock Technique

The classical approach to creating a shock wave within a molecular dynamics simulation is to subject the model to a sudden velocity boundary condition, which is representative of the desired particle velocity. Modeling the material response to the passage of a single shock wave requires that no reflections originating from free surfaces interact with the initial shock wave. Longer simulation times t_{sim}, which are required to observe time-dependent phenomena such as phase transformations, require an increasingly long domain size in the shock direction. The associated computational cost scales with t_{sim}^2, which quickly becomes intractable considering the necessary lateral domain size to remove finite size effects.

The multi-scale shock technique [59] is a method with a moving reference frame that couples the volume and temperature of the molecular dynamics sample to the Hugoniot jump conditions, which describe the conservation of mass, linear momentum, and energy across a steady shock wave. By not modeling the actual wave phenomena, surface reflections and interactions are nonexistent, which removes the requirement for a larger domain in the shock direction and leads to a linear scaling of the computational cost with the simulation time.

Reed et al. [59] developed a non-unique Lagrangian that automatically enforces the conservation of momentum and energy

$$L = T(\dot{\vec{r}}) - V(\vec{r}) + \frac{1}{2}Q\dot{v}^2 + -\frac{\mathrm{v_s}^2}{v_0^2}(v_0 - v)^2 + p_0(v_0 - v), \tag{3.1}$$

where T and V are the kinetic energies per unit mass, Q is a mass-like parameter, p_0 is the initial pressure, $\mathrm{v_s}$ is the prescribed shock velocity, and v and v_0 are the current and initial specific volume, respectively. The resulting equation of motion for the system volume is given by

$$Q\ddot{v} = \frac{\partial T}{\partial v} - \frac{\partial V}{\partial v} - p_0 - \frac{{\mathrm{v_s}}^2}{v_0^2}(v_0 - v)^2. \tag{3.2}$$

The mass-like parameter Q, which is set to $Q = 40.0$ amu^2·Å^6 for the simulations conducted here, adds an effective viscosity, which is required to dampen initial unphysical oscillations during the shock ramp up [59]. As both volume expansion and compression constitute viable solutions to Eq. 3.2, the volume has to be slightly biased to favor the compressive solution [59]. This is achieved by applying an initial temperature reduction $t_{scale} = 0.01$ [40]. The shock severity is chosen by selecting different shock velocities v_s, which will result in different shock pressures and associated, consistent thermodynamic states.

Although an iterative process that accounts for shock wave instabilities, such as the elastic-plastic transition is possible, the work reported here limits itself to stable, overdriven shock waves which occur at pressures above approximately 40 GPa [2]. A more detailed description of the multi-scale shock technique can be found in Reed [59].

Sample Preparation

A representative atomic arrangement of amorphous silica was obtained by melting an α-quartz domain of 18,018 atoms (67x62x62 Å) with periodic boundary conditions at 6000 K followed by a quenching process to 300 K within 9 ns ($6{\cdot}10^{11}$ K/s) using an NPT ensemble. This domain size and cooling rate were shown to provide converged material properties, such as the radial distribution function and density of the glass sample [40, 60]. Figure 3.3 depicts the transition from the initial α-quartz atomic structure to the amorphous silica glass after the described quenching process.

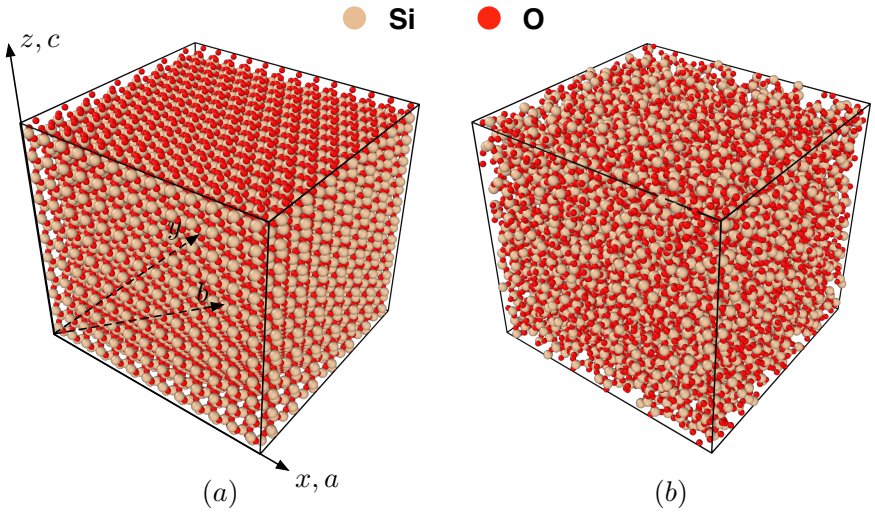

Figure 3.3: (a) Initial α-quartz atomic arrangement. (b) Silica glass obtained from quenching process.

The nucleation of a crystalline phase introduces a new length scale into the previously amorphous material. The kinetics of the phase transition were shown to be free of finite size effects for a simulation domain of 144,144 atoms (134x125x124 Å) [40], which was obtained by replicating the previously described silica glass sample in all three dimensions and equilibrating the result for 100 ps.

The quenched silica glass samples are then subjected to shock compression using the previously described multi-scale shock technique at different pressures. Figure 3.4 depicts the stishovite transformation observed during molecular dynamics simulations with pressures between 49.9-63.5 GPa (v_s = 6700 – 7500 m/s) within the 2 ns simulation time.

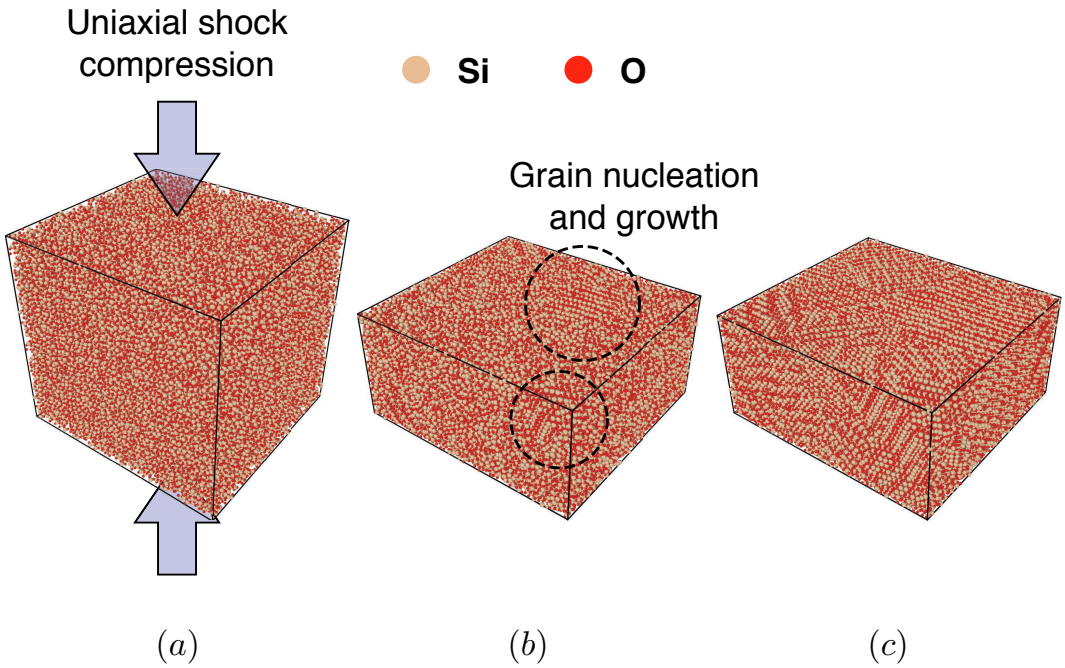

Figure 3.4: (a) Uniaxial shock compression of quenched silica glass sample. (b) (b) Nucleation of crystalline stishovite phase. (c) Crystalline stishovite sample.

The sample temperatures increase drastically during the transformation due to the lower energy state of stishovite at pressures above 50 GPa. Table 3.2 summarizes the thermodynamic state of the shocked samples. Considering the large uncertainties associated with experimental shock temperature measurements, the simulated shock temperatures compare favorably with reported experimentally measured temperatures of 5800 K during the stishovite phase transformation at a pressure of 63 GPa [2].

v_s [m/s]	p [GPa]	T [K]	ρ [kg/m^3]
6600	47.5	2990	4380
6700	49.9	3700	4460
6800	51.2	3930	4480
7000	55.0	4240	4500
7500	60.6	5260	4530
7600	65.3	3780	4530

Table 3.2: Thermodynamic state of silica glass samples after a simulation time of 2 ns.

3.4 Results and Discussion

The strength measurement under simple shear deformation is obtained by applying a displacement in the x-direction (see Fig. 3.3) to the upper x-y surface of the domain. The shocked samples were subjected to an engineering shear strain rate of $5{\cdot}10^8 s^{-1}$ until a shear strain of 20% was achieved, while a constant volume and energy were enforced by an NVE ensemble.

Figure 3.5 depicts the computed shear stress-shear strain relationship for the samples shocked to various pressures. The behavior is compared to the shearing response of a quenched silica glass sample at ambient conditions.

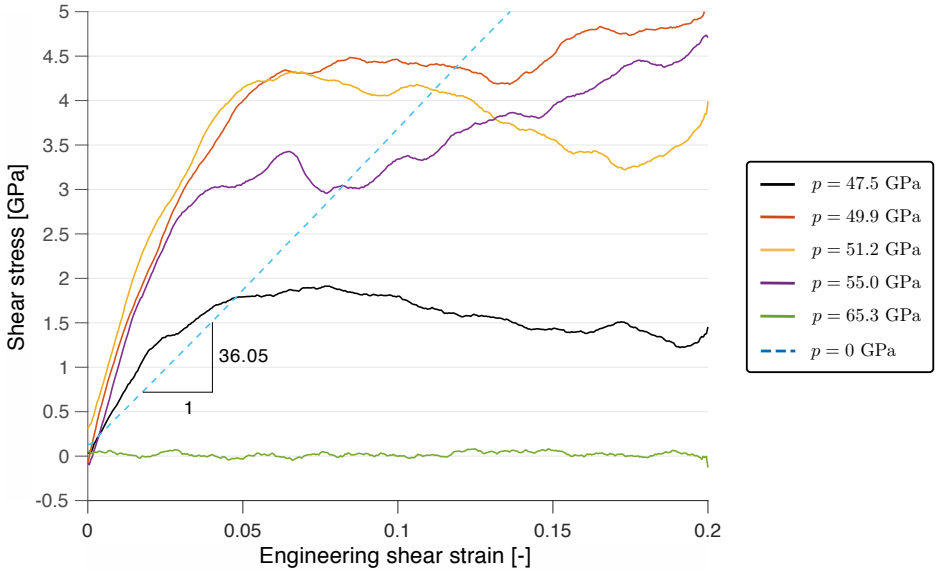

Figure 3.5: Shear stress-shear strain measurements obtained from quenched ($p = 0$ GPa, $T = 300$ K) and shocked samples. Shear stresses were smoothed with a moving average of 20 samples.

The quenched silica glass sample shows a prolonged elastic region with a shear

modulus of 36.05 GPa, which is higher than the experimentally reported value of 30.4 GPa under quasi-static conditions [30]. The non-transformed, high-density amorphous silica exhibits an increased shear modulus of approximately 62 GPa. The observed strong increase in the shear modulus of silica glass is consistent with results from diamond anvil cell experiments at pressures of up to 26 GPa [30]. The transitioned stishovite samples are significantly stiffer with shear moduli of approximately 76 GPa. Comparison with quasi-static measurements, obtained during room temperature diamond anvil cell experiments, is hindered by the previously described elastic instability of stishovite and transformation to a $CaCl_2$ like structure at pressures of 50 GPa. The samples shocked to 49.9 and 51.2 GPa exhibit the highest shear strength of 4.2 GPa at shear strains of 5.5%. Due to the lack of imperfections, pores, and defects within the sample domain, the computed strength will typically be higher than measured in experiments. The 55 GPa sample exhibits a lower shear strength of 3 GPa and 4% shear strain. Considering the strength loss at 65.4 GPa, the reduced strength might be explained with the onset of thermal softening. As no stishovite was formed in the 65.3 GPa sample at temperatures of 3780 K, its high temperature will result in (partial) melt, which was experimentally observed to occur at shock pressures of approximately 70 GPa [42]. Despite its lower temperature, the "low"-pressure amorphous sample starts to deform inelastically at shear stresses of 1.2 GPa and approximately 2% strain, which could be attributed to its lower melting temperature [1].

The normal stresses within the samples prior to transformation have been observed to converge to a common value, which is typically associated with a loss of strength. Figure 3.6 shows the shearing resistance of the 51.2 GPa sample before the nucleation and coalescence of stishovite grains at a simulation time of 0.2 and 0.6 ns in contrast to the crystalline sample obtained after 2 ns. Before the nucleation of stishovite grains at approximately 0.85 ns and the following coalescence phase at 1.6 ns, a much lower shear strength of approximately 0.5 GPa is observed, which could hint at a partially molten state. Figure 3.7 shows the trajectories of three particles during the 55 GPa multi-scale shock technique simulation. All three particles have a large range of motion, perpendicular to the shock direction, indicating high mobility before the coalescence of stishovite grains.

These observations support the hypothesis that higher atomic mobility in partially molten silica enables the stishovite transformation and provides a mechanism for the required atomistic rearrangements on nanosecond timescales. As described in Sec-

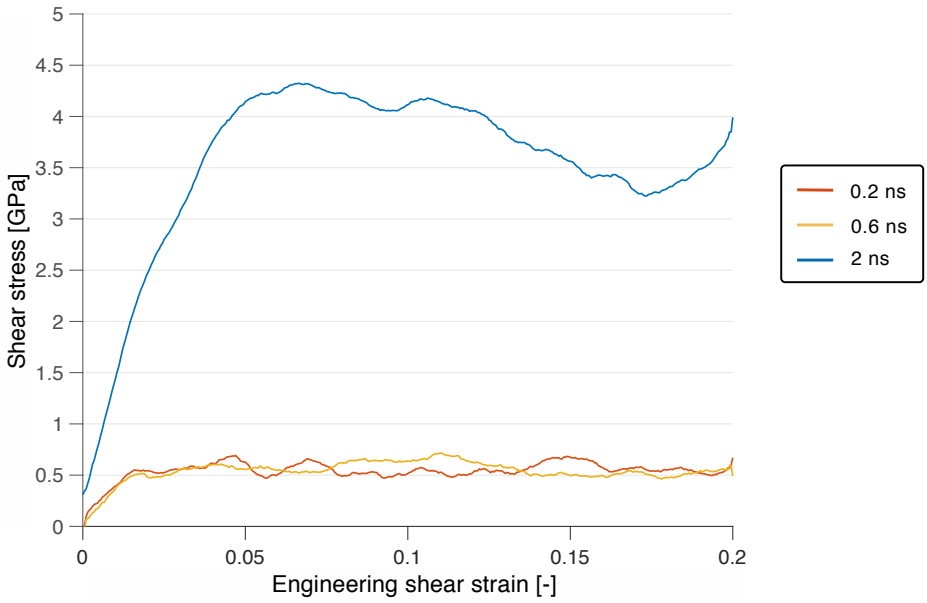

Figure 3.6: Comparison of the shear stress-shear strain obtained from the shocked 51.2 GPa sample in its non-crystalline state after 0.2 and 0.6 ns with the stishovite sample (2 ns). Shear stresses were smoothed with a moving average of 20 samples.

tion 2.2, this constitutes the same mechanism postulated by Schmitt and Ahrens [1], which explains their localized, high-temperature measurements at pressures between 20 and 30 GPa.

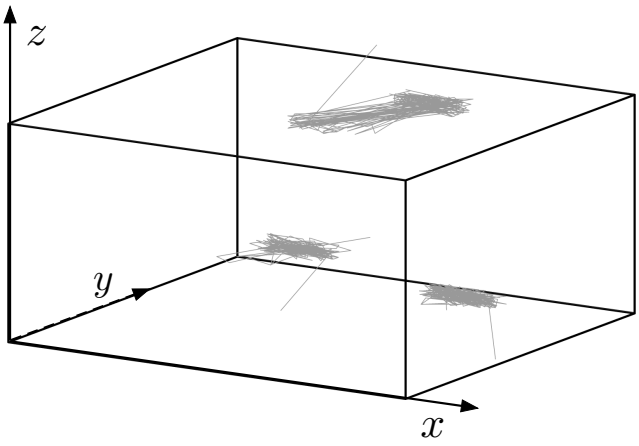

Figure 3.7: Trajectories of three particles during p = 55 GPa shock simulation illustrating high particle mobility perpendicular to the shock direction.

3.5 Conclusion

The molecular dynamics investigation into the shear strength of silica glass across the stishovite phase transformation yielded valuable insights into the mechanism of stishovite nucleation and melt in silica glass. Analysis of particle trajectories and shear strength before the nucleation of the crystalline phase indicates that the required atomistic rearrangements on nanosecond timescales are enabled by a partially molten sample and the associated higher diffusivity of silicon and oxygen atoms. Furthermore, the formation of stishovite, with its increased melting temperature, furnishes silica's strength at high pressures ($p \sim 50 - 60$ GPa) and temperatures ($T \sim 3700 - 5260K$) with shock melting observed at pressures above 65 GPa.

The reasonable agreement between shock temperature predictions provided by the multi-scale shock technique and experimental results, suggests that representative thermodynamic states are attained during the simulations and that the BKS interatomic potential [57] provides a valid description of the material behavior of silica and its high-density polymorphs. This technique could result in more accurate shock temperature estimates compared to analytical methods, which typically neglect pressure-dependent material parameters such as the specific heat capacity. An extension of PSPI experiments to pressures of 50-60 GPa would enable a detailed study of how these observations compare to realistic samples with inherent microstructural defects or how different compositions, e.g. borosilicate or soda-lime glass, affect the phase transformations.

Chapter 4

EXPERIMENTAL METHODS

The pressure-shear plate impact experiment (PSPI), introduced in Section 1.3, probes the strength of materials at high pressures and strain rates by subjecting the sample material to combined pressure-shear loading. The following chapter describes the apparatus, diagnostics and specimen design for the high-pressure PSPI setup (HP-PSPI), which greatly extends the range of attainable pressures in pressure-shear plate impact experiments.

4.1 High-Pressure, Pressure-Shear Plate Impact Experimental Setup

Given identical anvil materials, higher pressures and strain rates in pressure-shear plate impact experiments, are achieved by increasing the impact velocity of the flyer plate. Past PSPI experiments were solely conducted on single stage gas guns, which restricted the terminal projectile velocity to approximately 500 m/s [26]. For the research described in this dissertation, a 38 mm diameter powder gun, as depicted in Fig. 4.1 (a), creates a hot, high pressure driving gas ($p_{max} \approx 200$ MPa) which enables the acceleration of projectiles to impact velocities in excess of 2000 m/s.

There are numerous challenges associated with this approach. The oblique impact of the PSPI technique requires the control of the projectile's roll degree of freedom after the alignment of the impacting plates has occurred [3]. The axisymmetric geometry of the barrel is broken by the introduction of an axial keyway as illustrated in Fig. 4.1 (b), which guides a keyed sabot over the entire length of the gun barrel. Due to the high pressures routinely experienced by powder guns, their steel barrels are generally designed with a smaller inside diameter than single-stage gas guns and need to be heat treated to achieve the required hardness and strength. This greatly complicates the manufacturing process of the barrel keyway as it leads to much higher stresses in the utilized cutting tools. The keyway design was predominantly driven by the minimization of stress concentrations during the repeated pressure loading in an effort to alleviate the formation of cracks. This resulted in a 1.6 mm deep and 3.2 mm wide keyway with corner radii of 1.5 mm.

The higher pressures experienced during projectile acceleration in powder guns affects the sabot design in multiple ways. Most notably, thorough failure analysis is

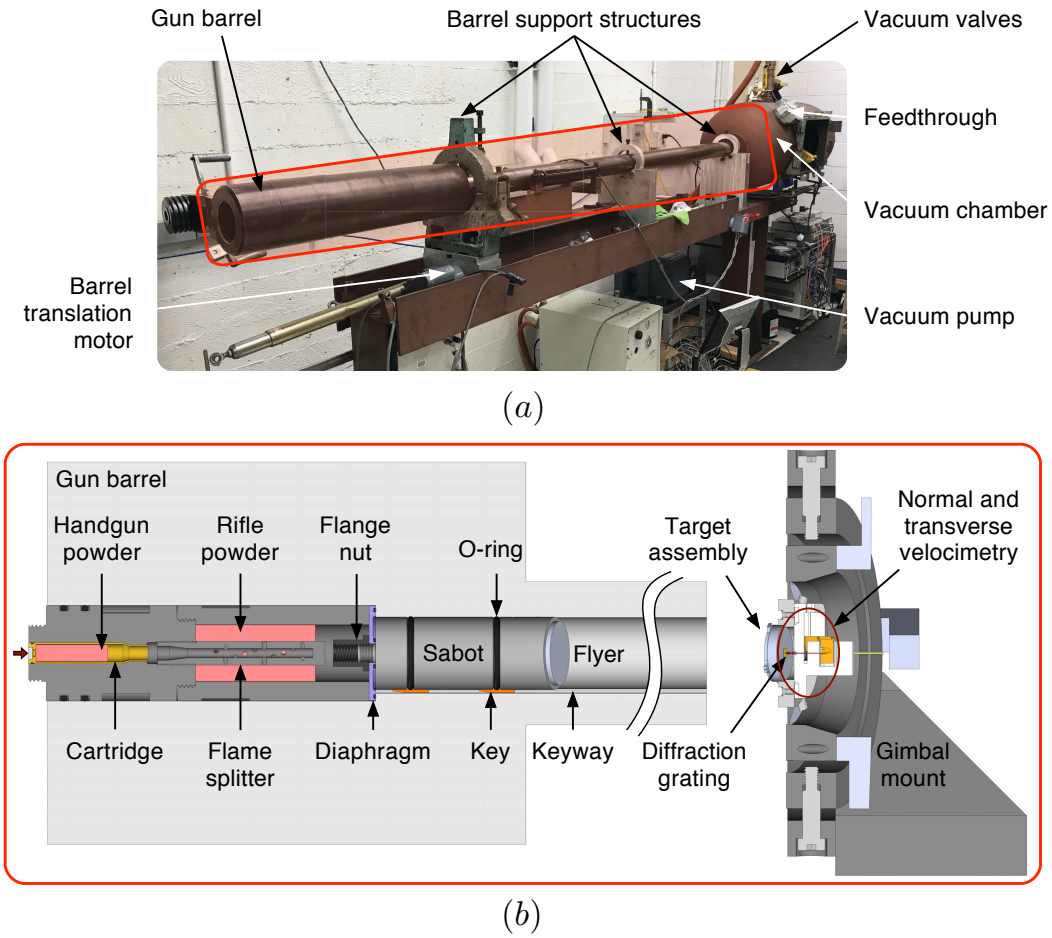

Figure 4.1: (a) High-pressure pressure-shear plate impact (HP-PSPI) setup utilizing a 38 mm powder gun at Caltech. (b) Section view of the powder gun, gimbal mount, and target holder components.

required as pressures can exceed the elastic limit of most polymers and some metals. Beyond a potentially catastrophic sabot collapse, even small plastic deformations on the order of tens of μm can lead to sufficiently large impact tilt angles that cause issues with light coupling for interferometric measurements (see Section 5) and complicate the stress analysis [3]. Thus, a sabot composed of high-strength aluminum (Al-7075) was employed for the experiments reported here. The driving pressure is sealed, unconventionally for powder guns, by two standard O-rings which enable the retraction of the sabot after the final alignment of the flyer and target plates.

The parallelism of the flyer and target plate is kept to within 25 μrad using an autocollimator that measures the reflection of first-surface mirrors attached to the

impact surfaces of both plates [61]. Figure 4.2 (a) depicts the gimbal target mount which was designed with six degrees of freedom that can be precisely adjusted during the alignment stage and locked to reduce movement prior to impact. The

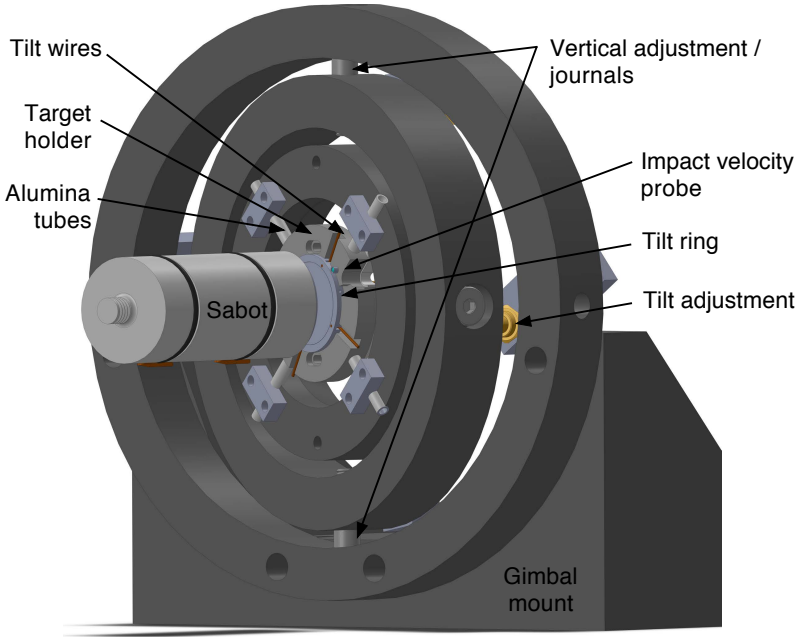

(a)

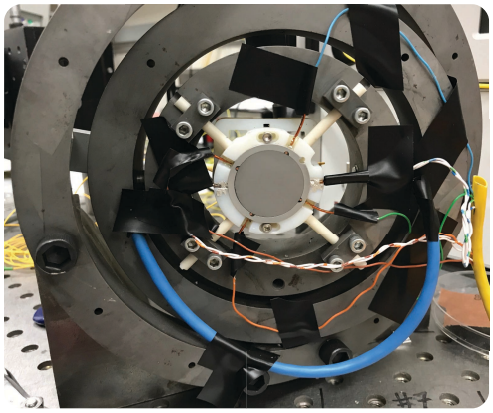

(b)

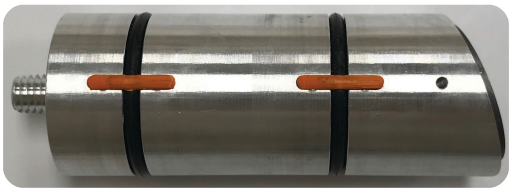

(c)

Figure 4.2: (a) CAD model of the actual gimbal mount with target assembly (b) and sabot with O-rings and keys attached (c).

gimbal rings are made from tool steel and hardened to 45 HRC to reduce wear from impacts with ejecta formed during the experiment. Figure 4.2 (b) shows the actual target holder assembly with the employed aluminum sabot for pressure-shear plate impact experiments shown in Figure 4.2 (c). The projectile and target assembly

are decelerated by impacts with successively thicker aluminum sheets (3.175 - 12.7 mm) that are arranged in a catch tank behind the gimbal mount.

Fig. 4.3 displays the fiber optic probes for the normal and transverse velocimetry

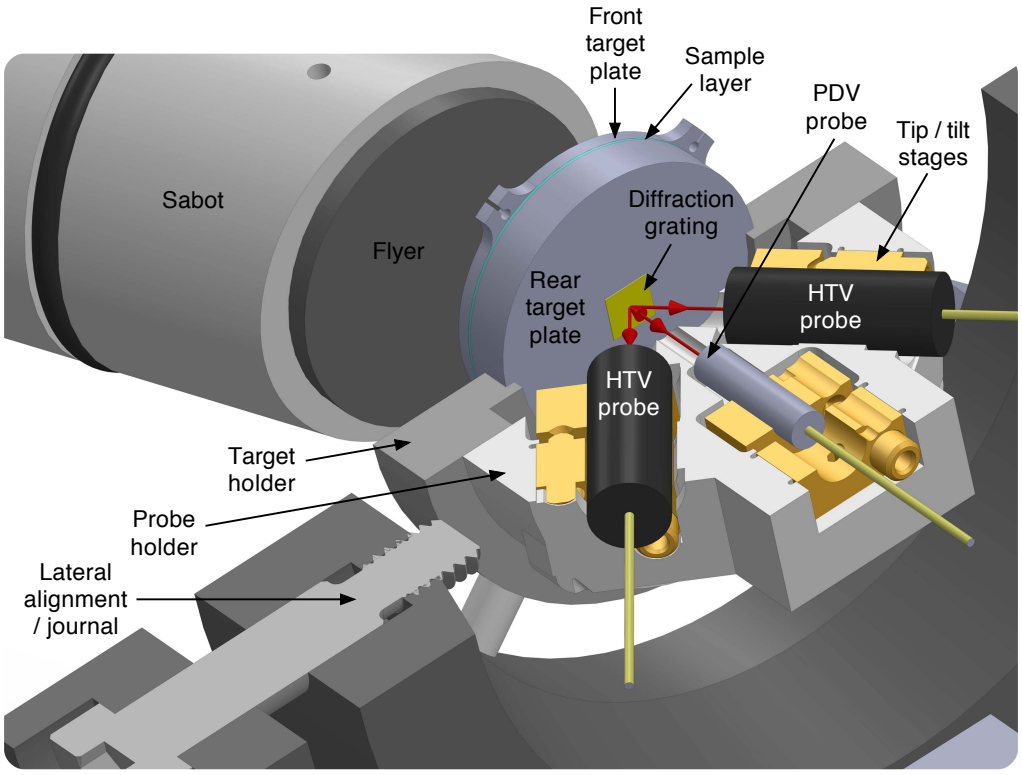

(a)

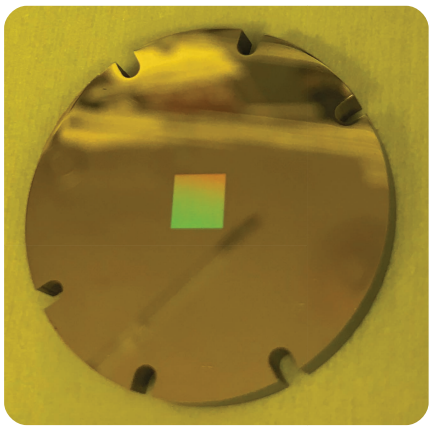

(b)

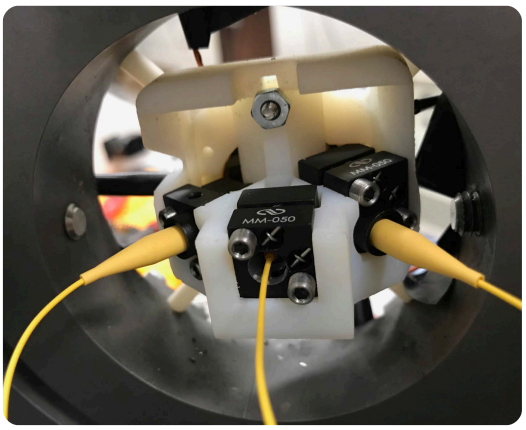

(c)

Figure 4.3: (a) Section view highlighting the fiber-optic heterodyne transverse velocimeter (HTV) and photonic Doppler velocimetry (PDV) diagnostics. (b) Rear target plate with gold diffraction grating. (c) Assembled probe holder with tip/tilt stages and fiber-optics aligned to their respective diffraction orders.

diagnostics. They are bonded to modified tip/tilt stages, which are placed in a high precision, additively manufactured polymeric probe holder that guarantees optimal alignment to the $\pm 1^{st}$ diffraction orders for the heterodyne transverse velocimeter (HTV) probes [62]. Precise alignment is obtained by maximizing the collected light intensity of the normal and transverse probes using fiber optic return loss and power meters.

4.2 Diagnostics

Figure 4.4 highlights the components of the photonic Doppler and heterodyne transverse velocimetry (PDV, HTV) diagnostics utilized for the simultaneous measurement of normal and transverse particle velocities at the rear surface of the target in PSPI experiments. The seed and booster laser provide the single wavelength light (λ = 1550 nm) required by the velocimetry diagnostics for the measurement of the impact (PDV), normal (PDV) and transverse (HTV) velocities [62]. The light returned by the fiber-optic probes, depicted in Fig. 4.3 (a), is interfered with a reference laser and light that propagated through an acousto-optical (AO) frequency shifter for the PDV and HTV diagnostics, respectively. The resulting interference fringes are then converted to analog electrical signals by high-bandwidth (12 GHz) photodetectors. A more elaborate description of the challenges, design, and validation of the velocimetry system is given in Chapter 5. A previous setup, as described in Section 5.3, used a 4 km fiber-optic delay to combine the measurement of the

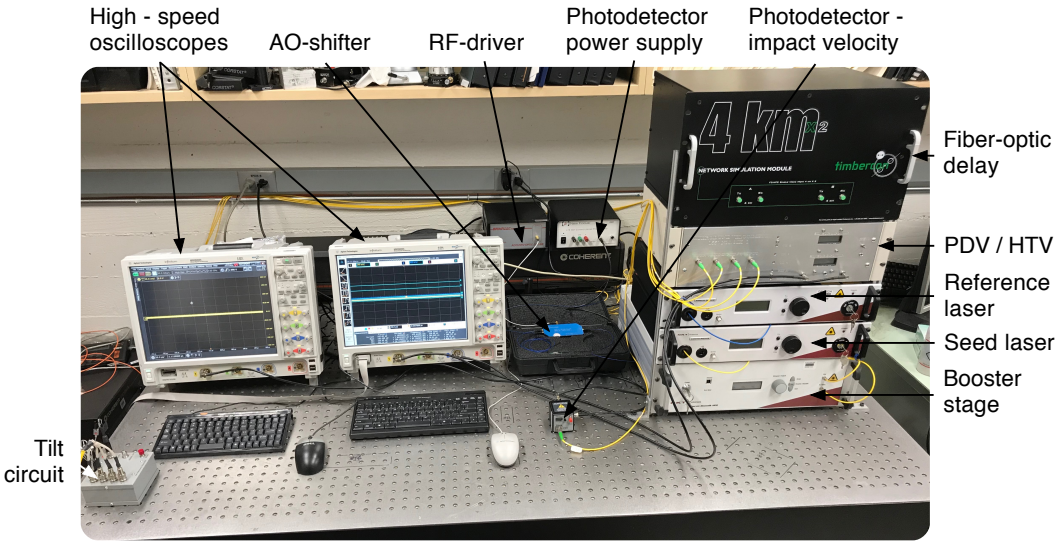

Figure 4.4: Diagnostics components for the measurement of tilt, impact velocity (PDV), normal (PDV), and transverse (HTV) velocities.

impact and target normal velocity on a single channel on one high-speed oscilloscope (20 GSa/s). The configuration depicted in Fig. 4.4 improved the signal fidelity of both measurements by utilizing designated oscilloscopes and photodetectors for each measurement.

The tilt diagnostic relies on time of impact measurements at four points using magnet wires that are lapped flush with the impact surface to within 1 μm. When impact with the flyer plate closes the open circuit between the electrically biased magnet wire and the grounded target plate, flip-flop logic gates (TI SN74S74SN) will switch from an ON to an OFF state which is recorded by four distinct digital channels on a high-speed oscilloscope (2 GSa/s). A 9 ns switching time of the utilized logic gates will give rise to a measurement uncertainty of ±0.15 mrad for experiments with a normal impact velocity of 500 m/s. A NAND gate combines the output of all four circuits and triggers the oscilloscopes when the first flip-flop has switched off. For non-conductive target materials, a circumferentially bonded tilt ring that is lapped flush with the impact surface, as highlighted in Fig. 4.2 (a), holds the biased magnet wire and provides a ground for the electrical circuit.

4.3 Anvil and Specimen Design

Accurate knowledge of the dynamic, inelastic behavior of anvil materials utilized for high pressure, PSPI experiments is essential for the correct inference of sample material properties, which is discussed in more detail in Section 7.1. Ideal anvil materials have a high Hugoniot elastic limit (HEL) and retain most of their strength during inelastic deformation and at high temperatures. Furthermore, a high mechanical impedance (ρc_1) (density, ρ, longitudinal wave speed, c_1) is the driving factor for extending the range of accessible pressures for a given impact velocity V_0. Table 4.1 compares candidate anvil materials based on relevant properties for PSPI experiments.

Material	ρ [kg/m^3]	ρc_1 [GPa/km/s]	HEL [GPa]	T_{melt} [K]
Diamond	3500	64.3	60-80	3820
Sapphire	4000	44.4	17-22	2330
Tantalum	16700	55.8	2	3270
Tool Steel	7900	47.0	1-2	1700
Tungsten Carbide	15600	106.5	5	3140
Zirconia	6000	43.2	14-17	2990

Table 4.1: Material properties of candidate anvil materials.

Its high longitudinal impedance (ρc_1), HEL, and melting temperature make tungsten

carbide an ideal anvil material for high-pressure plate impact experiments. Furthermore, recent PSPI experiments [26] have shown that tungsten carbide retained most of its strength at normal stresses of up to 21 GPa. For these reasons, tungsten carbide was selected as the anvil material for this study.

The geometry of the anvil plates is predominantly defined by the barrel diameter and the dimensions of the magnet wires for the measurement of impact tilt. Given a maximum outside diameter and the longitudinal wave speed c_1, an estimate for the arrival of lateral release waves can be obtained. The maximum shear strain in bulk material PSPI experiments is obtained by defining the flyer and target plate thicknesses such that wave reflections from the rear surface of the flyer plate do not arrive at the measured location prior to the lateral release waves. Release waves from the sample interface have to be taken into account when designing experiments involving a thin sample layer.

Materials are typically tested in either a symmetric configuration, where a thin sample layer is located between the flyer and target plate [26], or a configuration where the sample is sandwiched between a front and rear target plate [3]. A fully symmetric configuration with a sample on both the flyer and target impact surface imposes a symmetric velocity boundary condition which can simplify the interpretation and modeling of experiments. Nevertheless, a configuration with a front and rear target anvil sandwiching the specimen layer, as depicted in Fig. 4.3, is employed here. The faster longitudinal wave ramps up the normal stress through reverberations inside the sample prior to the shear wave arrival, thereby reducing the probability of slip at the sample interfaces in the sandwiched configuration.

Based on these considerations, a 34 mm diameter flyer plate impacting target anvils and specimen layers with a diameter of 30 mm were chosen. The nominal flyer, front and rear target anvil plates have thicknesses of 5, 2 and 4 mm, respectively. A Lagrange x-t diagram depicting the normal and shear wave propagation during experiment CK-1808, as described in Section 6.1, is shown in Fig. 4.5.

The soda-lime glass samples prepared for the PSPI experiments were produced with two different manufacturing techniques as no production method was suited to produce the full range of sample thicknesses. The 5 μm thick samples were vapor deposited directly onto the tungsten carbide front target plates, whereas the 100 and 300 μm thick glass samples, depicted in Fig. 4.6, were lapped down from a bulk material.

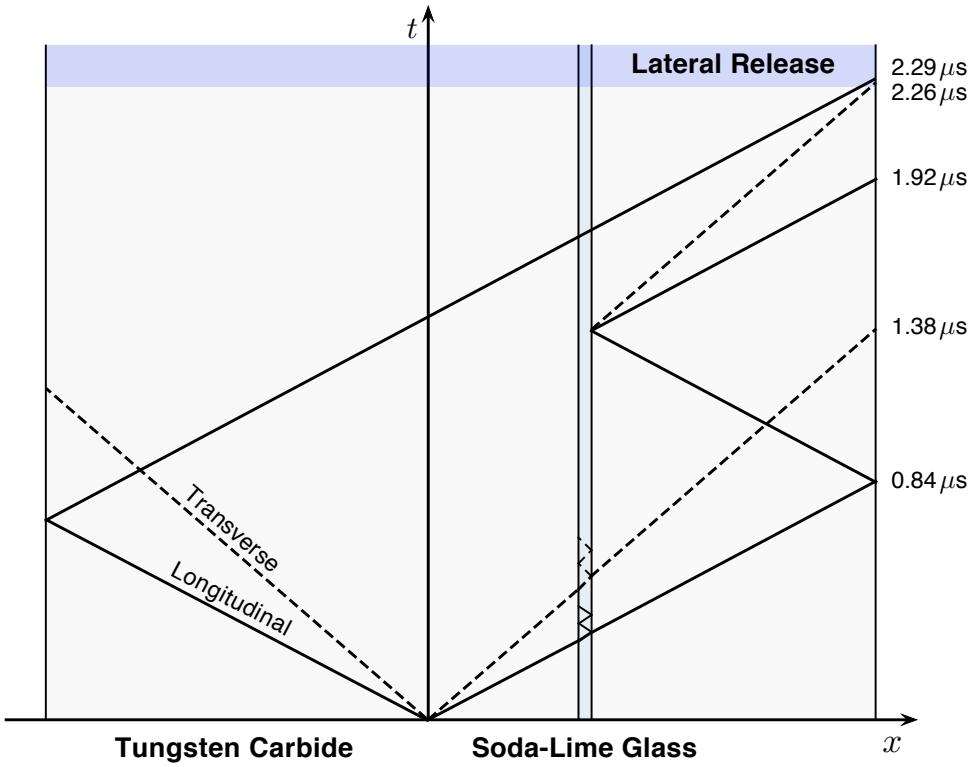

Figure 4.5: Lagrange x-t diagram illustrating the propagation of longitudinal compression and transverse shear waves during experiment CK-1808 (see Section 6.1).

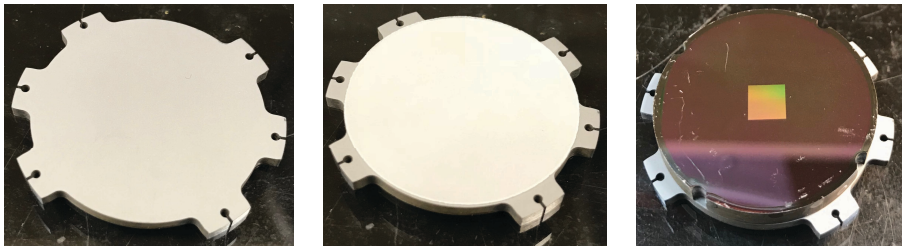

(a) (b) (c)

Figure 4.6: (a) Tungsten carbide front target plate. (b) 300 μm thick soda-lime glass sample on the front tungsten carbide target plate. (c) Target assembly with front and rear target plate sandwiching the soda-lime glass layer with the diffraction grating at the rear surface.

Chapter 5

NORMAL AND TRANSVERSE VELOCIMETRY FOR PRESSURE-SHEAR PLATE IMPACT EXPERIMENTS

5.1 Introduction

The measurement of plane waves involving both longitudinal and transverse velocity components is of particular importance for the study of material strength at high strain rates ($>10^4$ s^{-1}) and pressures ranging from hundreds of MPa to several TPa. These conditions arise in, amongst others: PSPI experiments [63], dynamically loaded anisotropic crystals [64, 65], laser-generated shear waves [66] and magnetically-applied pressure-shear experiments (MAPS) [67]. Traditional PSPI experiments rely on the transverse displacement interferometer (TDI) [64] for the measurement of in-plane displacement histories. Recently, this technique has been extended to an all fiber-optic configuration [68]. Alternative schemes have leveraged dual VISAR (Velocity Interferometer System for Any Reflector) arrangements [65] that utilize normal and angled probes to measure transverse velocity components. The main disadvantage of this technique is that the fringe constant, as determined by the etalon delay leg, is set to measure a superposition of both normal and transverse particle velocities which generally differ by an order of magnitude. Hence, the dual VISAR approach can not realize the full potential of the VISAR interferometry technique for PSPI experiments.

In recent years, there has been a paradigm shift towards the application of PDV (photonic Doppler velocimetry) for normal velocity measurements [69]. Along with the change in instrumentation came the utilization of robust short-time Fourier transform analysis techniques that are inherently more immune to signal noise than previously used phase-based methods and can, therefore, tolerate more light loss during an experiment. The frequency-based approach is also largely immune to amplitude modulation of the interferometer signals and does not depend on normalized (amplitude corrected) fringe records to extract frequency information, as required when processing a single (unheterodyned) interferometer signal.

A limitation of "standard" (unheterodyned) PDV is the inability of the technique to derive temporally-resolved measurements of low particle velocities from fringe records or even partial fringes with correspondingly low signal frequencies. This

limitation in temporal resolution leads to inaccuracies and signal processing artifacts as demonstrated by the discrepancy between a synthetic ramp velocity input pulse and its measured result depicted in Fig. 5.1(a). A heterodyned interferometer signal

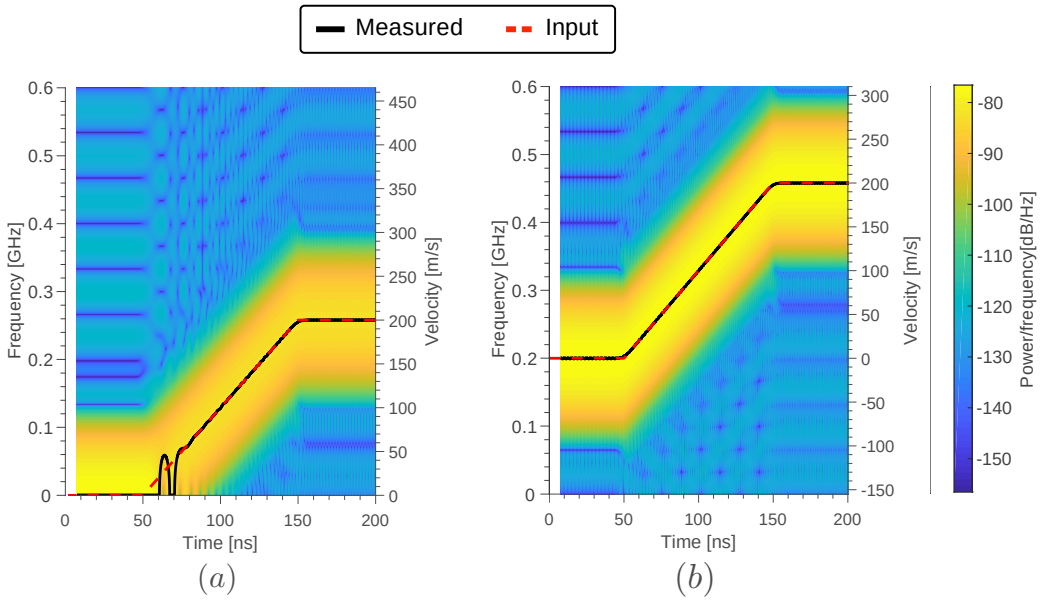

Figure 5.1: Frequency spectrum over time for a ramp velocity input pulse (dashed line) with inferred velocity for (a) "standard" and (b) heterodyne PDV. A Hamming window with a duration τ =15 ns was employed for the frequency analysis.

exhibits a carrier frequency f_c at zero target velocity as depicted by the ramp wave frequency spectrum in Fig. 1(b). The increased frequency enables the use of shorter time windows for the Fourier analysis and thus provides a high temporal resolution even at low velocities. While information at low velocities is not always required for traditional normal plate impact experiments, it is absolutely crucial for measuring transverse velocities in PSPI experiments, which are typically below 50 m/s.

The main goal of this work is to extend heterodyne PDV techniques, with their robust frequency-based analysis methods, to transverse interferometers utilized in PSPI [63] and magnetically-applied pressure-shear experiments [67]. Two different approaches were pursued to introduce a carrier frequency in transverse velocimetry signals. Both techniques rely on diffracted 1^{st} order beams generated by a specular, metallic grating deposited on the rear surface of the target plate. The diffracted beam photonic Doppler velocimetry (DPDV) technique interferes each 1^{st} order beam with a reference laser adjusted to a slightly higher wavelength. An additional benefit of this transverse velocimeter lies in the independent measure of the normal velocity record that can be obtained by decoupling the normal motion from the diffracted

order signals. The second technique, called the heterodyne transverse velocimeter (HTV), sends the $+1^{st}$ diffracted order through an acousto-optic frequency shifter to create a carrier frequency upon interference with the -1^{st} order beam. In a similar fashion to the transverse displacement interferometer [64], this approach provides a pure measurement of transverse motion. A measurement of the normal particle velocity is obtained from a heterodyne PDV arrangement employing the reflected 0^{th} order diffracted beam. The strengths and limitations of each interferometer design are addressed and the techniques are compared by examining fringe records obtained from normal impact validation experiments conducted on Y-cut quartz.

5.2 Optical Design

Collecting diffracted or scattered light at an angle from the surface normal, to measure in-plane transverse displacements or velocities, poses a set of unique challenges in PSPI experiments that are not encountered in normal plate impact experiments. Normal displacement accumulated over the course of the experiment causes decentering of the diffracted beams at the receiving fiber-optic probes resulting in a rapid loss of light intensity. Light loss is further exacerbated by small tilt angles between the impacted surfaces of the flyer and target plates. Analyzing the geometrical effects of target tilt and normal displacement of the target surface can provide valuable insights into a suitable optical design. The optical design software Zemax was applied to investigate and quantify light loss due to both of these effects during PSPI experiments. The normal displacement during a PSPI experiment will depend on the impact velocity, experiment duration, and material response, resulting in varying optimal designs for different experiments. However, impact tilts of up to 2 mrad (0.11°) are considered typical in PSPI experiments and should lie within the light loss tolerance exhibited by the optical system.

Probe Design

Figure 5.2 shows two optical systems that were investigated for their tolerance to normal displacement and tilt of the target plate's rear surface. The calculation of the coupling efficiency requires the computation of an overlap integral between the electric field that impinges on the fiber-optic core and the mode that can propagate in the utilized single mode fiber. However, many qualitative trends can be explained by appealing to geometrical optics.

Geometrical Analysis of Optical System

Figure 5.2(a) shows a fiber-optic configuration using focusing probes, which are commonly utilized in normal plate impact experiments [70]. The advantage of a focused optical system is its insensitivity to small rotations of the target rear surface, as highlighted in Fig. 5.2(b). The limitations of using this approach for transverse measurements become immediately apparent in Fig. 5.2(a), which highlights how quickly a diffracted or scattered beam is decentered with respect to the optical axis of the receiving probe upon normal motion of the target. Figure 5.2(a) also indicates that a larger spot size on the target rear surface, corresponding to a longer working distance W, increases the tolerance to normal displacement. The natural extension of this principle is to introduce a collimated light system, which is shown in Fig. 5.2(c). By reducing the beam diameter of the source probe, the diffracted beam will decenter, with respect to the optical axis of the receiving probe, without a reduction in light intensity at the fiber core until the decentered beam is vignetted by the edge of the receiving lens. The disadvantage of a collimated optical system is emphasized in Fig. 5.2(d). Any tilt angle α of the target rear surface will introduce a lateral translation of the focused spot αf from the fiber-optic core, which has a diameter of 8.2 μm for standard $\lambda = 1550$ nm wavelength single-mode fiber. One way to alleviate this concern is to utilize a source probe lens with a short focal length f resulting in a small source beam diameter. This leads to an enlarged focused spot size at the focal point of the receiving probe, which is larger than the fiber-optic core resulting in light coupling even when the center of the light distribution is displaced laterally by αf. This approach of increasing the system's tolerance to tilt comes at the expense of lower overall coupling efficiency. However, this does not pose a limitation for the systems presented here, as light collected by the angled probes is close to the damage threshold of the photodetectors, which limits the usable light intensity in the employed interferometer systems. Another factor that has to be taken into account with collimated optical systems, is that a light beam can only stay collimated over a finite distance. Assuming Gaussian beam propagation the collimation distance corresponds to the confocal parameter b, given by [71]

$$b = 2z_R = \frac{2\pi\omega_0^2}{\lambda}, \tag{5.1}$$

where z_R is the Rayleigh range parameter and ω_0 represents the beam waist radius. Equation (5.1) highlights the increasing importance of the Rayleigh range with smaller beam sizes. The collimated source beam used in the final experimental configuration has a beam diameter of 280 μm, which yields a Rayleigh range

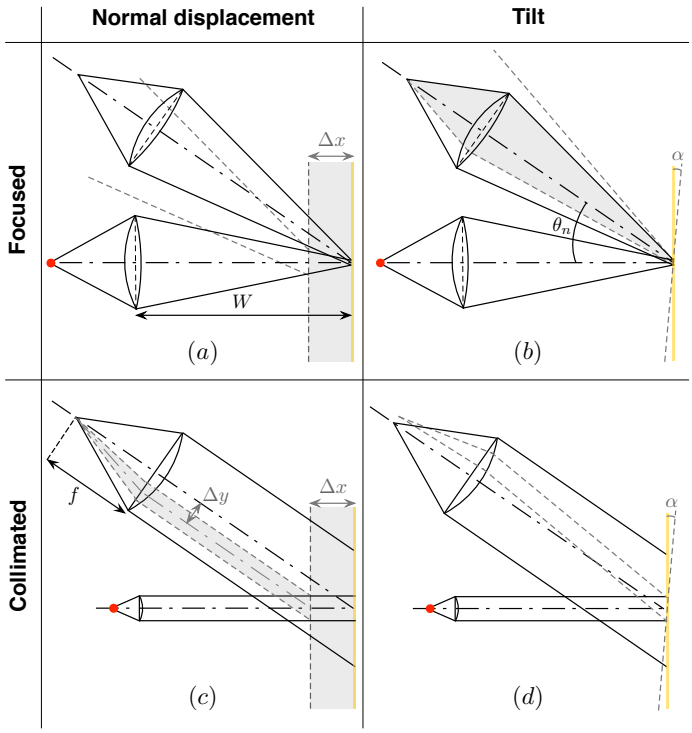

Figure 5.2: Geometrical analysis of light coupling in fiber-optic transverse interferometers for focused (a)-(b) and collimated (c)-(d) optical designs subject to normal displacements Δx and tilt α.

$z_R \approx 40$ mm, corresponding to an 80 mm collimation distance. In order to avoid reductions in coupling efficiency, the distance between the source and receiving lens should be kept below this value. In contrast to focusing systems, collimated designs experience no light loss due to the depth of field of the employed probe lenses for $W < z_R$.

Now that the geometrical effects have been established, the conflicting nature of the requirements for designs that accept large tilt angles and have a high tolerance to normal motion of the target plate becomes evident. A short focal length of the receiving lens will yield increased tolerance to tilt, while a receiving lens with a long focal length will result in an increased tolerance to decentering from accumulated normal displacement.

Optical Simulations

Further progress towards the optical design requires a more quantitative comparison of several optical configurations. Optical simulations that propagate electric fields (Zemax Physical Optics Propagation feature) were carried out to compute the fiber

coupling efficiency for varying amounts of normal displacement and target tilt. The fiber-optic lenses for the optical simulations were chosen based on typical PDV probes used for normal plate impact experiments [70]. Geometrical and optical properties of aspheric lenses with a focal length of f = 1.4 mm, 6.2 mm and 11 mm were sourced from Thorlabs and used as input for the optical simulations. Focusing probes were modeled by a collimator pair of f = 6.2 mm aspheric lenses for which the spot size at the rear target surface was minimized by adjusting the spacing of the lenses along the optical axis.

The coupling efficiencies between the source and the receiving side probes for two focused and two collimated optical configurations are shown in Fig. 5.3.

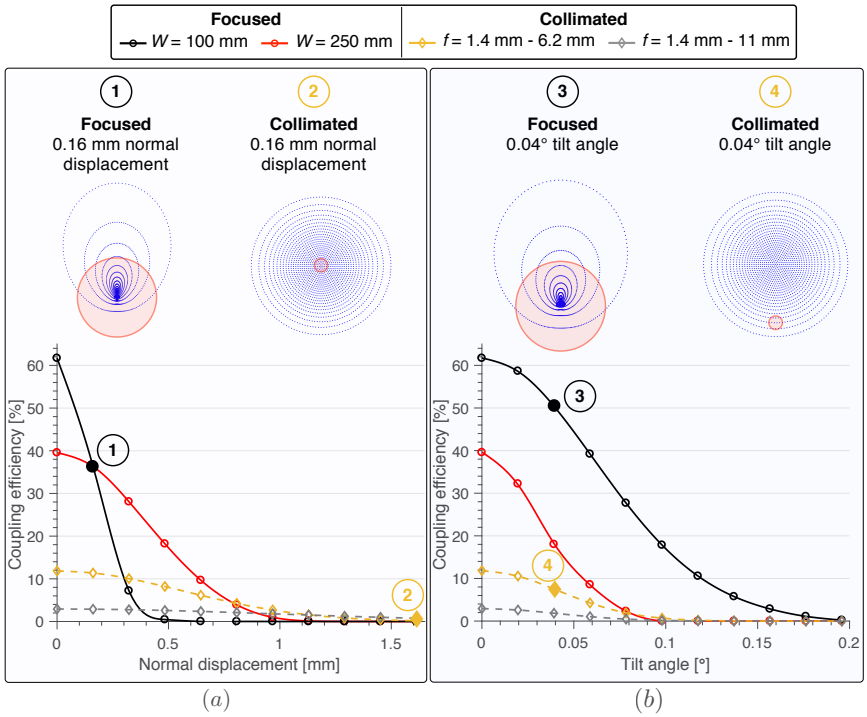

Figure 5.3: Optical simulation results in relation to (a) normal displacement and (b) tilt angle for focused and collimated fiber-optic designs with corresponding spot diagrams superimposed on the 8.2 μm diameter single-mode fiber (red circle).

Focused designs are characterized by their working distance W, whereas collimated designs are designated by their source and receiving probe lens focal length f. The final coupling efficiency for each receiving side probe can be obtained by multiplying the results displayed in Fig. 5.3 by the diffraction efficiency I_n, which depends on the diffraction grating design and is described in Section 5.2. Figure 5.3(a) shows, as mentioned in the previous geometrical analysis, that focusing probes will suffer from

a rapid loss of coupling efficiency upon normal motion of the target. Considering the immense light loss of the $W = 100$ mm focused design, it is not advisable to use working distances at or below this value for passive receiving probes. Figure 5.3(a) confirms that a focused configuration with a larger working distance W is less sensitive toward normal displacements of the target. As expected, the light loss designed into the collimated configurations yields a lower initial coupling efficiency. However, the small relative change of efficiency with target normal motion makes the collimated configuration more suited to transverse interferometry applications. Typical diagnostic systems can compensate for the lower initial coupling efficiencies with a higher source beam intensity.

The importance of achieving a low impact tilt during PSPI experiments with spectrally reflective surfaces is demonstrated in Fig. 5.3(b). As previously mentioned, especially short focal length focused configurations offer a higher tolerance to tilt than collimated systems. However, Fig. 5.3(b) confirms the result of the geometric analysis that using a short focal length source lens in a collimated system can provide a suitable tilt tolerance, which can surpass the absolute efficiency of a $W = 250$ mm focused systems at tilt angles above 1.5 mrad (0.085 °) and provide a much more constant light coupling. As a result of this analysis, a probe design that incorporates a $f = 1.4$ mm collimated source lens with a $f = 6.2$ mm receiving lens was selected, resulting in a collimation distance of 80 mm and beam diameter of 280 μm. The optimized probe design provides sufficient spatial resolution for most PSPI experiments.

In summary, the small relative change of coupling efficiency demonstrated by the collimated beam configuration (even as the target surface is normally displaced) suggests that collimating probes are more suitable for transverse velocimetry applications. The relatively low coupling efficiencies do not restrict the light available to the interferometer as ample laser power is available to obtain a diffracted light intensity, which is close to the damage threshold of the interferometer system.

Grating Design

A suitably designed diffraction grating can provide a high-intensity beam at diffraction angles θ_n in a range of $0° < \theta_n < 90°$. In conjunction with an appropriate optical design, the diffraction intensity I_n provided by the diffraction grating can be designed such that no additional electric or optical amplification is required.

Diffraction Angle

The diffraction angle is directly related to the resolution of the transverse velocity measurement. Assuming a normally incident source beam, the diffraction angle θ_n can be calculated by

$$d\sin(\theta_n) = n\lambda, \tag{5.2}$$

where d is the grating pitch, n is the diffraction order and λ represents the wavelength of the incident light beam. The resolution of a transverse velocimetry diagnostic is defined here as the inverse of the interferometer sensitivity $S = d/2n$ [64, 72]. Therefore the highest resolution is obtained for the lowest grating pitch that still produces the $\pm n^{th}$ diffraction order, i.e. for $d = n\lambda$.

Increased diffraction angles will, however, promote decentering of the diffracted beams by a distance $\Delta y = \Delta x \sin\theta_n$ with respect to the optical axis of the receiving probes, as previously addressed and depicted in Fig. 2(c). The maximum normal displacement Δx that is acceptable for successful measurement of transverse motion derived from the diffracted beams will thus be restricted. As a first order approximation, the accumulated normal displacement during a symmetric PSPI experiment can be estimated based on the observation time window T and the normal component of the impact velocity $V_0\cos(\psi)$, where ψ is the inclination angle of the target and flyer plate relative to its direction of travel, by $\Delta x = V_0\cos(\psi)T$. Considering an observation time window T, increased impact velocities V_0 will thus result in larger decentering values Δy leading to more challenging requirements for PSPI experiments at high impact velocities.

As discussed in Section 5.1, the acceptable degree of light loss, or a corresponding reduction in contrast of the interference signal will depend on the method of analysis, i.e. if the velocity record is obtained from analyzing signal phase or frequency. Optical simulations of the collimated probe configuration used in this study (f = 1.4 mm source probe, f = 6.2 mm receiving probe), reveal that diffracted beam decentering values of Δy of 0.41 mm, 0.63 mm and 0.75 mm will result in a light loss of 50%, 80%, and 90%, respectively. Decentering values assumed in the analysis are strictly attributed to normal displacement of the target rear surface and are independent of tilt. The corresponding amount of normal displacement associated with the 50%, 80%, and 90% light loss levels varies with the diffraction angle (or grating line density) as summarized by the colored curves in Fig. 5.4. The black curve in the figure represents the measurement resolution (as previously defined). A suggested method for interpreting the curves in Fig. 5.4 is to estimate

the maximum normal displacement (right vertical axis) that is accumulated during the observation time Δt of the experiment and find the intersection with the colored curves designating the acceptable degree of light loss considering the employed analysis technique. The corresponding diffraction angle (lower horizontal axis) or grating line density (upper horizontal axis) will then determine the maximum measurement resolution (left vertical axis). A diffraction grating with a pitch of

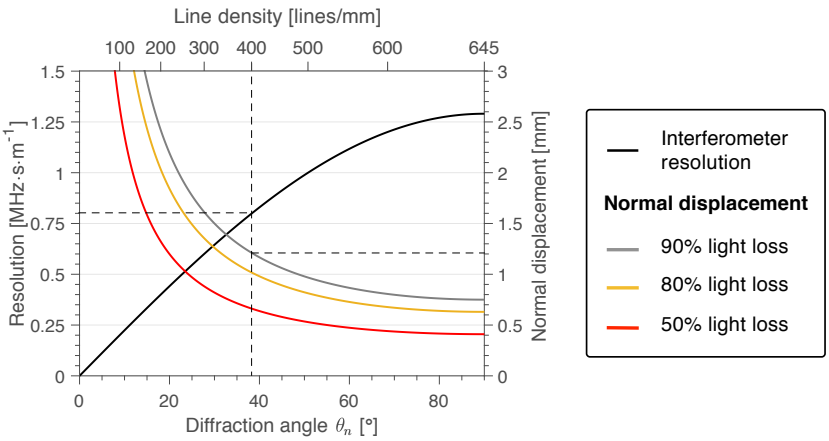

Figure 5.4: Plot of the transverse interferometer resolution and maximum normal displacement, assuming the previously described optical system, for different light loss thresholds as a function of diffraction angle θ_n.

$d = 2.5\,\mu$m ($\theta_1 = 38.32$ deg), highlighted in Fig. 5.4, was chosen for the experiments conducted in this study. This configuration provides a transverse velocity resolution of 0.8 MHz·s·m^{-1} and will experience a light loss of 90% at a normal displacement of 1.2 mm.

Diffraction Intensity

In addition to selecting the desired diffraction angle θ_n, the structure of the grating can be designed to obtain the desired intensity distribution into each diffraction order. For the purpose of this study only binary, reflective diffraction gratings, as shown in Fig. 5.5(a), were considered. For this case, the grating structure $l(x)$ can be represented by the following aperture function

$$l(x) = \begin{cases} e^{i\phi_1} = e^{i4\pi n_0 h/\lambda} & 0 \le x \le \beta d \\ e^{i\phi_2} = 1 & \beta d < x < d \end{cases}, \tag{5.3}$$

where ϕ_1 and ϕ_2 are phase terms associated with optical path length, n_0 is the refractive index of the medium that the incident light propagates in, h represents the step height, and β the duty cycle of the diffraction grating.

According to Fraunhofer diffraction theory [73], the intensity I_n of the n^{th} order diffracted beams resulting from a unity amplitude plane wave directed at normal incidence to the grating is given by the absolute square of the Fourier transform of the aperture function $l(x)$ and can be expressed as

$$I_n = \left| \int_0^{\beta d} e^{i\phi_1} e^{-2\pi i n x/d} dx + \int_{\beta d}^{d} e^{i\phi_2} e^{-2\pi i n x/d} dx \right|^2, \tag{5.4}$$

resulting in a 0^{th} order diffraction intensity of

$$I_0 = 2\beta^2 \left(1 + \cos\left(\frac{4\pi n_0 h}{\lambda}\right)\right), \tag{5.5}$$

and a diffraction intensity of the first order beams given by

$$I_1 = \frac{1}{\pi^2} \left(1 - \cos\left(\frac{4\pi n_0 h}{\lambda}\right)\right) \left(1 - \cos\left(2\pi\beta\right)\right). \tag{5.6}$$

Equation (5.6) reveals that a duty cycle of $\beta = 0.5$ results in the highest intensity for the $\pm 1^{st}$ order diffracted beams. In anticipation of pronounced light loss by the angled fiber-optic probes, more light should be directed into the $\pm 1^{st}$ order diffracted beams. The diffraction grating selected for this study has a duty cycle of $\beta = 0.5$ and a grating height of $h = 320$ nm resulting in a 0^{th} order efficiency of 7.3% and a 1^{st} order efficiency of 37.6% in both diffracted beams as highlighted by the intersections of the dashed black lines in Fig. 5.5.

The light response from the diffraction grating was further tailored for this study to increase the tolerance of the optical system to target tilt. This objective was achieved by designing a grating structure with slightly broadened diffraction lobes centered around the primary diffraction angle θ_1. Broadened lobes will thus contribute light to the fiber optic probe even as the diffracted beam is slightly inclined due to tilt induced rotation of the target rear surface. The novel grating structure has a varying pitch that steps from $d_h^i = 2.45$ μm to $d_h^i = 2.55$ μm in 5nm increments as depicted in Fig. 5.6(a). The varying pitch results in a corresponding range of diffraction angles $\theta_1 = 38.3 \pm 0.9°$ per Eq. (5.2). The feature width βd was varied accordingly to maintain a constant duty cycle of $\beta = 0.5$.

Furthermore, the diffracted lobes were also slightly broadened in the direction lying perpendicular to the primary diffraction plane to obtain an increased tolerance to

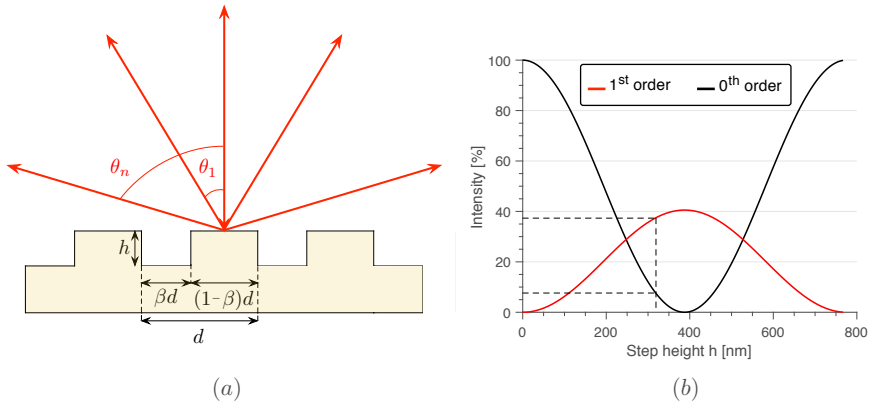

Figure 5.5: (a) Structure of a reflective binary diffraction grating and (b) its diffracted beam intensity as a function of step height h for a duty cycle β of 0.5.

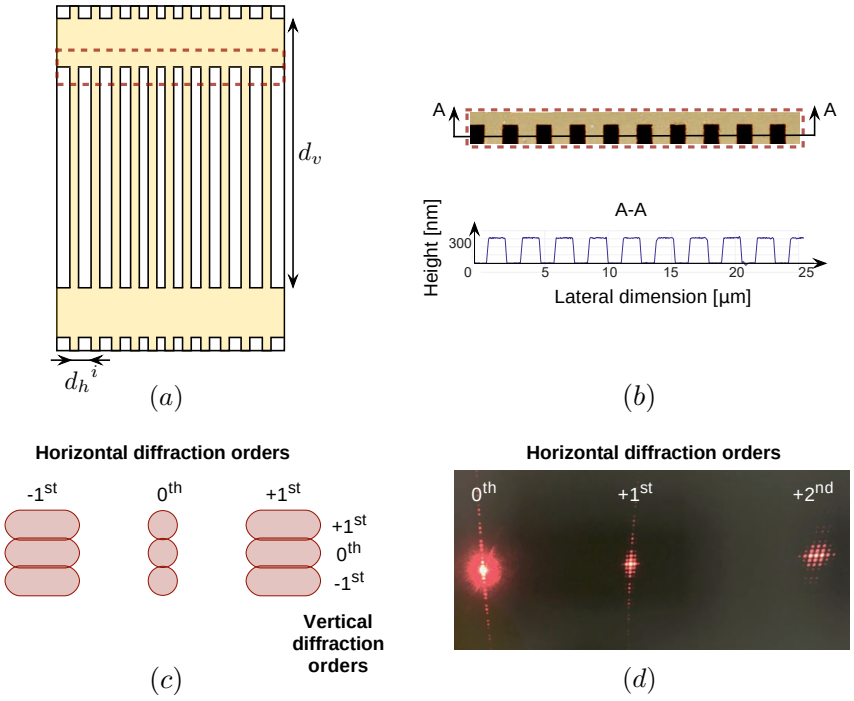

Figure 5.6: (a) Design of modified diffraction grating and (b) atomic force microscopy measurement of manufactured grating. (c) Schematic of designed light distribution around diffracted spots and (d) observed diffraction pattern under visible light (λ = 630 nm).

tilt in the orthogonal plane as well. Broadened diffraction lobes in the orthogonal direction were achieved by superimposing a coarse cross grating structure with a pitch of d_v = 80 μm and a duty cycle of 0.2, oriented perpendicular to the fine grating structure as shown in Fig. 5.6(a). The design freedom afforded by the e-beam

lithography technique, which is used to manufacture the grating structure, entails that only a new pattern drawing has to be created to generate the aforementioned modifications.

5.3 Heterodyne Transverse Interferometry

Two new and novel applications of heterodyning interferometer signals for transverse velocity measurements are described in Subsections 5.3 and 5.3. The light beams with different wavelength are created by either using a wavelength-tunable laser as a stationary reference beam or an acousto-optic frequency shifter that is applied to the $+1^{st}$ order diffracted light beam.

Diffracted Beam Photonic Doppler Velocimetry

Interferometer Design

The first approach is the fiber-optic DPDV arrangement, which is comprised of the drive, reference, and sensing groups as depicted in Fig. 5.7. The drive group hardware elements include a seed laser with an adjustable center wavelength between 1550 nm and 1570 nm, an Erbium-doped 2W booster stage, a 1 x 2 fiber-optic splitter, circulators (high-power model for 0^{th} order), attenuators, and fiber-optic collimating probes. PDV fiber-optic probes illuminate the leading edge of the sabot and rear surface of the target plate as shown in Fig. 5.7 and collect normally scattered and reflected light from each respective surface. A pair of DPDV "side probes" collect the symmetrically diffracted beams. The 0^{th} order beam and the scattered light from the sabot is passed through a fiber-optic circulator and all collected beams are redirected to variable attenuators before propagating to the sensing group elements as depicted in Fig. 5.7. Reference group hardware elements depicted in Fig. 5.7 generate the reference beams, which are interfered with the four collected drive group source beams. The reference light is produced by a fiber laser with an adjustable center wavelength between 1535 nm and 1580 nm and a power output of 40 mW. A reference beam wavelength of 1550.017 nm was selected for the DPDV validation experiment, which generated a constant carrier signal frequency of 0.66 GHz at zero particle velocity when mixed with the source light with a wavelength of 1550.012 nm. Sensing group hardware elements, depicted in Fig. 5.7, interfere the collected return light with the reference light and convert the resulting interference signals into digitized fringe records for analysis. The four Drive Group source beams are combined into PDV/DPDV beam pairs using two 1 x 2 Single Mode (SM) fiber-optic couplers as shown. The diffracted light beams are each initially

sent through a 4 km x 2 Network Simulation Module, which delays each beam by

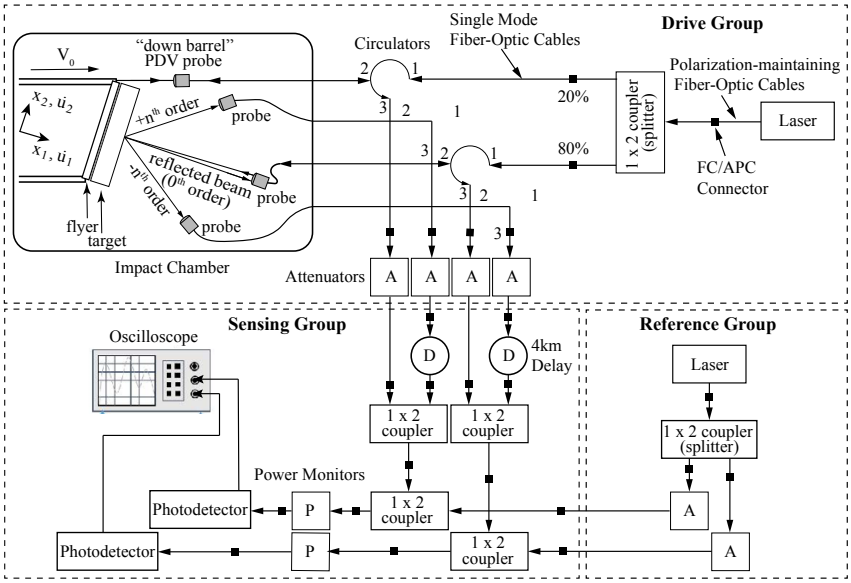

Figure 5.7: Schematic of DPDV system for combined measurement of normal and transverse particle velocities in PSPI experiments.

≈ 20 μs with respect to its PDV counterpart before the beams are combined. Each beam pair is then combined with a reference beam using a 1 x 2 SM fiber-optic coupler with a 10/90 coupling ratio. Interfering beam trains are each monitored by an in-line power monitor and terminate at a photodetector where the modulating light fields are converted into electrical signals. The time multiplexed PDV and DPDV interferometer signals are recorded using only 2-channels of a 4-channel oscilloscope to take advantage of the doubled sampling rate of 20 GSa/s.

Interferometer Sensitivities

Figure 5.8 depicts the oblique impact between a flyer and target plate in a PSPI experiment along with the reflected (0^{th} order) and symmetrically diffracted n^{th} order beams produced by the diffraction grating at the rear surface of the target plate. The ray diagram on the right hand side of Fig. 5.8 graphically depicts the optical path length change (δOPL) experienced by a normally reflected (0^{th} order) beam and a diffracted ($+n^{th}$ order) beam in response to infinitesimal normal and transverse displacements ($\delta u_1, \delta u_2$) of the target rear surface. The corresponding optical path length changes of the reflected and symmetrically diffracted $\pm n^{th}$ order beams are summarized in Fig. 5.8 under the assumption that the target rear surface displaced toward the detector as shown. The highly magnified optical ray diagram

on the right of Fig. 5.8 shows parallel horizontal rays impinging upon points A and A', which represent two rays out of a multitude of such rays that compose the incident collimated probe beam.

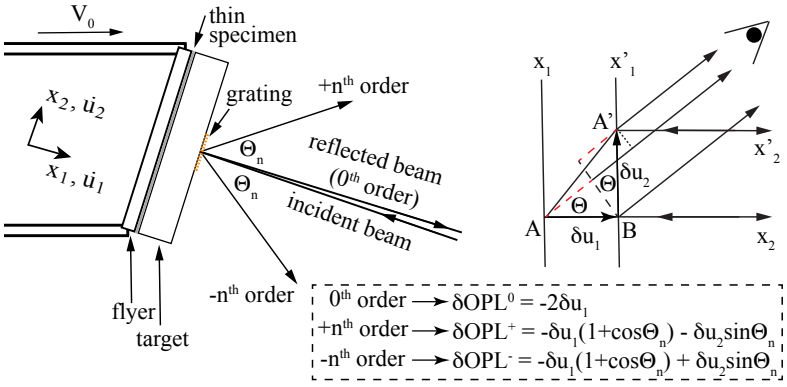

Figure 5.8: Changes in optical path length (OPL) of the 0^{th} order (reflected) and n^{th} order diffracted beams due to small (positive), normal and transverse displacements (u_1, u_2) of the target rear surface as point A displaces to A'.

DPDV measurement sensitivity is derived by invoking the two beam, time-averaged intensity formula

$$I \propto \left(\vec{E}_S + \vec{E}_R\right) \cdot \left(\vec{E}_S + \vec{E}_R\right)^* \tag{5.7}$$

where $\vec{E}_S$ and $\vec{E}_R$ are the electric field plane wave representations of the source and reference beams and the asterisk symbol denotes the complex conjugate operation [64]. Substituting for all time varying phase terms including those corresponding to changes in optical path length (OPL) of the $\pm n^{th}$ order diffracted beams, as shown in Fig. 5.8, leads to an expression for the time-averaged intensity of the heterodyned DPDV interference signals given by

$$I^{\pm}(t) = I_S^{\pm} + I_R^{\pm} + 2\sqrt{I_S^{\pm} I_R^{\pm}} \cos\left[\frac{2\pi}{\lambda_S}\left(u_1(t)(1-\cos\theta_n) \pm u_2(t)\sin\theta_n\right) + 2\pi(f_S - f_R)t - \phi^{\pm}\right]. \tag{5.8}$$

Here I_S and I_R represent the time-averaged steady state intensity of the source and reference beams, λ_S represents the wavelength of the source light, f_S and f_R are the optical frequencies of the source and reference light fields, and $\phi^{\pm}$ is a arbitrary constant phase in each interference signal. Application of a short-time Fourier transform algorithm to the recorded DPDV fringe records extracts the encoded

signal frequencies corresponding to

$$f^{+}(t) = \frac{1}{\lambda_S}\big(\dot{u}_1(t)(1+\cos\theta_n) + \dot{u}_2\sin\theta_n\big) + (f_S - f_R) \tag{5.9}$$

$$f^{-}(t) = \frac{1}{\lambda_S}\big(\dot{u}_1(t)(1+\cos\theta_n) - \dot{u}_2\sin\theta_n\big) + (f_S - f_R) \tag{5.10}$$

where $\dot{u}_1(t)$ and $\dot{u}_2(t)$ correspond to the normal and transverse particle velocity components.

Subtracting the two DPDV signal frequencies given by Eqs. (5.9), (5.10) and substituting for $\sin\theta_n$ from the grating Eq. (5.2) yields an expression for the transverse particle velocity in terms of the grating pitch (d), diffraction order (n), and the extracted signal frequencies given by

$$\dot{u}_2 = \frac{d}{2n}\big(f^{+}(t) - f^{-}(t)\big). \tag{5.11}$$

The frequency scaling factor $d/2n$ effectively represents the fundamental measurement sensitivity of the DPDV to changes in transverse velocity and is equivalent to the sensitivity of a transverse displacement interferometer [64]. Using the $\pm 1^{st}$ order beams from a 400 lines/mm grating in the current DPDV configuration results in a transverse velocity measurement sensitivity of 1.25 m/s/MHz.

Addition of the two DPDV signal frequencies given by Eqs. (5.9) and (5.10) yields an expression for the normal particle velocity in terms of the measured signal frequencies and the independently measured carrier frequency ($f_C = f_S - f_R$) given by

$$\dot{u}_1 = \frac{\lambda_S}{2(1+\cos\theta_n)}\big(f^{+}(t) + f^{-}(t) - 2f_C\big). \tag{5.12}$$

The scaling factor $\lambda_S/(2(1+\cos\theta_n))$ represents the fundamental measurement sensitivity of the DPDV to changes in normal velocity. DPDV is evidently $(1+\cos\theta_n)$ times more sensitive to changes in normal velocity compared to a standard PDV, which has a sensitivity of $\lambda_S/2$ [69]. Using the $\pm 1^{st}$ order beams of a 400 lines/mm grating in the current DPDV configuration results in a normal velocity measurement sensitivity of 0.434 m/s/MHz, which represents a factor of 1.78 increase over the sensitivity of the PDV when using the 0^{th} order beam at the same source wavelength.

Time Uncertainty of Signals

The uncertainty principle of signal processing, commonly referred to as the Heisenberg-Gabor limit [74], given by

$$\Delta t \Delta f \geq \frac{1}{4\pi}, \tag{5.13}$$

imposes a restriction on how well both signal frequencies f and their location in time t can be resolved. By examining Eq. (5.11) and (5.12) in this context, it becomes clear that adding or subtracting frequencies $f^{\pm}(t)$ that have an uncertainty about their position in time will introduce errors in determining the transverse $\dot{u}_2(t)$ and normal velocities $\dot{u}_1(t)$.

A synthetic example based on the analytical result of the Y-cut quartz validation experiment has been devised to demonstrate the issues arising from this approach. The ideal normal and transverse velocity records, with a rise time of 10 ns to transition between states, are depicted in Fig. 5.9(a). The velocity records are integrated over time to yield the corresponding displacements $u_1(t)$ and $u_2(t)$ that are subsequently inserted into Eq. (5.8) with a carrier frequency of $f_c = 1$ GHz to generate the synthetic light intensity signals $I^{\pm}$(t). An interferometer signal which more accurately reflects experimental results was generated by adding a noise term drawn from the standard normal distribution $\mathcal{N}(0, 1)$ with a signal noise fraction of 10%

$$I^{\pm}_{noise}(t) = I^{\pm}(t) + 0.1\ \mathcal{N}(0, 1)(t). \tag{5.14}$$

A short-time Fourier transform analysis with a $\tau = 25$ ns Hamming window was applied to the noise afflicted intensity signal generated by Eq. (5.14). Figure 5.9(c) shows the decoupled transverse $\dot{u}_2(t)$ and normal $\dot{u}_1(t)$ velocities that were calculated by Eqs. (5.11) and (5.12), respectively. It becomes evident that the velocity transient that coincides with the arrival of the first elastic wave, gives rise to artifacts as shown in Fig. 5.9(c). These artifacts become more dominant for cases where the transverse velocity is orders of magnitude slower than the normal velocity, which is typical for PSPI experiments.

Heterodyne Transverse Velocimetry

Interferometer Design

The second approach for designing a heterodyne transverse interferometer circumvents the issues related to the time uncertainty of frequency records, as discussed in Section 5.3, by optically decoupling the normal and transverse motion in a similar fashion to a transverse displacement interferometer [64]. The novelty of the HTV technique lies in the way it directly extracts the signal frequency through the use of robust frequency-based algorithms from a heterodyned transverse displacement interferometer, which by its very nature is purely sensitive to transverse motion. HTV is thus immune to signal artifacts that necessarily arise when frequency sig-

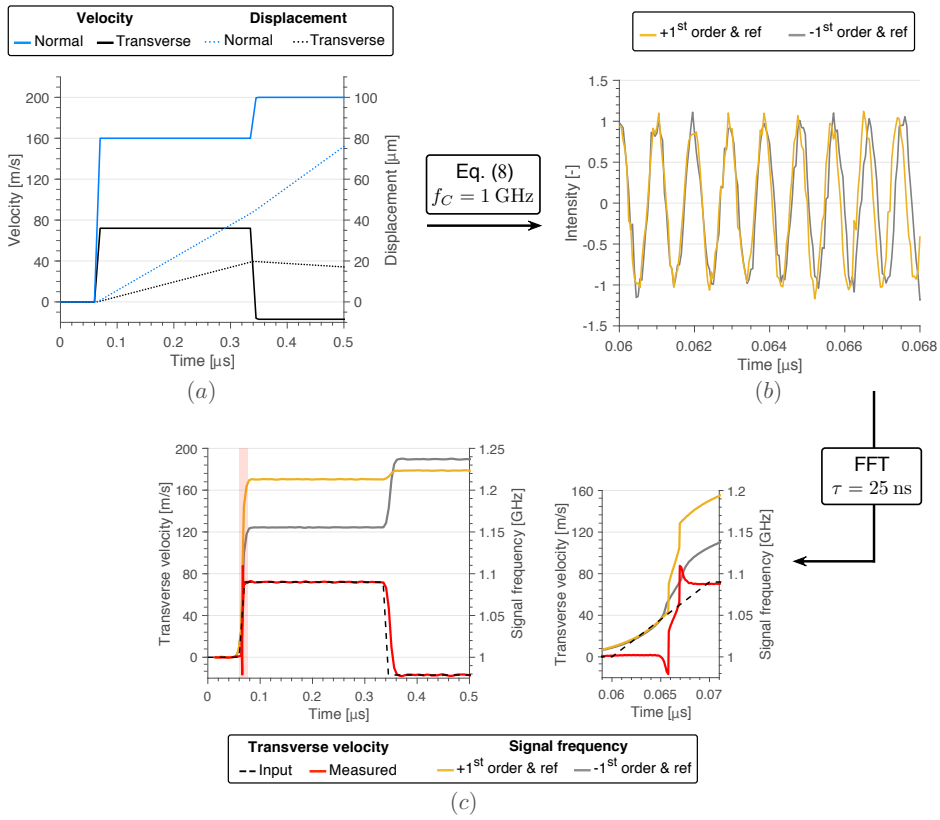

Figure 5.9: Synthetic experiment highlighting the limitations of superimposing frequency signals due to their time uncertainty. (a) Theoretical velocity and displacement profiles of Y-cut quartz validation experiment. (b) Fringe patterns of diffraction orders interfered with a stationary reference beam of different wavelength providing a carrier frequency of 1 GHz with a 10% noise fraction. (c) Result from frequency analysis with a 25 ns Hamming window, displaying artifacts during the QL wave transient associated with the superposition of frequency signals that are uncertain in time.

nals are added or subtracted to decouple motion components such as in the DPDV technique. That said, the DPDV technique has been shown to have the same sensitivity to transverse motion while offering increased sensitivity to normal motion compared to PDV. Each technique will thus have its advantages and disadvantages and it is left to the experimentalist to decide which technique to apply based on the experimental objectives and available instrumentation.

Many elements of the HTV interferometer are identical to the DPDV components. However, the HTV optical configuration shown in Fig. 5.10 relies on interference between the symmetrically diffracted $\pm 1^{st}$ order beams, which leads to modifications of the DPDV arrangement displayed in Fig. 5.7. As depicted in Fig. 5.10, the $+1^{st}$

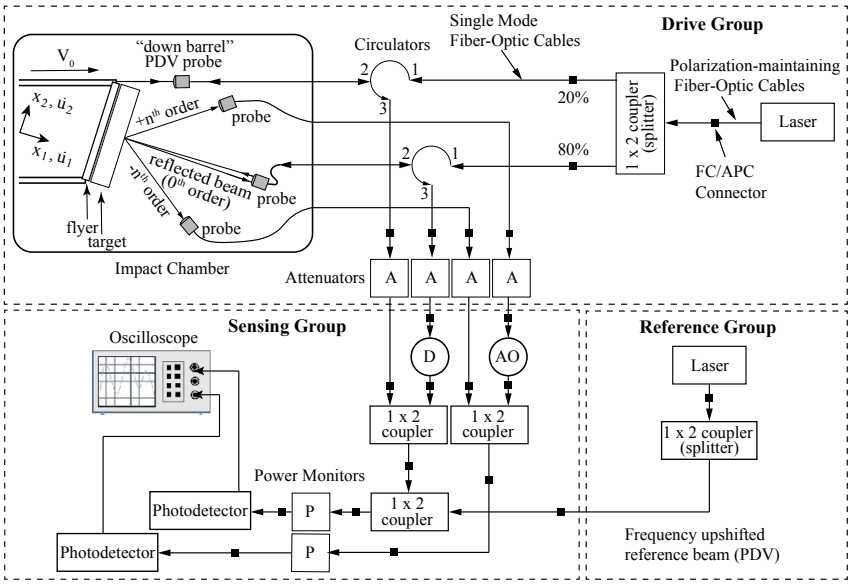

Figure 5.10: Schematic of HTV system for combined measurement of normal and transverse particle velocities in PSPI experiments.

order diffracted beam is passed through the acousto-optic frequency shifter, which provides a frequency shift equal to the frequency of the acoustic wave propagating inside its tellurium dioxide window. An up-shift frequency of 300 MHz was chosen as it offers an acceptable amount of light attenuation and enables the use of $\tau \geq 5$ ns analysis windows, resolving transients with 10%-90% rise times of $t_R \approx 2$ ns [69]. As previously mentioned, reducing τ further will lead to a higher frequency uncertainty, which is problematic for resolving the low transverse velocities observed in PSPI experiments.

Interferometer Sensitivities

As depicted in Fig. 5.10, the HTV interferometer interferes the $+1^{st}$ and -1^{st} diffracted order, which changes Eq. (5.8) to

$$I(t) = I_+ + I_- + 2\sqrt{I_+ I_-}\cos\left[\frac{2\pi}{\lambda_S}u_2(t)\sin\theta_n + 2\pi(f_+ - f_-)t - \phi\right]. \tag{5.15}$$

Equation (5.15) shows that the HTV scheme is insensitive to normal displacement and is therefore a pure transverse interferometer. Applying short-time Fourier transform analysis methods yields a signal frequency that is now directly related to the transverse velocity by

$$\dot{u}_2 = \frac{\lambda_S}{2\sin\theta_n}(f(t) - f_c) = \frac{d}{2n}(f(t) - f_c). \tag{5.16}$$

As expected, the fundamental sensitivity of the transverse displacement interferometer of $d/2n$ is recovered.

5.4 Experimental Validation

Wave Propagation in Anisotropic Crystals

A historical benchmark experiment used in the validation of the transverse displacement [64] and velocity interferometers (dual VISAR) [65] is to conduct a normal plate impact on a Y-cut quartz target. Due to the coupling of the shear and normal response of the anisotropic single crystal, both shear and pressure waves are generated during a normal impact experiment. This experiment creates very challenging conditions for interferometry systems such as rapid transients and velocity reversals in the transverse velocity record.

An analytic solution to the wave propagation in anisotropic media can be derived from the linear-elastic wave equation given by

$$\rho \frac{\partial^2 u_i}{\partial t^2} = C_{ijkl} \frac{\partial^2 u_k}{\partial x_j \partial x_l}, \tag{5.17}$$

where C_{ijkl} represents the fourth rank elastic moduli tensor, u_i is the displacement in the three Cartesian coordinates x_i, and ρ is the material density. Before lateral release waves arrive at the measured material point, the displacement u_i can be represented by a plane wave $u_i = U_i f(t - p_m x_m/c)$ with an arbitrary function f of wave velocity c, a vector denoting the propagation direction p_m and a relative displacement U_i. By inserting this plane wave ansatz into Eq. (5.17), the following eigenvalue problem can be formulated

$$(\Gamma_{ik} - \rho c^2 \delta_{ik}) U_i = 0, \tag{5.18}$$

where δ_{ik} is the Kronecker delta and Γ_{ik} represents the acoustic tensor, which is defined as

$$\Gamma_{ik} = C_{ijkl} p_j p_l. \tag{5.19}$$

The three eigenvalues of the acoustic tensor represent the product of the material density and the wave speed c_i for each corresponding eigenvector $\mathbf{U}^i$, which represent the polarization vectors of the three propagating waveforms. If no slip is assumed to occur during the experiment, the velocities and tractions are continuous across the flyer - target interface and the normal and transverse velocity - time profiles, given in Fig. 5.9(a), can be obtained. A more detailed description of elastic waves in anisotropic media can be found in Johnson [75].

As shown in Fig. 5.11, only two waveforms can propagate given the described conditions. The polarization vector of the fast wave commonly referred to as the quasi-longitudinal wave (QL), has its largest entry along the normal direction (y-axis of crystal), whereas the quasi-transverse wave (QT) is mainly polarized along the z-axis of the crystal.

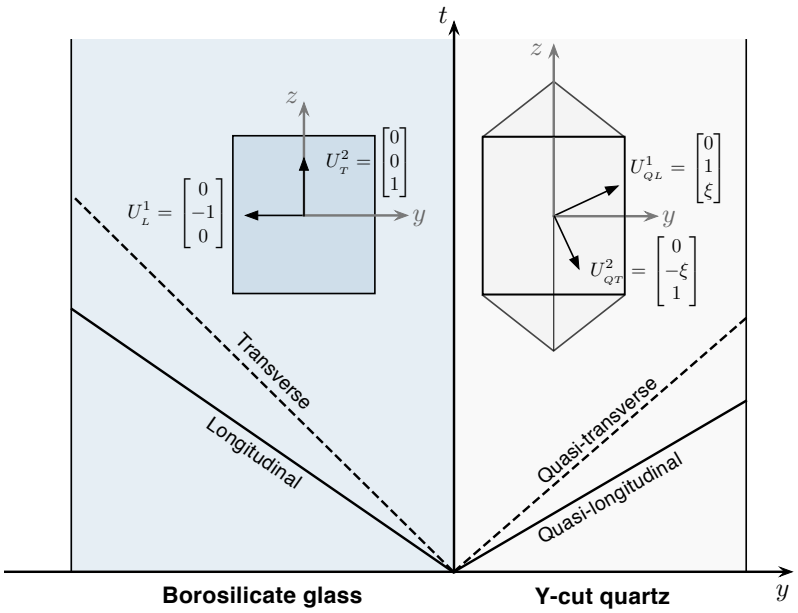

Figure 5.11: X-t diagram of normal impact experiment with a borosilicate glass flyer plate and Y-cut quartz target plate with polarization vectors $\mathbf{U}^i$.

Y-Cut Quartz Normal Impact Experiments

Pressure-shear normal impact experiments were conducted using borosilicate glass flyer plates and single-crystal Y-cut quartz target plates as a means of validating the DPDV and HTV interferometry techniques. Single-crystal Y-cut quartz was selected as a target material because of the strong coupling exhibited between longitudinal and transverse particle motion under normal impact. The predicted sharp positive velocity jumps in the transverse and normal directions upon arrival of the QL wave followed by negative jumps upon arrival of the QT wave presented an ideal scenario for evaluating various attributes of the transverse interferometer systems such as the predicted interferometer sensitivities and the optical heterodyne feature for automatic, accurate detection of velocity reversals.

Cylindrical Y-cut quartz plates were obtained with a diameter of 30 ± 0.1 mm, a thickness of 5 ± 0.1 mm and a Y-cut tolerance of ±0.17°. The target plate diameter was sufficiently large to provide an observation window of more than 2 μs before

lateral release waves reached the center of the target. The circumference of the Y-cut quartz plate included a 5 mm long flat that was manufactured to be parallel to the z-axis of the quartz crystal. Values for density and stiffness coefficients were taken from literature [76] and are as follows: density, $\rho = 2.65$ g/cm^3, $C_{22} = 87.16$ GPa, $C_{24} = 18.15$ GPa, $C_{44} = 58.14$ GPa, $C_{66} = 40.26$ GPa.

The choice of Borosilicate for the flyer plate material was based on three considerations: (a) choice of an isotropic material to simplify material alignment requirements, (b) a low acoustic impedance to generate relatively low stresses in both plates, and (c) sufficiently high yield strength in compression and shear to prevent premature failure of the flyer plate during the experiment. Cylindrical plates of Borofloat 33 glass were obtained with a diameter of 33.9 ± 0.1 mm and a thickness of 6.5 ± 0.1 mm. The flyer plate thickness was chosen to prevent wave reflections from the back side of the flyer plate from reaching the impact face prior to separation. Values for Borosilicate material constants were obtained from Schott North America and are given as follows: density, $\rho = 2.2$ g/cm^3; elastic Young's modulus, $E = 64$ GPa; Poisson's ratio, $\nu = 0.2$.

A 400 lines/mm gold diffraction grating was fabricated onto the backside of each target plate using metal vapor deposition and electron beam (e-beam) lithography. The first manufacturing step consists of depositing a 20 nm chromium adhesion layer followed by a 250 nm thick gold reflective layer. Gold exhibits very high reflectivity in the near infrared spectrum and does not suffer from oxidization, such as aluminum and silver. The creation of a high-quality optical grating lends itself well to a lift-off process, which is typically conducted with a bi-layer resist. After alignment of the 5 mm flat edge with the coordinate system of the e-beam lithography tool, the desired grating pattern is exposed and the bi-layers are individually developed to create a well-defined undercut resist profile. Subsequently, another gold layer of thickness $h = 320$ nm is deposited and residual resist features are dissolved, leaving an all gold diffraction grating on the target plate.

Experimental Results

Error Assessment

The accuracy of the velocimetry measurements is limited by the Heisenberg-Gabor limit (Eq. 5.13), the exact knowledge of the source laser wavelength λ_S, the digitizer time calibration and probe alignment to the designed angles [77]. Each probe alignment is conducted by maximizing the respective signal return. The cosine

corrections of the PDV measurements, utilizing the 0^{th} order diffracted beams, are assumed to be below 0.01% [77]. Considering the loss of coupling efficiency in the angled probes for tilt angles $\alpha > 0.5$ mrad, shown in Fig. 5.3, the uncertainty caused by small angle variations for the transverse velocimetry measurements is estimated to be below 0.08%. The uncertainty of the laser wavelength and the digitizer time measurement for these systems are typically below 10 ppm [77]. Based on these parameters, most of the uncertainty in velocimetry measurements is caused by identifying the peak frequency in the power spectrum of the short-time Fourier transform [77].

The assessment of the frequency uncertainty in this study follows Dolan's approach [69], which utilizes an analytically derived relation for the fitting of noise afflicted sinusoidal signals [78]. The resulting estimate of the frequency uncertainty Δf in a short-time Fourier transform analysis is based on the sampling frequency f_{sa} and the signal noise fraction σ of the velocimetry fringe records given by

$$\Delta f = \sqrt{\frac{6}{f_{sa}}} \frac{\sigma}{\pi} \tau^{-3/2}. \tag{5.20}$$

The signal noise fraction is estimated by [79]

$$\sigma^2 = \frac{1}{2} \frac{B f_N}{\int \left|\tilde{S}(f)\right|^2 df - B f_N}, \tag{5.21}$$

where B represents the mean (upper bound) noise level in the power spectrum of signal s(t) with its Nyquist frequency f_N and total area under its power spectrum $\int |\tilde{S}(f)|^2 df$.

The velocity uncertainty can then be deduced by multiplying the frequency uncertainty with the respective interferometer sensitivities

$$\Delta \dot{u}_i = S_i \sqrt{\frac{6}{f_{sa}}} \frac{\sigma}{\pi} \tau^{-3/2}, \; i = 1, 2. \tag{5.22}$$

As previously mentioned, the sensitivities for PDV and DPDV/HTV measurements are given by $S_1 = \lambda_S/2$ and $S_2 = d/2n$, respectively. As the DPDV technique relies on two frequency measurements to obtain the transverse velocity profile $\dot{u}_2(t)$, the uncertainty associated with both results has to be considered. Corresponding uncertainty values, calculated by Eq. 5.22, were included in the results obtained for each validation experiment.

Equation 5.22 also highlights the importance of the window length τ for conducting precise frequency measurements. A trade-off between the velocity uncertainty and time resolution, approximated by the 10-90% signal rise time $t_R \approx 0.37\,\tau$ (Hamming window function [69]), has to be taken into account for providing sufficient temporal resolution in the analysis of velocity time signals.

Diffracted Beam Photonic Doppler Velocimetry Measurements

Normal and transverse velocity profiles measured at the rear surface of the Y-cut quartz target plate using the DPDV diagnostic are plotted in Fig. 5.12. The velocity profiles were obtained from the acquired fringe records using a Hamming window duration of 50 ns with the window shifted one time step for every analysis (50 ps). The dashed lines represent the predicted velocity jumps of each respective motion component for a measured impact velocity of V_0 = 211 m/s. The measured QL and

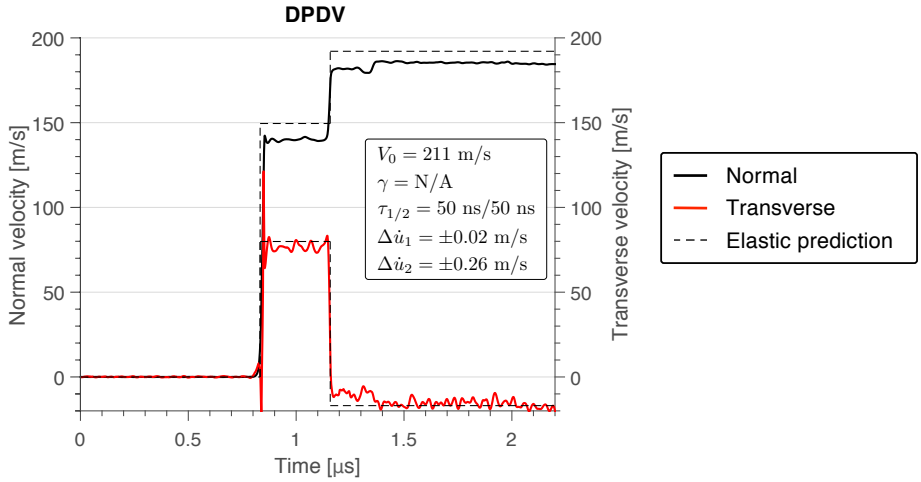

Figure 5.12: Measured longitudinal and transverse velocity profiles with PDV/DPDV interferometer compared to predicted values based on the measured impact speed of V_0 = 211 m/s.

final transverse QT velocity levels are in excellent agreement with theory while the measured normal velocity jumps both fell 3 – 4% short of their respective predicted values. Velocity measurements of the QL wave are sensitive to the impact tilt angle γ, but deviations in the final state can be attributed to uncertainty in the elastic stiffness constants used for the analysis. The tilt angle measurement was unsuccessful for this experiment, however, sufficient light return in the angled probes, as well as velocity measurements that are close to the elastic predictions, suggest an impact tilt γ below 2.5 mrad. As described previously, the time uncertainty of the DPDV signals leads

to artifacts during velocity transients, which occur with the arrival of the QL wave, as shown in Fig. 5.12.

Heterodyne Transverse Velocimetry Measurements

Figure 5.13(a) and (c) show a direct comparison of the fringe pattern observed during two different HTV experiments. The second experiment utilized a structured diffraction grating with slightly broadened diffraction lobes as described in Fig. 5.6. Due to a measured impact tilt of 2.2 mrad and distinct diffraction angles, the signal fringe contrast in the first experiment is reduced drastically with the arrival of the QL wave and almost vanishes with the appearance of the QT wave. In this region, only long window lengths of $\tau > 100$ ns can recover the transverse velocity information. However, the results of the second experiment, which utilized a structured grating,

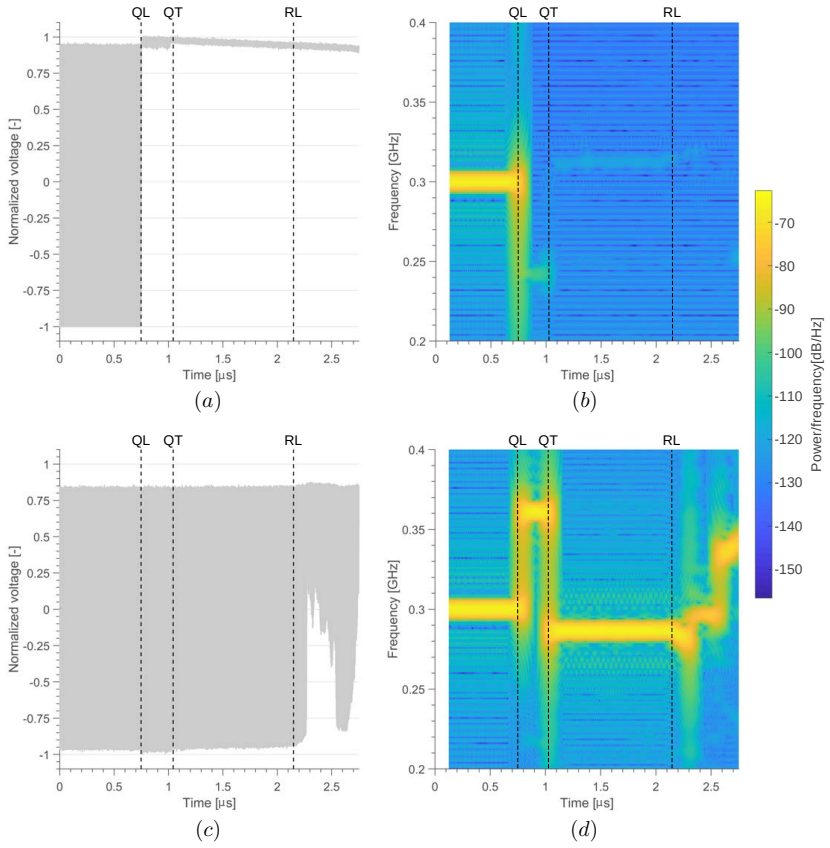

Figure 5.13: Comparison of fringe pattern and resulting spectrogram ($\tau = 250$ ns) of the experiment with a standard (a-b) and modified diffraction grating (c-d) according to Section 5.2. QL, QT, and RL denote the arrival of the quasi-longitudinal, quasi-transverse, and lateral release waves, respectively.

show an excellent fringe contrast even after the arrival of lateral release waves after

2.15 μs. Both the diffuse light response from the modified diffraction grating and a lower impact tilt value of 0.8 mrad contributed to maintaining a high coupling efficiency and hence a much improved fringe contrast. Comparing the spectrograms of both measurements in Fig. 5.13(b) and (d) illustrates the improvement in measurement uncertainty that is gained. Figure 5.13(b) and (d) reveal that the crystal axes in both experiments were oppositely oriented, which resulted in a reversed frequency response upon arrival of the QL and QT waves.

The measured normal and transverse velocities are depicted in Fig. 5.14. As previously discussed, no artifacts arise in the transverse velocimetry signals due to transients in the velocity profiles. Furthermore, the transverse velocity measurements vary considerably less around its respective steady-state value indicating a more precise measurement compared to the DPDV result [69]. The transverse velocity profile matches the theoretical prediction very well, while the final state in the normal velocity profile is measured to be 3-6% lower than the elastic prediction.

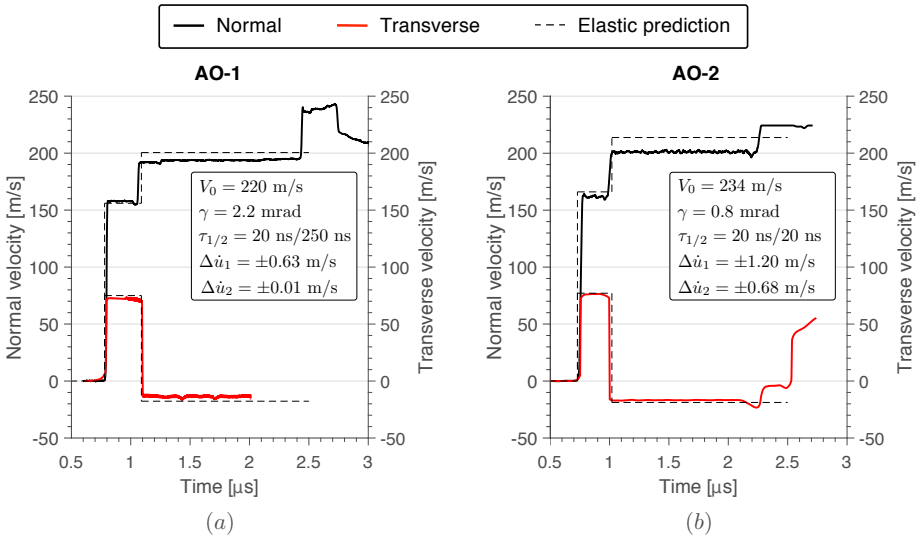

Figure 5.14: Measured longitudinal and transverse velocity profiles compared to predicted values in (a) the experiment with the standard grating at an impact velocity of V_0 = 220 m/s and (b) the modified grating experiment with V_0 = 234 m/s.

Orthogonality of Polarization Vectors

As previously discussed, the polarization vectors $\mathbf{U}^i$ are eigenvectors of the acoustic tensor. As the acoustic tensor governing this problem is real and symmetric, it is guaranteed to have orthogonal eigenvectors. This property provides an additional

opportunity to test the accuracy of the interferometer results by comparing the ideal orthogonality condition with the velocity jumps of the QL and QT waves.

The plot of transverse velocity $\dot{u}_2$ and longitudinal velocity $\dot{u}_1$ in Fig. 5.15 provides a graphical means of demonstrating this relationship and shows that the measured values of the transient and final velocity jumps are not perfectly orthogonal. The discrepancy mainly results from impact tilt, which affects the orientation of the polarization vectors. An impact with a tilt angle of 1.5 mrad (0.11°) and an impact velocity of $V_0 = 200$ m/s leads to an inclination of the propagating QL and QT waves to the y-axis of the quartz crystal of 2.6°, which is comparable to the observed deviation for the conducted experiments. The deviations from orthogonality are

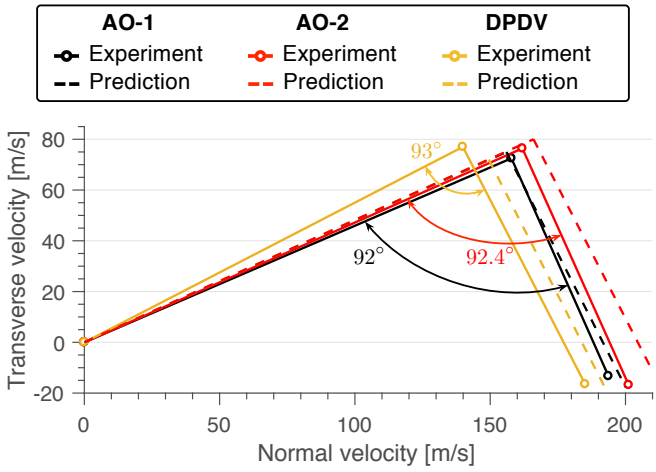

Figure 5.15: Orthogonality of the measured velocity jumps during the arrival of the QL wave and QT waves.

comparable for the HTV and DPDV experiments, with a slightly higher deviation in the DPDV experiments likely caused by a higher impact tilt angle γ. These values are respectively comparable to the 1.7° orthogonality deviation found by Kim & Clifton [64] in their study of transverse displacement interferometry with application to Y-cut quartz in which a measured tilt value of 0.4 mrad and an impact velocity of $V_0 = 50$ m/s were observed.

5.5 Conclusion

In this work, two new heterodyne interferometry techniques for PSPI experiments are presented: DPDV and HTV. The novelty in both interferometers lies in a carrier frequency f_c that is superimposed on the transverse velocity signals. Application of robust frequency-based fringe processing algorithms enables accurate measure-

ments of low velocities, with improved immunity to signal noise, and automatic detection of velocity reversal encountered in PSPI experiments. The DPDV technique provides an independent measure of normal particle velocity with an enhanced sensitivity compared to the PDV technique, but exhibits artifacts during rapid velocity transients, thus eliminating it from certain applications. The HTV technique does not suffer from the aforementioned issues and is, therefore, a superior transverse velocimeter, which manifests itself in more precise measurements. However, HTV is unable to provide additional information on the normal velocity record. The design and implementation of collimating fiber optic probes combined with structured diffraction gratings, engineered at the nano-scale, counteract coupling losses related to decentering and tilt of diffracted beams and effectively eliminate the need for additional electric or optical amplification. The validation impact experiments on Y-cut quartz showcased the efficacy of the optical design and interferometer techniques as challenging velocity transients and reversals were well resolved and showed good agreement with theoretical predictions.

These key developments will enable PSPI experiments at higher pressures (> 25 GPa), which will ultimately enhance our understanding of material strength in extreme environments and across phase transformations. Although these developments are presented in the context of PSPI experiments, both heterodyne velocimetry techniques can be effectively used for measuring normal and transverse velocities associated with other dynamic phenomena, including laser-driven shocks and magnetically-applied pressure-shear loading.

Chapter 6

EXPERIMENTAL RESULTS

6.1 Summary of Experimental Parameters

Table 6.1 summarizes the experimental parameters for the pressure-shear plate impact (PSPI) experiments conducted at Caltech (CK) and Brown University (TJ). The PSPI experiments at Brown University were carried out by Dr. Tonia Jiao in Professor R. J. Clifton's laboratory. The parameters and the results of the PSPI experiments at Brown University are shown here as a comparison to the experimental results on soda-lime glass obtained at Caltech. The soda-lime glass samples and tungsten carbide (WC) anvil plates employed at both experimental facilities were produced by the same manufacturer to identical specifications. Pure tungsten carbide plates were sourced from BAE Systems for experiment TJ-0103, CK-1901 and CK-1902, whereas the Basic Carbide Corporation manufactured the remaining tungsten carbide plates with a cobalt content of 3%. The 5 μm thick soda-lime glass samples were vapor-deposited by Thin-Films Research Inc., and the 100-300 μm thick samples were obtained from Valley Design, Corp. All experiments were con-

Experiment	Thickness [mm]			V_0 [m/s]	σ_{peak} [GPa]	Tilt [mrad]
	Glass	Flyer	Target			
TJ-0103	-	7.98	5.93	488	20.5	-
TJ-1602	0.005	6.39	3.97/5.92	194	9.3	0.5
TJ-1603	0.005	6.39	3.95/5.90	188	9.0	0.4
TJ-1802	0.005	6.43	3.95/5.88	483	21.2	1.9
CK-1701	0.005	4.98	2.01/3.77	736	31.4	N/A
CK-1801	-	4.97	3.85	863	36.9	3.4
CK-1802	0.005	4.97	1.96/3.81	640	27.2	N/A
CK-1803	0.005	4.97	1.96/3.78	606	25.8	0.8
CK-1804	-	4.99	3.91	617	26.5	0.5
CK-1805	0.005	4.91	1.59/3.96	317	14.1	1.0
CK-1806	-	4.97	3.93	319	14.1	0.3
CK-1807	0.3	4.97	1.96/3.70	328	14.5	0.3
CK-1808	0.1	4.96	1.96/3.70	330	14.5	0.8
CK-1901	-	4.97	3.94	631	26.9	0.2
CK-1902	-	4.99	3.95	611	26.9	1.5

Table 6.1: Experimental parameters for PSPI experiments conducted at Caltech (CK) and Brown University (TJ)

ducted with an inclination angle ψ of 18°, except experiment TJ-0103 and TJ-1802 which utilized a 16° angle and CK-1902 that employed a 12.5° angle. TJ-0103, CK-1801, CK-1804, CK-1806, CK-1901 and CK-1902 were symmetric PSPI experiments conducted on tungsten carbide anvil plates, whereas the other experiments involved varying thicknesses of soda-lime glass sandwiched between tungsten carbide front and rear target plates. The peak normal stress in the experiments σ_{peak} is calculated using the tungsten carbide material model discussed in Section 7.4.

6.2 Symmetric PSPI Experiments on Tungsten Carbide Anvil Plates

A detailed description of the dynamic material behavior of tungsten carbide was obtained through symmetric PSPI experiments at different pressures. Figure 6.1 shows the recorded fringe signals of the PDV and HTV diagnostics during experiment CK-1806 (V_0 = 319 m/s) on tungsten carbide. The carefully designed optical

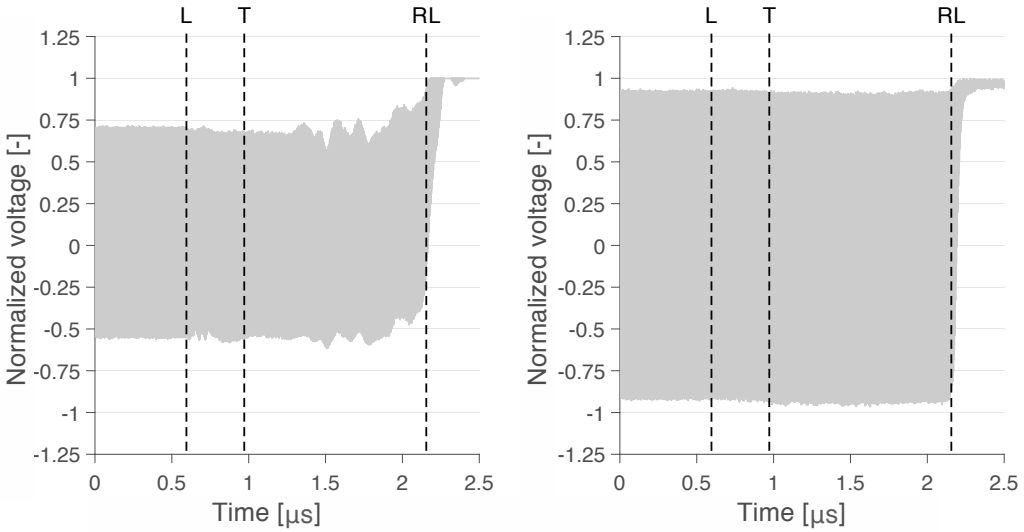

Figure 6.1: Interference fringe pattern of (a) PDV and (b) HTV diagnostics during symmetric tungsten carbide PSPI experiment CK-1806. The arrival of the longitudinal (L), transverse (T) and release wave (RL) are highlighted by vertical, dashed lines.

system, described in Chapter 5, and a low impact tilt angle γ provide very stable fringe amplitudes that maximize the signal to noise ratio σ and minimize the corresponding measurement error, according to Eq. 5.22. The upper bound on the errors in all Caltech experiments are comparable and lie between ±0.17 m/s - ±0.89 m/s and ±0.22 m/s - ±0.68 m/s for the normal and transverse velocitiy measurements, respectively. The fringe records for all PSPI experiments conducted at Caltech are

analyzed using short time Fourier transforms as described in Chapter 5, with Hamming windows of 20 ns and 50 ns duration for the normal and transverse velocity records, respectively. The resulting normal and transverse velocities for experiment CK-1806 are depicted in Fig. 6.2.

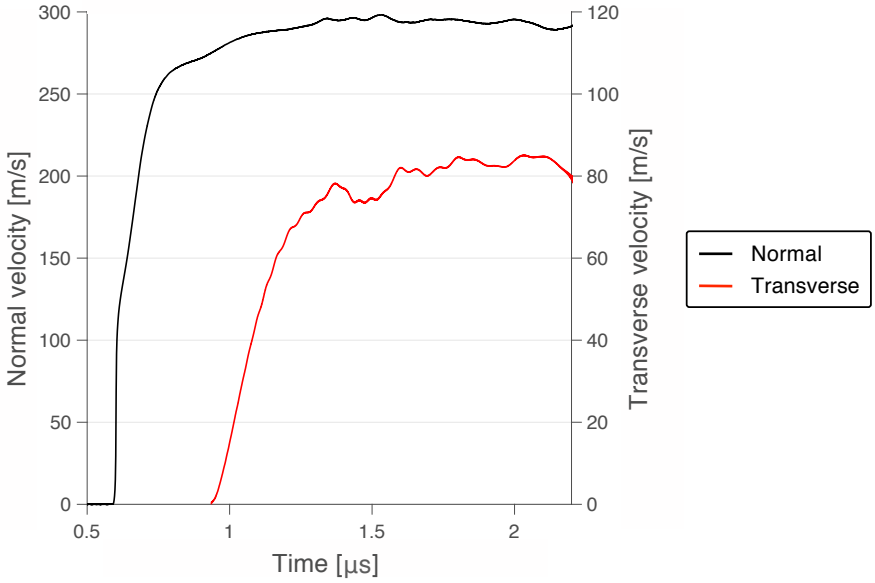

Figure 6.2: Normal and transverse free surface velocity measurements of symmetric tungsten carbide PSPI experiment CK-1806.

The normal velocity signal shows the signature of a Hugoniot elastic limit (HEL) at approximately 115 m/s or 6.1 GPa, which is consistent with the range of reported values, 6.6 ± 0.5 GPa [28]. The evolution of the plastic wave shows a large amount of hardening with characteristic wave profiles before reaching its slightly unsteady final value. The transverse velocity result exhibits a visibly spread out shear wave up to approximately 70 m/s followed by a gradual increase to a peak value of 85.1 m/s.

Figure 6.3 depicts the normal and transverse velocities of symmetric tungsten carbide experiment CK-1804, which was conducted at a higher impact velocity of V_0 = 617 m/s. The HEL and rise of the plastic wave, visible in the normal velocity signal, are comparable to those observed in experiment CK-1806. The steady-state exhibits a less erratic response with a small positive slope. The transverse velocity reaches a much smaller peak value of 12.1 m/s with a subsequent steady decline towards a transverse velocity of 7.6 m/s. The change in shearing resistance of tungsten carbide at impact velocities above 600 m/s, is confirmed by two PSPI experiments,

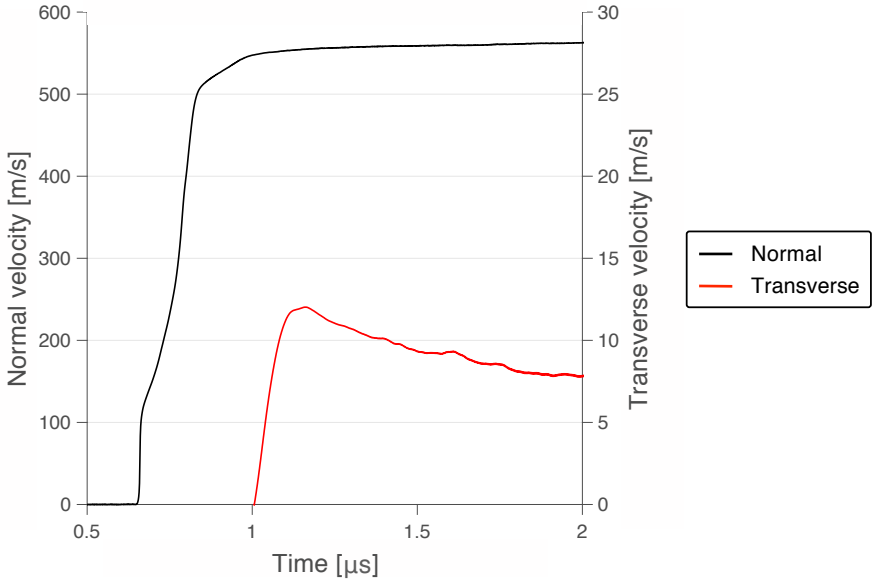

Figure 6.3: Normal and transverse velocity measurements of symmetric tungsten carbide PSPI experiment CK-1804.

CK-1802 and CK-1803, conducted on a 5 μm thick soda-lime glass layer sandwiched between tungsten carbide front and rear target plates. A comparison of the normal and transverse velocity measurements is depicted in Fig. 6.4, for which the normal and transverse signals of experiment CK-1804 have been shifted in time to coincide with experiments CK-1802 and CK-1803.

The thin glass layer equilibrates to the same normal stress as the tungsten carbide anvils within a few nanoseconds, rendering its effect on the normal response of the target assembly negligible. The normal velocity profiles of experiments CK-1802 (V_0 = 640 m/s) and CK-1803 (V_0 = 606 m/s) coincide for a large part of the plastic wave structure demonstrating the repeatability of both the onset and evolution of the inelastic behavior of the tungsten carbide material.

For large anvil to sample strength ratios, the measured transverse velocities are largely governed by the sample behavior. However, the low shearing resistance in experiment CK-1806 and the direct correlation between impact and peak transverse velocities in all three experiments suggest a loss of strength of the tungsten carbide anvil plates. Experiments CK-1802 and CK-1803 are therefore not indicative of material behavior exhibited by the 5 μm thick glass layer, but likely represent a measurement of the strength of tungsten carbide at normal stresses exceeding 25 GPa. All experiments exhibit a common steady state shearing resistance suggesting

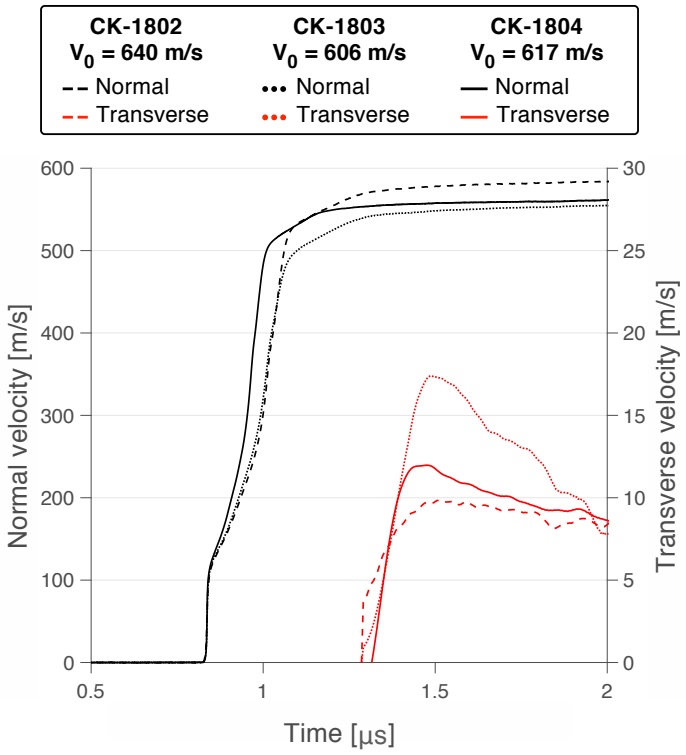

Figure 6.4: Comparison of normal and transverse velocity profiles of symmetric tungsten carbide PSPI experiment CK-1804 with soda-lime glass experiments CK-1802 and CK-1803.

a distinctive strength of tungsten carbide at this pressure level.

Symmetric PSPI experiments were conducted on pure tungsten carbide anvils to constrain the mechanisms for the loss of shearing resistance at normal stresses exceeding 25 GPa. All three experiments, displayed in Figure 6.5(a), show the increased Hugoniot elastic limit of pure tungsten carbide at approximately 160 m/s. Figure 6.5(b) highlights a similar loss of strength, between PSPI experiments at normal stresses of 20.5 GPa and 26.9 GPa, as observed in the cemented tungsten carbide material. The skew angle in experiment CK-1902 (12.5°) was chosen such that the normal stress was identical to the low shearing resistance experiment CK-1901 while maintaining the transverse velocity of the high strength experiment TJ-0103. The results of the PSPI experiment CK-1902 in Figure 6.5(b) show an intermediate shearing resistance characterized by a plateau value slightly below 30 m/s.

Figure 6.6 depicts the normal velocity measurements of experiments CK-1701 and CK-1801, conducted at even higher impact velocities of 736 and 863 m/s, respec-

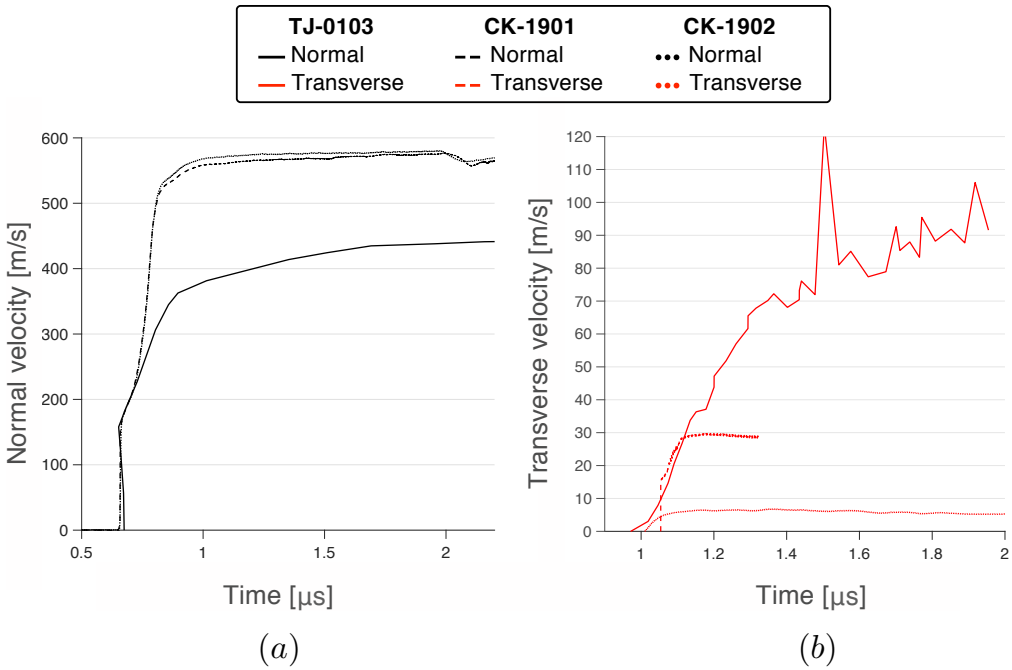

Figure 6.5: Normal and transverse velocity measurement of PSPI experiment TJ-0103, CK-1901 and CK-1902 on . The inset highlights a subtle waveform visible in the higher velocity PSPI experiments. The arrival time of experiment CK-1701 was translated in time for comparison.

tively. The transverse velocity measurements were unsuccessful in both experiments due to a loss of light coupling into the DPDV (CK-1701) and HTV diagnostic (CK-1801). The DPDV diagnostic in experiment CK-1701 was able to recover a weak transverse velocity signal. However, the high signal to noise ratio prohibited a meaningful measurement of material behavior. A high impact tilt during the experiments is likely the cause for the light coupling losses as it more strongly affects the transverse than the normal velocity measurements. The similar evolution of the normal velocity profiles suggests that the same hardening mechanisms persist at higher pressures and strain rates. Moreover, a distinct waveform is observed during the build-up of the plastic wave in the higher impact velocity experiments (V_0 >330 m/s), which is illustrated by the inset of Fig. 6.6 and further discussed in Chapter 7.

6.3 PSPI Experiments on Soda-Lime Glass Samples

The pressure-shear response of soda-lime glass was investigated in a total of six experiments. Four experiments provided information regarding the pressure dependence of the material behavior by subjecting the samples to three different levels of normal stress (9, 14 and 21 GPa), while two experiments isolated the effect of strain

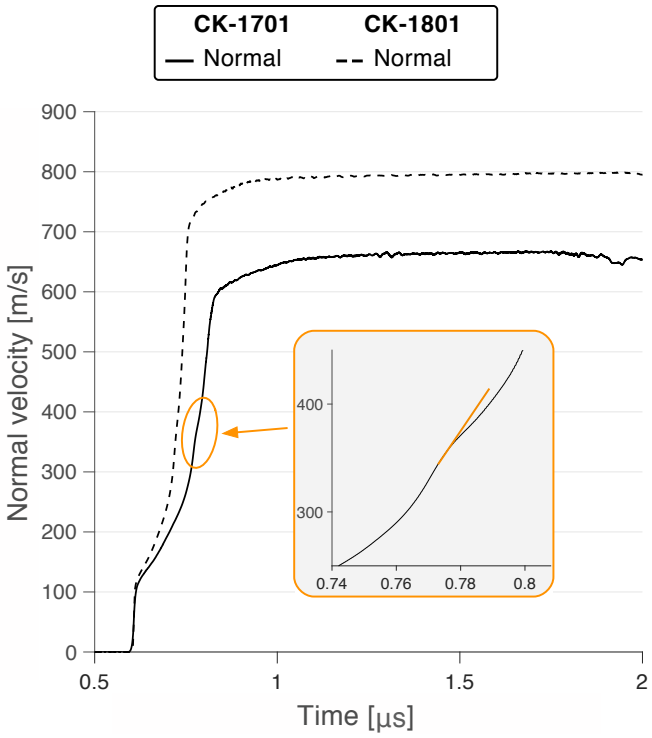

Figure 6.6: Normal velocity measurement of PSPI experiment CK-1701 and CK-1801. The inset highlights a subtle waveform visible in the higher velocity PSPI experiments. The arrival time of experiment CK-1701 was translated in time for comparison.

rate by studying three different sample thicknesses (5, 100 and 300 μm) at constant normal stress.

The experiments TJ-1602, TJ-1603 and TJ-1802 were conducted on single-stage gas guns at Brown University. A 63.5 mm diameter gun with a maximum impact velocity of ~200 m/s was employed for experiments TJ-1602 and TJ-1603, whereas a 102 mm diameter gun with a maximum impact velocity of ~500 m/s was utilized for the higher velocity experiment (TJ-1802). These experiments rely on the normal (NDI) and transverse displacement interferometer (TDI) for the combined measurement of normal and transverse free surface velocities [64], respectively. These three PSPI experiments are summarized in Fig. 6.7.

The HEL of the tungsten carbide anvil plates in all three experiments, depicted in Fig. 6.7 (a), is comparable to the experiments conducted at Caltech. Experiments TJ-1602 and TJ-1603 exhibit a sigmoidal normal velocity increase following the initial elastic response as the maximum normal stress only slightly exceeds the HEL of the tungsten carbide anvil plates. Due to the thin sample layer (5 μm), the normal

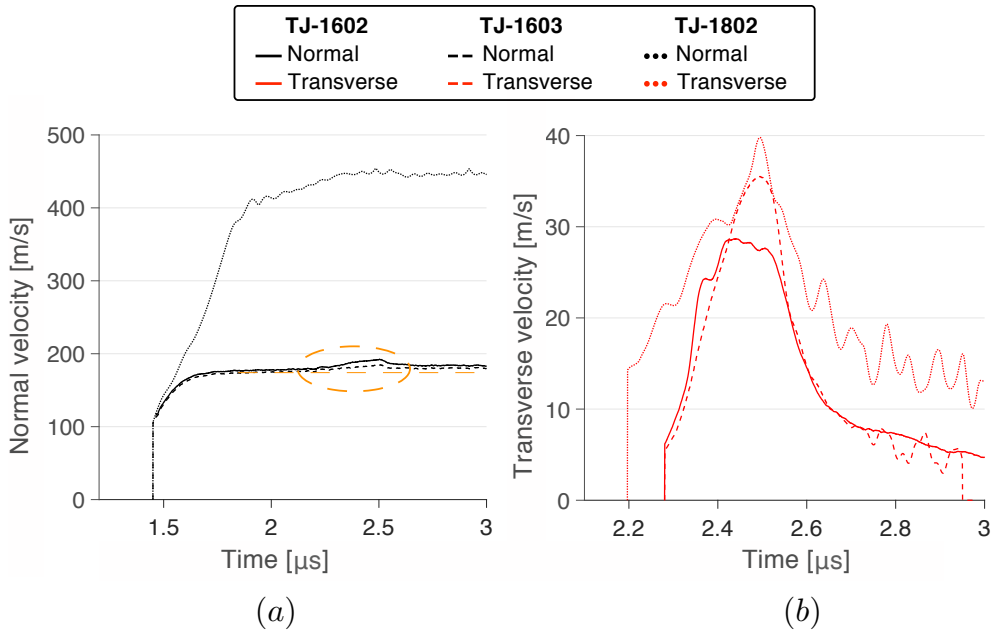

Figure 6.7: (a) Normal and (b) transverse velocity measurements during soda-lime glass PSPI experiments TJ-1602, TJ-1603 and TJ-1802. The increase in normal velocity following a plateau region is highlighted for experiments TJ-1602 and TJ-1603. The transverse velocity profile of experiment TJ-1802 was displaced in time to facilitate comparison.

response of experiment TJ-1802 shows a noticeable resemblance to the behavior obtained in the symmetric tungsten carbide experiments, discussed in Section 6.2.

The transverse velocity measurements of experiments TJ-1602 and TJ-1603 agree remarkably well with the exception of an observed velocity plateau of approximately 28 m/s during experiment TJ-1602 in contrast to a peak velocity of 36 m/s in experiment TJ-1603. Slip at the anvil-sample interfaces constitutes the most likely explanation for the constant inelastic shear response in experiment TJ-1602 since a precipitous reduction in transverse velocity, as observed in TJ-1603, is expected to occur. At higher pressures, experiment TJ-1802 exhibits an increase in peak transverse velocity to 40 m/s. However, the rise time and drop in transverse velocity change considerably in comparison with the observed behavior in experiments TJ-1602 and TJ-1603. A higher final transverse velocity, following a precipitous drop, indicates a pressure dependent failed strength of soda-lime glass, as observed in manganin gauge strength measurements at lower pressures [18, 49]. The longer rise time and oscillating wave profile suggest the onset of damage in the tungsten carbide anvils, which might have affected the inferred sample properties in this experiment.

The impact velocity of experiments CK-1805, CK-1807 and CK-1808, depicted in Fig. 6.8, were set to resemble the conditions experienced by experiment CK-1806, during which tungsten carbide was shown to retain most of its strength. The normal velocity record of experiment CK-1805 exhibits analogous behavior to the

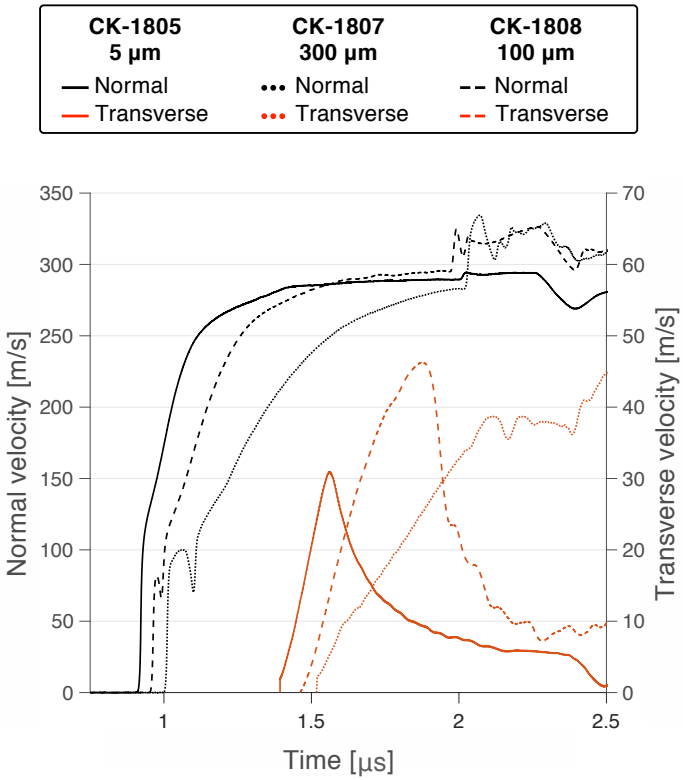

Figure 6.8: Normal and transverse velocity measurements of symmetric PSPI experiments on soda-lime glass: CK-1805, CK-1807 and CK-1808.

symmetric impact experiment on tungsten carbide (CK-1806) due to the negligible effect of the 5 μm thick glass layer on the normal response of the target assembly. The small increase in the normal velocity record at approximately 2 μs, coincides with the arrival of a reflected wave from the rear target-sample interface highlighted in Fig. 4.5. The recompression is caused by the lower impedance of the glass sample in comparison to the tungsten carbide rear target plate. The transverse velocity shows an almost linear rise to a peak value of 31 m/s followed by an equally sharp release and a gradual reduction to a constant transverse velocity of 5.3 m/s.

The normal velocity record of PSPI experiment CK-1808 shows an immediate dip in velocity, from 82 m/s to 66 m/s, following the propagation of the initial compression wave with immediate recompression observed after the arrival of the first reverberation inside the sample layer. The effect of the 100 μm thick sample

layer on the normal velocity profile is much more pronounced as it leads to significant rounding of the signal. The recompression wave at 2 μs is more evident than in experiment CK-1805 due to the longer reverberation time inside the thicker sample. A peak transverse velocity of 46 m/s is observed followed by a precipitous drop in shearing resistance approaching a velocity of approximately 8.5 m/s in its final, failed state. Although the shear strain rate is well below that of experiment CK-1805, the slope of the transverse velocity signals is comparable indicating strong shear wave spreading in the tungsten carbide anvils.

The normal velocity record of experiment CK-1807 shows an even more significant ramp loading, with an increase in sample layer thickness (300 μm), owing to the compressibility anomaly discussed in Section 2.1. The anomalous drop following the initial compressive wave persists and becomes more pronounced as it falls from a normal velocity of 100 m/s to a local minimum of 70 m/s. The increased sample thickness leads to a much-reduced shear strain rate, which is demonstrated by a prolonged rise time of the transverse velocity profile. A transverse velocity plateau of approximately 39 m/s is reached after 2.1 μs, which, as previously mentioned, is likely a sign of slip at the sample-anvil interfaces.

Chapter 7

NUMERICAL MODELING OF PRESSURE-SHEAR PLATE IMPACT EXPERIMENTS

If one assumes a linear-elastic material behavior of the anvil plates and a uniform stress distribution inside the sample layer, a well-established procedure exists to obtain the stress-strain relation for the material of interest in the pressure-shear plate impact (PSPI) experiments [80] and no further modeling is required. This chapter details the motivation for and implementation of numerical modeling tools to infer sample properties when normal stresses during high-pressure PSPI experiments exceed the elastic limit (HEL) of the utilized anvil plates.

7.1 Motivation

The following sections provide insight into the fundamental challenges for the analysis of PSPI experiments that arise as a consequence of the change in behavior of yielding materials under combined normal and shear loading.

Dynamic Material Behavior under Combined Normal and Shear loading

PSPI experiments on isotropic materials give rise to combined uniaxial compression and simple shear loading. The strain $\boldsymbol{\varepsilon}$ and stress $\boldsymbol{\sigma}$ tensors under these conditions (coordinate system defined in Fig. 7.1 (a)) are given by

$$\boldsymbol{\varepsilon} = \begin{pmatrix} \varepsilon_{xx} & \epsilon_{xy} & 0 \\ \epsilon_{xy} & 0 & 0 \\ 0 & 0 & 0 \end{pmatrix}, \qquad \boldsymbol{\sigma} = \begin{pmatrix} \sigma_{xx} & \tau_{xy} & 0 \\ \tau_{xy} & \sigma_{yy} & 0 \\ 0 & 0 & \sigma_{zz} \end{pmatrix}. \tag{7.1}$$

For materials that exhibit a linear elastic response, Hooke's law

$$\sigma_{ij} = 2G\epsilon_{ij} + \lambda\epsilon_{kk}\delta_{ij} \tag{7.2}$$

can be used to obtain the lateral confinement stresses σ_{yy} and σ_{zz} as a function of the material's Poisson's ratio ν and the longitudinal stress σ_{xx}

$$\frac{\sigma_{yy}}{\sigma_{xx}} = \frac{\sigma_{zz}}{\sigma_{xx}} = \frac{\nu}{1-\nu}. \tag{7.3}$$

Under symmetric impact conditions, as depicted in Fig. 7.1 (a), the normal and shear stresses can be obtained by [3]

$$\sigma_{xx} = -\frac{(\rho c_1)\cos(\psi)V_0}{2} \tag{7.4}$$

and

$$\tau_{xy} = -\frac{(\rho c_2)\sin(\psi)V_0}{2}. \tag{7.5}$$

The ratio of shear to normal stresses is therefore given by

$$\frac{\tau_{xy}}{\sigma_{xx}} = \sqrt{\frac{(1-2\nu)}{2(1-\nu)}}\tan(\psi). \tag{7.6}$$

The resulting state of stress is represented by a Mohr's circle in Fig. 7.1 (b).

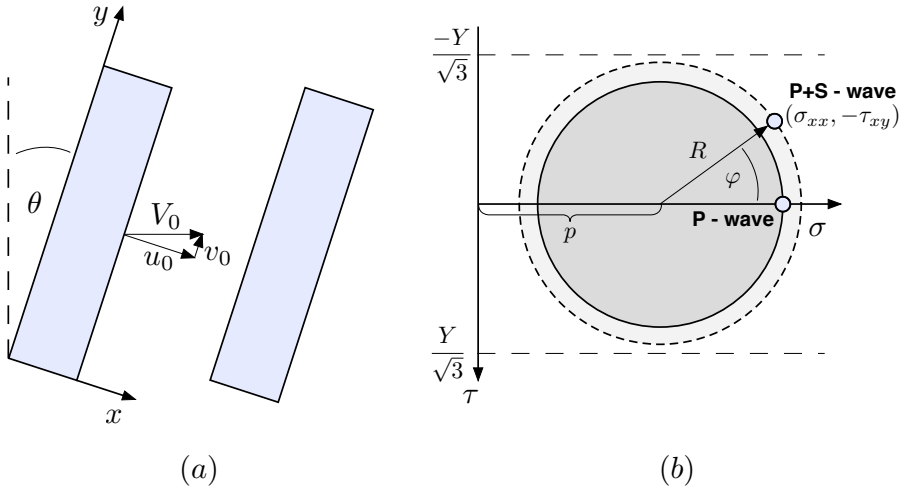

Figure 7.1: (a) Schematic of symmetric PSPI configuration. (b) Mohr circle representation of the combined state of stress within the elastic regime ($R < Y/\sqrt{3}$) during PSPI experiments.

When a material is loaded beyond its elastic regime, the combined state of stress changes to accommodate the restrictions imposed by the yield surface. Assuming a von Mises yield criterion

$$Y = \sqrt{\frac{3}{2}s_{ij}s_{ij}}, \tag{7.7}$$

where s_{ij} is the deviatoric stress tensor, the yield condition takes on the form

$$\frac{3}{4}s_{xx}^2 + \tau_{xy}^2 = \frac{1}{3}Y^2. \tag{7.8}$$

Equation 7.8 illustrates the coupling between longitudinal and shear stresses through the yield strength of the material. The longitudinal deviatoric stress s_{xx} vanishes, when a shear wave of sufficient amplitude ($\tau_{xy} = Y/\sqrt{3}$) is propagating within a yielding material. Hence, the shear stress provides a direct measure of the yield strength of materials even if the applied normal stress exceeds the elastic limit. If the shear stress is supported by an interface with an elastic anvil, the material strength can be directly inferred from velocity measurements on the free surface of that anvil, according to Eq. 1.4. However, shear waves propagating through yielding anvils will spread and are therefore not directly representative of the sample's shearing response.

Abou-Sayed and Clifton analyzed the propagation of combined normal and shear waves in rate-dependent materials using a second-order-accurate finite-difference scheme [81]. Figure 7.2 (a) illustrates the spreading of shear waves propagating through yielding material regions. Due to the coupling of normal and shear stresses, as defined by Eq. 7.8, the shear wave is also called a quasi-transverse wave as it exhibits both normal and transverse velocity components [82], which is highlighted in Fig. 7.2 (b).

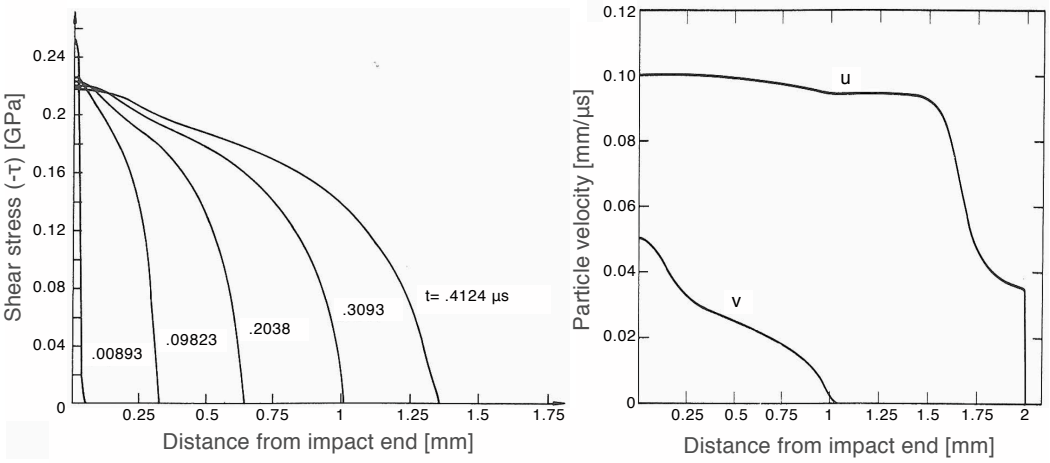

Figure 7.2: (a) Spreading of shear waves as a function of propagation distance in yielding anvils [81]. (b) Computed normal and transverse velocity profiles for combined pressure and shear loading in inelastically deforming anvils [81].

Strength Determination for Yielding Anvils

The spreading of shear waves in inelastic materials poses a strict limitation on successful PSPI experiments at pressures exceeding the elastic limit of the employed anvil plates. This constraint is illustrated by numerical simulations in which a step normal stress (σ_0 = 15 GPa) and varying degrees of shear loading $\tau_0 = Y_s/\sqrt{3}$, representing the sample strength, are applied to the front surface of a 50 mm diameter and 12 mm thick tungsten carbide specimen. A hypothetical elastic-perfectly plastic strength model and elastic properties of tungsten carbide were selected for the anvil material (ρ = 15600 kg/m^3, E = 609.1 GPa, ν = 0.2, Y_a = 5 GPa).

Figure 7.3 (a) displays the spreading of shear waves of different amplitude obtained after propagating through 4 mm of the yielding anvil material for sample strengths between 2 and 5 GPa. The initial shear step load spreads considerably, effectively limiting the observation time and maximum shear strain for which the sample's shear response can be measured. The shear stress rise time strongly depends on the ratio of the sample to anvil strength, which is depicted in Fig. 7.3 (b). Given the limited shear window in PSPI experiments, as shown in Fig. 1.6, the shear wave spreading in yielding anvils imposes a fundamental limitation on the strength of materials that can be studied given a certain anvil strength. The choice of the sample to anvil strength ratio has to be even more conservative if PSPI experiments hope to reveal material behavior beyond the sample's initial yield strength, such as strain hardening or damage processes. Considering a shear window of 1 μs, as observed for the PSPI experiments reported here, a sample to anvil strength ratio above 75% would likely not capture any strength related information given the previously specified assumptions of anvil behavior.

The spreading of shear waves also invalidates the strain calculation based on Eqs. 1.5 and 1.6 for inelastic anvil plates. Furthermore, shear wave attenuation associated with anvil plasticity and damage processes will affect the normal and shear stress calculation using Eqs. 1.3 and 1.4.

Forward methods that aim to match the obtained free surface velocity measurements through numerical modeling or inverse methods [83, 84] inferring the sample's response at the anvil interfaces are required to obtain realistic shear strain and stress measurements. However, even these more advanced analysis techniques rely on the velocimetry results on the rear anvil's free surface and are not able to circumvent excessive shear wave spreading.

As both shear wave spreading and attenuation have a strong influence on the actual

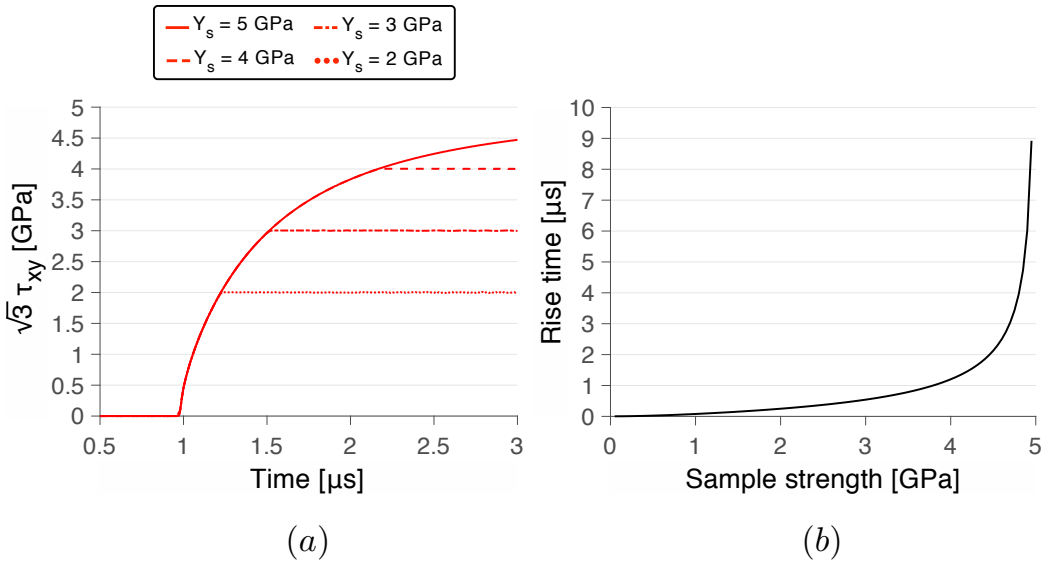

Figure 7.3: (a) Shear stress wave spreading after propagating 4 mm through yielding tungsten carbide anvils. (b) Rise time of shear stress as a function of sample strength for elastic-perfectly plastic anvils (Y_a = 5 GPa).

measurements of the sample material, a thorough characterization of the inelastic behavior of the anvil plate material has to be conducted. Section 6.2 details the investigation of the tungsten carbide anvil plates employed in this work.

7.2 Finite Element Modeling of Dynamic Experiments

The finite element method is employed to model the macroscopic material behavior of both the tungsten carbide anvils and the soda-lime glass samples in PSPI experiments. As plate impact experiments are well-known for their large stress and velocity gradients, the domain discretization becomes crucial to accurately represent the dynamic material behavior. The finite element solver LS-Dyna (Version R9.0.1) [85] was employed with an explicit time integration to obtain the presented simulation results. Constant-stress 3-dimensional solid elements with a Flanagan-Belytschko hourglass stabilization scheme were utilized in the simulations.

Figure 7.4 compares the simulated normal wave profiles for different mesh sizes. A mesh size ratio of 1:10 between the shocked and transverse directions was maintained during the comparison in an effort to avoid numerical artifacts. For the materials and experimental conditions studied here, the highest velocity gradients occur in the initial rise of the compressive wave's elastic precursor. The rise time and HEL are well represented by a simulation employing a mesh size of 10 μm in the shocked direction, which is being used for the simulations reported here.

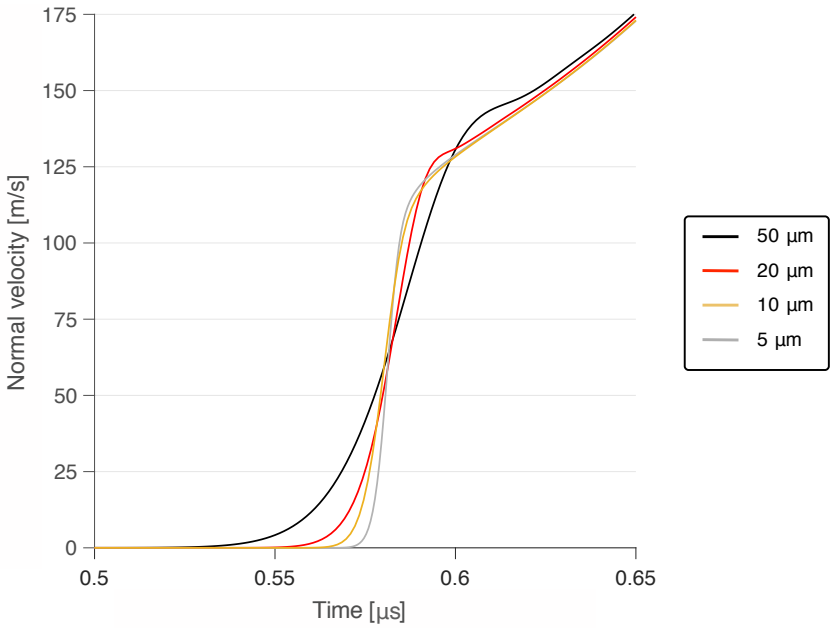

Figure 7.4: Comparison of simulated normal velocity profiles with corresponding element sizes in the shocked direction.

The computational cost of the simulations is reduced by replacing the elements in the non-shearing, lateral direction with zero-displacement boundary conditions on the lateral surfaces. This is equivalent to simulating the entire domain due to the uniaxial compression and simple shear deformation experienced in PSPI experiments. The impact surface nodes on the flyer, target and sample surfaces are merged to circumvent contact noise and associated challenges.

7.3 Constitutive Relations

The results from symmetric PSPI experiments on tungsten carbide, discussed in Section 6.2, motivate the inclusion of hardening and damage effects into the constitutive relations. Quasi-static experimental results on different tungsten carbide materials identified a remarkable strain hardening of similar magnitude as the initial yield strength [86]. The strain hardening function employed for this work follows a Johnson-Cook strain hardening model [87]

$$Y(\varepsilon) = Y_0 + B\varepsilon^n, \tag{7.9}$$

where Y_0 represents the initial yield strength of the material, B is the coefficient and n the power of work hardening.

As reviewed in Section 5.1, many materials exhibit strain rate-dependent material

behavior, which for tungsten carbide is modeled through a Cowper-Symonds law of the form

$$Y = Y(\varepsilon)\left(1 + \left(\frac{\dot{\varepsilon}^{pl}_{eff}}{C\dot{\varepsilon}^{pl}_{ref}}\right)^{1/p}\right), \tag{7.10}$$

where C is the coefficient and p the power of rate hardening and $\dot{\varepsilon}^{pl}_{eff}$ and $\dot{\varepsilon}^{pl}_{ref}$ constitute the effective and reference plastic strain rate, respectively. Swegle and Grady [88] observed that the strain rate in shock experiments followed the very simple relation $\dot{\varepsilon} = A(\Delta\sigma)^4$ for different material systems. This phenomenological relation is applied to the Cowper-Symonds law by setting the strain rate hardening power to $p = 2$.

As materials experience large volumetric deformations, the pressure-volume relation becomes non-linear, which is modeled by a simplified Gruneisen equation of state [89]

$$p = \frac{\rho_0 c_0^2 \mu[1 + (1 - \gamma_0/2)\mu]}{(1 - (S_1 - 1)\mu)^2}, \tag{7.11}$$

with the relative change in density $\mu = \rho/\rho_0 - 1$, the bulk wave speed c_0, the unitless Gruneisen parameter γ_0 and first order coefficient of the shock velocity-particle velocity relation S_1. A more general form of the equation of state is often formulated by a polynomial function

$$p = K\mu + K_2\mu^2 + K_3\mu^3, \tag{7.12}$$

with the bulk modulus $K = \rho c_0^2$ and higher order coefficients K_2 and K_3.

7.4 Calibration of Tungsten Carbide Material Model

As previously mentioned, the accurate characterization of tungsten carbide anvils is critical for the inference of sample behavior in PSPI experiments. The material properties of tungsten carbide, shown in table 7.1, were obtained from density measurements, energy-dispersive x-ray spectroscopy (EDS) and reported values [26, 28].

Table 7.2 shows the parameters for the Johnson-Cook strain hardening model and the Cowper-Symonds strain rate hardening law, which were established through

ρ [kg/m^3]	G [GPa]	K [GPa]	ν [-]	c_1 [m/s]	c_2 [m/s]	Co-wt%
15600	273	379	0.21	6900	4180	3

Table 7.1: Material properties of tungsten carbide.

the comparison of simulation results with experimental wave profiles, while the coefficients for the Gruneisen equation of state are taken from literature [28].

Y_0 [GPa]	B [GPa]	n [-]	C [-]	$\dot{\varepsilon}^{pl}_{ref}$ [1/s]	p [-]	c_0 [m/s]	γ_0 [-]	S_1 [-]
3.2	11	0.25	500	10^6	2	4930	1.62	1.309

Table 7.2: Hardening and equation of state parameters for tungsten carbide.

Figure 7.5 compares the experimentally obtained and simulated normal and transverse free surface velocity measurements during experiment CK-1806. The simulated normal velocity profile reproduces the HEL and evolution of the plastic wave. Analysis of particle velocities inside the target plate showed that the double peak structure observed at 0.8 μs and 1 μs is caused by free surface effects which arise from the long rise time of the shock profile. The simulation underestimates the peak velocity observed in the experiment by approximately 4%.

Following a steep initial rise (<30 m/s), the simulated transverse velocity follows a similar shear wave spreading. Above a transverse velocity of 60 m/s, the simulated response overpredicts the final velocity. Furthermore, the smooth evolution to a constant final velocity does not fully capture the more oscillatory and upward sloping final response observed in the experiments.

As discussed in Chapter 6, the normal response of the target assembly is unaffected by the presence of a 5 μm thick soda-lime glass sample. Figure 7.6 shows a comparison of normal velocities obtained from symmetric PSPI experiments on tungsten carbide and sandwiched glass samples with numerical results. As noted during the comparison for experiment CK-1806, the elastic precursor is matched accurately, while the final peak value is underestimated by 3-4%. The higher discrepancy observed for the simulation result of experiment TJ-1802 (7%), could have been caused by an inaccurate impact velocity measurement. The elevated strain rates experienced in experiments CK-1803, CK-1701 and CK-1801 result in a steeper ramp-up of the plastic wave than is observed experimentally, which highlights the limitation of the plasticity-based modeling approach for the description of brittle material behavior at high pressures.

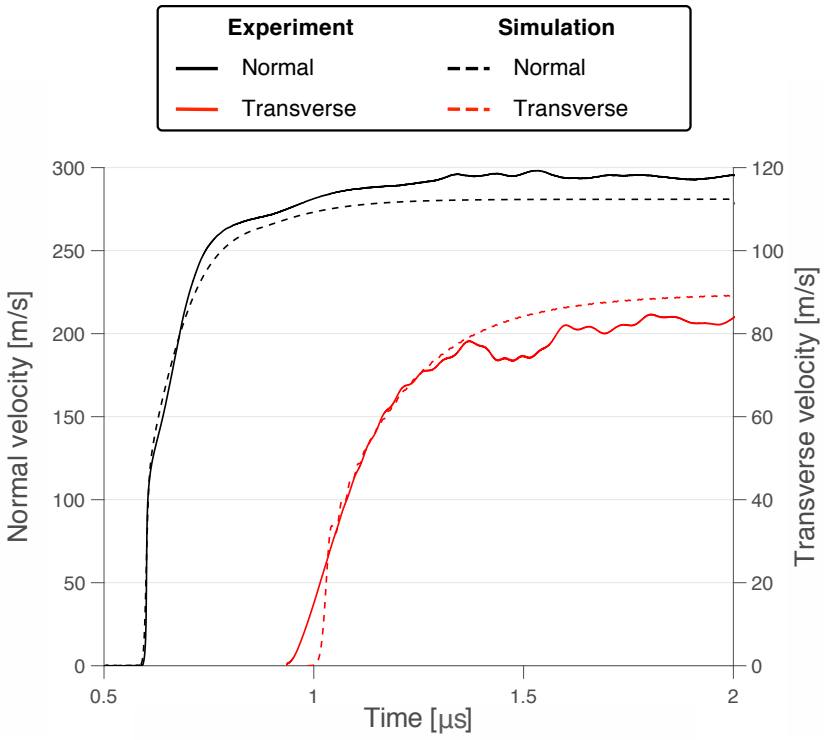

Figure 7.5: Normal and transverse velocity profiles obtained from velocimetry measurements and numerical simulation of PSPI experiment CK-1806.

7.5 Strength Extraction from Soda-Lime Glass Experiments

The material properties of soda-lime glass, obtained from reported values [50], are shown in Table 7.3. A polynomial equation of state with only the linear term of Eq. 7.12, i.e. the bulk modulus K, is utilized for modeling the pressure-volume response of soda-lime glass.

ρ [kg/m^3]	G [GPa]	K [GPa]	ν [-]	c_1 [m/s]	c_2 [m/s]
2530	30.5	45.3	0.225	5830	3470

Table 7.3: Material properties of soda-lime glass.

The utilized strength model follows similar considerations as the Johnson-Holmquist 2 (JH-2) model for brittle materials [90], which transitions the material strength from an intact to a failed state. The strength evolution of a JH-2 model is defined through pressure-dependent characteristic strains, which is consistent with the current and previous [24] pressure-shear plate impact experimental results on soda-lime glass. Figure 7.7 depicts the employed pressure-dependent softening model, with an intact strength of 2.8 GPa for all strain values below the onset of softening at ε_o. An

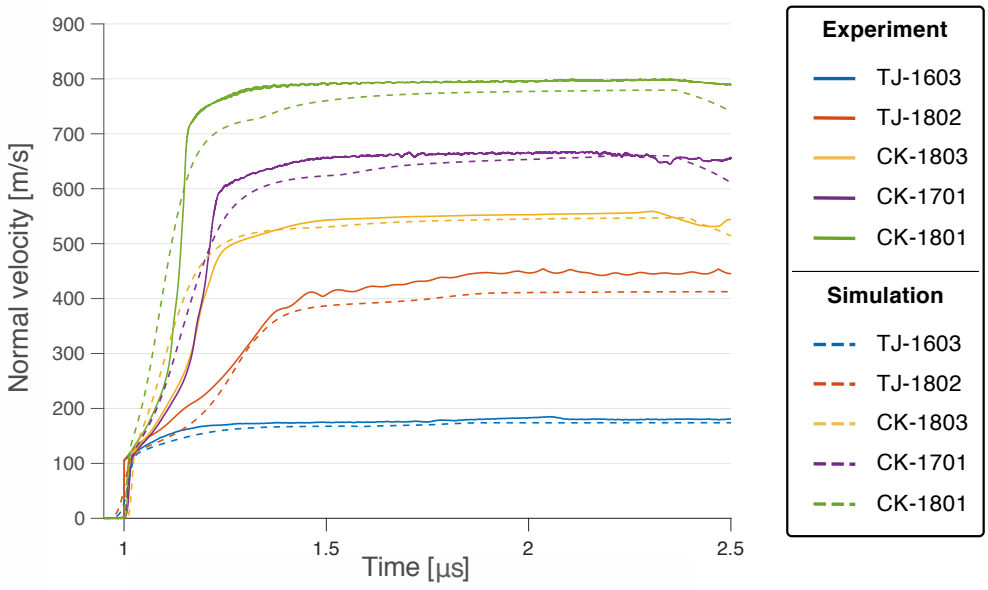

Figure 7.6: Comparison of simulated and measured normal velocities during PSPI experiments at different impact velocities.

intermediate damaged strength σ_d and strain ε_d specify the immediate precipitous strength loss before a granular, failed strength σ_f is defined at large plastic strain ε_f.

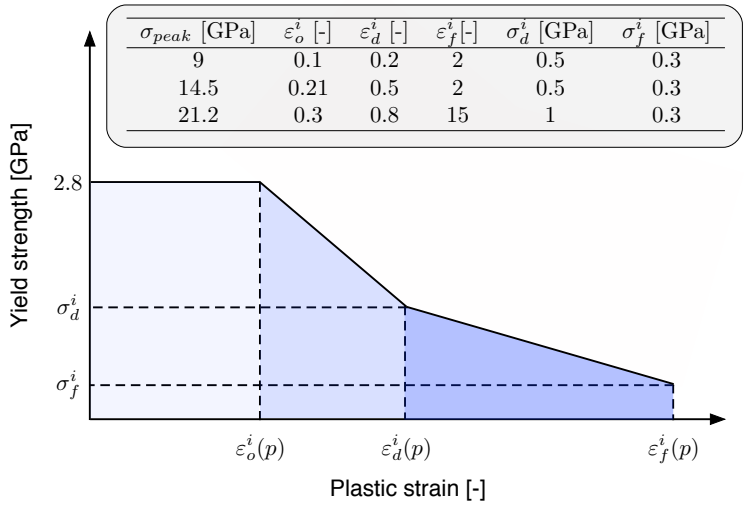

Figure 7.7: Pressure-dependent strain softening model for soda-lime glass.

Figure 7.8 (a) compares the simulated and measured normal and transverse velocities

during experiment TJ-1603. Both velocity profiles are well represented by the utilized model, described in Fig. 7.7. The effect of shear loading on the normal velocity profile is highlighted by the comparison to a corresponding normal impact simulation, represented by a blue dotted line, which highlights the effect of normal and shear stress coupling in yielding anvil materials. The increase in normal velocity at approximately 2μs is further investigated by correlating the simulated normal and transverse velocities at the sample-rear anvil interface, depicted in Fig. 7.8 (b). The increase in normal velocity clearly coincides with the arrival of the shear wave, highlighting the experimental observation of normal and shear stress coupling.

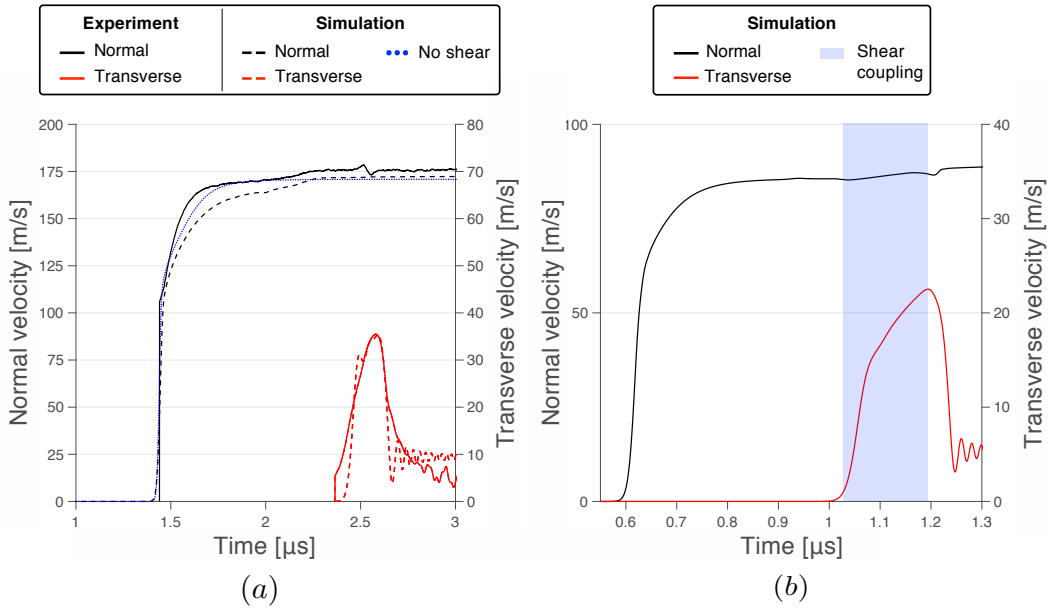

Figure 7.8: (a) Comparison of measured and simulated normal and transverse velocities of experiment TJ-1603. (b) Simulated velocity gauge at sample-rear anvil interface highlighting normal and shear stress coupling in yielding anvils.

The comparison between the numerical predictions and experimental results for experiment TJ-1802 is depicted in Fig. 7.9. As previously discussed, the uncharacteristically large discrepancy between the experimentally measured and numerically obtained normal velocity profile in experiment TJ-1802 (7%), constitutes an outlier. The pressure-dependent strain softening model of soda-lime glass accurately predicts the peak and release observed in the experimental transverse velocity record, but exhibits a much shorter rise time.

Figure 7.10 depicts a direct comparison between the experimentally observed and numerically predicted normal and transverse velocities during PSPI experiments

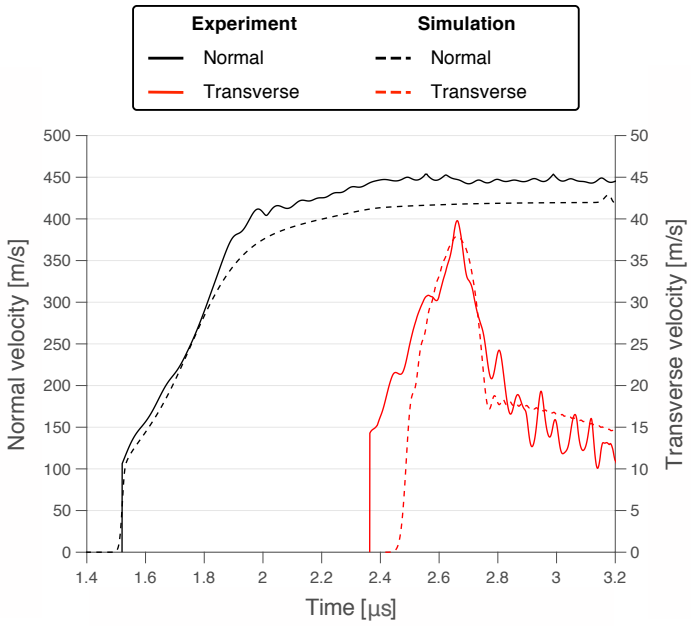

Figure 7.9: Normal and transverse velocity profiles obtained from velocimetry measurements and numerical simulation of PSPI experiment TJ-1802.

CK-1805, CK-1807, and CK-1808. The numerical model does not predict the dip in normal velocity following the initial compression wave but reproduces the effect of the soda-lime glass layer on the evolution of the normal velocity profile. In fact, the normal velocity profiles compare more favorably with increasing sample thickness. As expected from the Lagrange diagram depicted in Fig. 4.5, all experiments show clear signs of a recompression wave in their normal velocity profiles at approximately 2 μs. These wave signatures carry information regarding the failed state of the soda-lime glass sample layer and the strength of the tungsten carbide anvils after both shock and shear waves have propagated through the target assembly. Although the recompression waves are predicted to arrive slightly earlier than observed experimentally, the waveforms show remarkable similarity.

The simulated response of experiment CK-1808 matches the measured transverse velocity profile exceedingly well. However, the numerical model overestimates the peak shearing response in experiment CK-1805, which is predicted to ramp up with a much shorter rise time. Although the initial shear stress reverberations are not fully captured by the simulated transverse velocity of experiment CK-1807, the measured and predicted slope of the transverse velocities are comparable. The model does not predict the observed shearing resistance plateau at a transverse velocity of 39 m/s, which supports the hypothesis that interface slip occurred during the experiment.

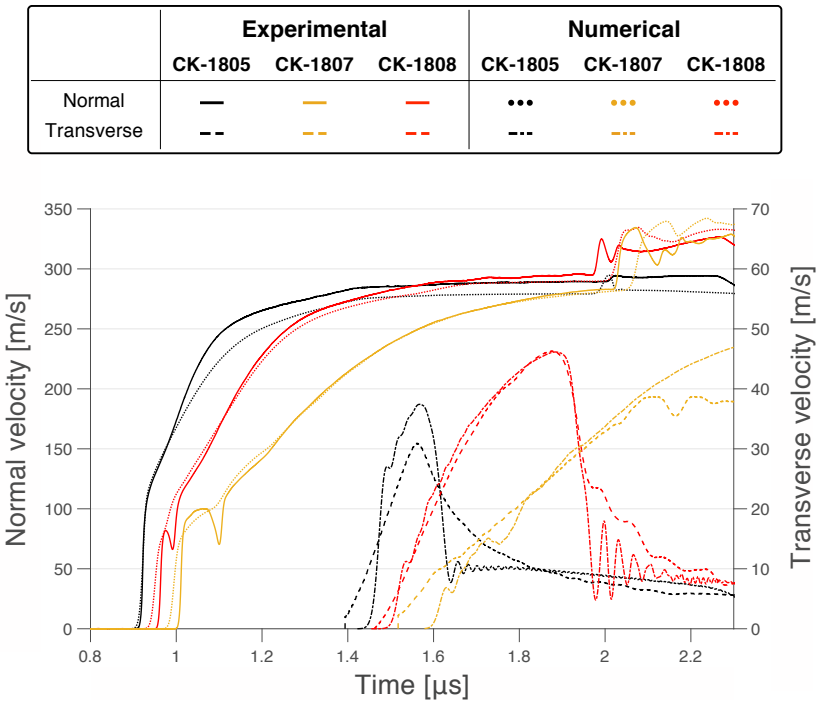

Figure 7.10: Normal and transverse velocity profiles obtained from velocimetry measurements and numerical simulation of soda-lime glass PSPI experiments CK-1805, CK-1807 and CK-1808.

Nevertheless, the slope of the transverse velocity profile carries strength information, which reveals a more detailed view of the onset of inelastic deformation.

7.6 Temperature Rise in Soda-Lime Glass Layer

Figure 7.7 highlights the extensive inelastic deformation accommodated by the thin soda-lime glass layers prior to softening in PSPI experiments. A significant fraction of the associated strain energy is converted to heat, which leads to a temperature increase in the sample material. Considerable heating can result in thermal softening, which for soda-lime glass occurs in the proximity of its glass transition temperature of approximately 570 °C [91].

The strength model described in section 7.5 is implemented in a coupled thermo-mechanical finite element model to calculate the temperature rise inside the soda-lime glass layer during the PSPI experiments conducted in this work. A constant specific heat capacity of c_p = 900 J/kg·K [92], a conductivity of k = 1.06 W/m·K [92] and an inelastic heat fraction of 0.9 were chosen as the thermal material parameters. This continuum analysis assumes uniform heating of the glass layer without strain localization and the formation of “hot spots”. As described in Section 1.3,

PSPI experiments gradually ramp up the stresses inside the sample material through reverberations, which gives rise to a quasi-isentropic compression process [26]. Therefore no shock heating is considered for this analysis.

Figure 7.11 shows the temperature rise up to the pressure-dependent softening strain $\varepsilon_o^i(p)$ computed by the coupled finite element solver. The assumption of uniform deformation of the soda-lime glass layer likely becomes invalid after softening occurs.

A maximum temperature increase of 350 K is observed in the highest pressure experiment, i.e. TJ-1802. With an initial sample temperature of 20 °C, the results suggest that the temperature rise is modest enough, compared to the glass transition temperature of soda-lime glass, to not significantly affect the material behavior during the conducted PSPI experiments.

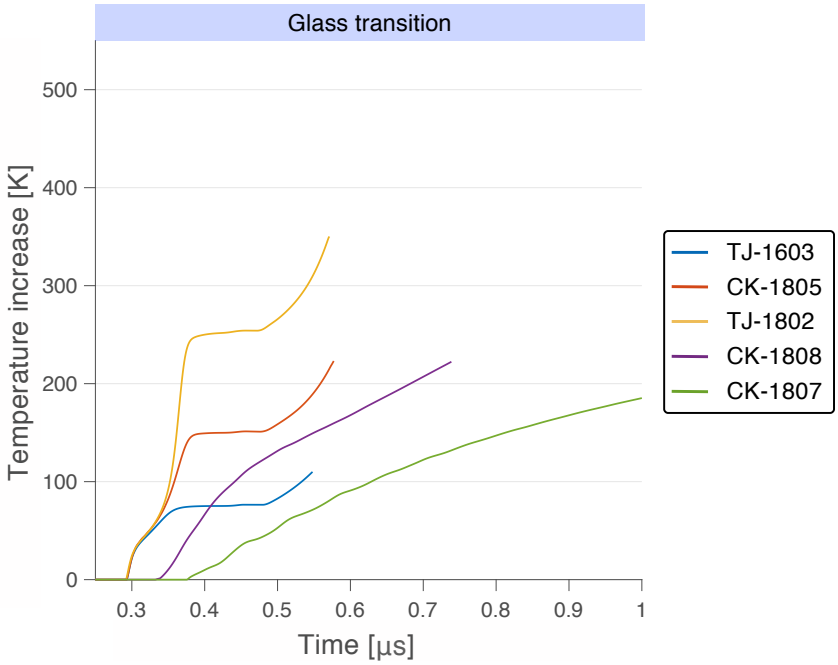

Figure 7.11: Temperature rise estimate within the soda-lime glass layer during PSPI experiments computed by coupled thermo-mechanical finite element solver.

Chapter 8

DISCUSSION

The following chapter examines the experimental observations, detailed in Chapter 6 while considering insights into the deformation and failure mechanisms provided by the numerical model in Chapter 7.

8.1 Dynamic Material Behavior of Tungsten Carbide

Tungsten carbide is considered one of the most "ductile" ceramics [93], with a spall strength in close proximity to its HEL, as predicted by a von Mises yield criterion for ductile materials [94]. Furthermore, ceramics are hypothesized to exhibit a brittle to ductile transition in the mechanism for accommodating inelastic deformation, which was attributed to an increase in confining pressure during uniaxial strain conditions. Therefore, it is reasonable to assume that a modeling approach based on plasticity mechanisms could succeed in the prediction of material behavior observed in pressure-shear plate impact (PSPI) experiments on tungsten carbide.

Comparison between the velocity profiles observed during experiment CK-1806 and the predictions made by modeling inelastic deformation using a plasticity approach, depicted in Fig. 7.5, shows an adequate agreement. This suggests that the constitutive law, detailed in Section 7.4, provides an equivalent description of the quasi-plastic material behavior observed at normal stresses of up to 14 GPa. High strength and work hardening even at larger shear strains, visible through the sloped trend of the transverse velocity profile, enables the use of tungsten carbide as an anvil material in this normal stress range.

However, subtle aspects hint at the limitations of modeling tungsten carbide as a ductile material at "modest" pressures. The normal velocity profiles of each experiment are slightly below predicted values, typically by 3-4%, while the final transverse velocity of experiment CK-1806 is overestimated. A higher strength would reduce the normal velocity discrepancy at the cost of an increased gap in the transverse profiles. The introduction of a strain rate hardening law is required to minimize these contrasting trends and to "smooth" out the otherwise sharp waveforms in the simulated normal velocity profiles. However, the added strain rate dependence leads to an aberrant ramp up in the simulated transverse velocity record, which occurs

on a shorter time scale than observed during the experiments. It is noteworthy that these observations would have been impossible to arrive at without the additional information from the transverse velocity signal provided by the PSPI experimental technique. This point is highlighted by the remarkably good agreement of the measured normal velocities at normal stresses of up to 37 GPa with the simulated responses based on a material model designed for ductile materials, which is due to the similar imprint of strain hardening in ductile and pressure hardening in brittle materials on the normal velocity profiles.

The erratic nature of the measured normal and transverse velocity signals after the passage of the compressive and shear waves could hint at the onset of damage in tungsten carbide, which is not captured by the employed plasticity-based constitutive laws. At a normal stress of 26.5 GPa, a transition to a low shearing resistance regime is observed in symmetric PSPI experiment CK-1804. Two PSPI experiments on soda-lime glass at stresses just below, 25.8 GPa in experiment CK-1803, and above experiment CK-1804, in experiment CK-1802 at 27.2 GPa, observed a direct correlation between the normal stress the tungsten carbide anvils were subjected to and their measured shearing resistance, which is depicted in Fig. 6.4. This suggests that the shearing resistance in experiments CK-1802 and CK-1803 is not governed by the 5 μm thick soda-lime glass layer, but by the employed tungsten carbide anvils. Based on the partial strength recovery observed between PSPI experiments at normal stresses of 26.5 and 25.8 GPa, a significant strength can be assumed to exist at a normal stress of 21.2 GPa experienced in experiment TJ-1802.

A similar loss of strength was observed in symmetric PSPI experiments on pure tungsten carbide anvils, which discounts mechanisms associated with the cobalt binder as the source for the softening in uniaxial compression. Experiment CK-1902, designed with the same transverse impact velocity component as measured in the "high-strength" experiment TJ-0103, revealed that the higher shear loading is only partially responsible for the reduced transverse velocity measurements. Therefore, the loss of shearing resistance mainly occurs due to softening or damage mechanisms which are active during the inelastic deformation associated with the compressive, uniaxial strain loading. The higher plateau of Experiment CK-1902 indicates that the ratio of shear to normal stress does have an effect on the measured shearing resistance. Further experiments could illuminate if this behavior persists at higher pressures or if it is confined to a transitional pressure range between the high and low shearing resistance regime.

8.2 Dynamic Material Behavior of Soda-Lime Glass

The pressure-dependent strain softening model accurately predicts the response of soda-lime glass over a large range of normal stresses, between 9.0 and 21.2 GPa. The simulated peak transverse velocities are in excellent agreement with the measured values in PSPI experiments TJ-1603 and TJ-1802. The initial ramp-up of the transverse velocity in PSPI experiment TJ-1802 constitutes the largest discrepancy between the simulated and measured response. Due to the small thickness of the vapor-deposited soda-lime glass layer, the rise time is mostly governed by the spreading of the shear wave during its propagation through the inelastically deforming tungsten carbide. This could be an indication, along with the erratic waveforms observed during the rise and precipitous reduction in transverse velocity, of the onset of damage in the tungsten carbide anvils at a normal stress of 21.2 GPa.

The computed normal velocities of PSPI experiments CK-1805, CK-1807, and CK-1808, depicted in Fig. 7.10, show an improved prediction of the structure and evolution of the measured normal velocity profiles with increasing sample thickness. However, the significant precursor decay observed between the initial compression wave and the first reverberation inside the 100 and 300 μm thick glass samples at pressures of 4.4 and 5.4 GPa, respectively, is not captured by the soda-lime glass material model. Substantial elastic precursor decay has been observed in symmetric normal impact experiments on x-cut crystalline silica (quartz) at slightly higher pressures of 9 GPa [95], which was associated with unsteady time-dependent wave profiles in samples with small propagation distances [37]. The well-known unsteady wave behavior for short propagation distances could explain the wave profiles obtained with the 100-300 μm thick soda-lime glass samples. However, the proximity of the attained normal stresses to the "failure wave" phenomena [47, 49] in soda-lime glass motivates further investigation of this anomalous waveform.

The comparison of the numerical results and measured transverse velocities, obtained at almost identical normal stresses (14.1-14.5 GPa) and strain rates across two orders of magnitude ($3{\cdot}10^5$-$1.2{\cdot}10^7 s^{-1}$), demonstrates the strain rate independent material behavior of soda-lime glass. The discrepancy of the computed and measured peak transverse velocity in experiment CK-1805 is attributed to the simulated ramp up, which occurs on a much shorter timescale than observed during the experiment. This results in a lower accumulated strain during the simulated ramp up and softening of the material will occur at a higher shearing resistance. The discrepancy is exacerbated by the extreme shear strain rates in this experiment

($1.2{\cdot}10^7 s^{-1}$). Despite a more significant imprint of the shear wave reverberations on the simulated transverse velocity profile, the discrepancy between the simulated and measured material response improves with increasing sample thickness as the ramp up and overall response is more strongly affected by the glass layer.

The pressure-dependent softening law, employed for modeling the behavior of soda-lime glass, transitions its strength from an intact to a failed state at characteristic, pressure-dependent plastic strains, following similar descriptions of material strength in soda-lime glass [96]. The numerically implemented failed strength value of 300 MPa, based on the measurement of a granular strength of silica sand [17], matches the observed transverse velocity profiles in the corresponding PSPI experiments. This indicates that the softening behavior describes a transition from a quasi-plastic material behavior under combined pressure-shear loading below strains of 10% (9.0 GPa), 21% (14.5 GPa) and 30% (21.2 GPa) to a granular flow regime at strains exceeding 200%. In agreement with molecular dynamics simulations on silica glass [44], the damage initiation is shown to occur much earlier than previously reported at 200% [24]. Nevertheless, a strain-dependent failure mechanism, as reported for earlier PSPI experiments at 3.5 and 5.7 GPa [24], was observed to persist throughout the normal stress range explored in this study (9.0-21.2 GPa). Strength measurements of soda-lime glass obtained from release wave experiments [29] showed a strong dependence of strength on the normal stress level attained during the experiments. This observation is in stark contrast to the measurements reported in this work while the intact strength value of 2.8 GPa falls within the range of reported strength values, depicted in Fig. 1.1. The limited strength sensitivity of the release wave technique combined with its inherent inability to resolve strain dependent phenomena, prevalent in damage and failure modeling approaches for brittle materials [90], is the likely cause for the differing conclusions.

As a 5 μm thick soda-lime glass layer manufactured from bulk material could not be manufactured, the open question at the start of this work remained if the response of the vapor-deposited thin film is representative of the bulk material behavior of soda-lime glass. The comparison of all experimental results with simulations based on one unified material description suggests that the material response is remarkably similar within the context of combined pressure-shear loading, demonstrating the validity of comparisons between materials from different manufacturing techniques. The lack of a mesoscopic length scale and microstructure in amorphous materials is likely responsible for the observed similarity in material behavior.

Chapter 9

CONCLUSIONS AND FUTURE WORK

9.1 Summary

The main focus of this work lies in the determination of the material strength of silica glasses at high pressures and strain rates. The pressure-shear plate impact (PSPI) experiment constitutes the ideal technique for probing material strength under these conditions, due to their well-characterized plane wave loading and the invaluable information provided by the shearing response of the material of interest. The range of accessible pressures and strain rates was greatly improved by the development of the high-pressure PSPI (HP-PSPI) technique (Chapter 4), which leverages the increased terminal projectile velocities of powder gun setups while addressing associated challenges such as the effects of the high-pressure loading on the sabot assembly, i.e. increased impact tilt and sabot failure, stronger vibration environment and higher temperatures experienced by the diffraction grating during a more severe shock loading.

The development of a fiber-optic heterodyne transverse velocimetry (HTV) diagnostic (Chapter 5) greatly improved the fidelity of the transverse velocity measurement during PSPI experiments, thereby enabling a more detailed analysis of material behavior. The heterodyne nature of the diagnostic enables the application of robust frequency-based data reduction techniques which are less affected by fringe amplitude variations and signal noise while also enabling the automatic detection of velocity reversals. The thorough design of the fiber-optic system and diffraction grating minimize error-inducing light coupling losses, caused by impact tilt and normal displacement of the rear target plate, and guarantee high-intensity velocimetry signals throughout the experiments. The challenging transverse velocity rise times and velocity reversals during the validation experiments on Y-cut quartz demonstrated the efficacy of the developed diagnostic.

The very high acoustic impedance of tungsten carbide motivated a rigorous study of its applicability towards their use as anvil materials for HP-PSPI experiments. Symmetric PSPI experiments (Chapter 6) at different pressure levels established a range of normal stresses above the elastic limit where tungsten carbide retains most of its strength and can be successfully used as an anvil material. Uniaxial

shock compression above normal stresses of 25 GPa is shown to strongly reduce the shearing resistance of tungsten carbide, limiting its use as an anvil material under these conditions. The reduction in shearing resistance is attributed to softening or damage mechanisms occurring during the inelastic deformation associated with the passage of the pressure wave. The underlying mechanisms for the loss of strength under uniaxial compressive loading require further examination. Nevertheless, successful experiments were conducted at normal stresses of 15 GPa, highlighting the applicability of tungsten carbide as an anvil material during PSPI experiments exceeding its HEL while remaining below normal stresses of ~25 GPa.

PSPI experiments on soda-lime glass suggest that its intact strength of 2.8 GPa is insensitive to pressure and strain rate, while the transition towards a failed, granular state is pressure-dependent (Chapter 7). A pressure-dependent strain softening is observed which transitions from the intact soda-lime glass strength at strains of 10% (9.0 GPa), 21% (14.5 GPa) and 30% (21.2 GPa) and reaches a failed, granular strength of 300 MPa following large inelastic deformation ($\varepsilon_f > 200\%$). The transition from an intact to a failed strength is reminiscent of earlier works on soda-lime glass [18, 49] and well-known constitutive laws such as the Johnson-Holmquist 2 (JH-2) model [90]. Conducting experiments with different sample thicknesses isolated the effect of strain and strain rate on the sample strength, while the normal stress remained constant across experiments. The validity of comparisons among the vapor deposited (5 μm) and bulk samples (100/300 μm) was demonstrated by the ability to accurately predict the compressive and shearing response of both materials with the same constitutive model.

An effort has been made to establish numerical simulations capable of accurately modeling critical aspects of material behavior during PSPI experiments (Chapter 7). A fundamental change in the way that PSPI experiments are analyzed was imperative given the inelastic deformation exhibited by the anvil plates at higher pressures and the corresponding shear wave spreading and attenuation. In addition to relying on the method of characteristics to obtain stress, strain rate and strain profiles at the sample interface, a constitutive law that predicts both the measured normal and transverse velocities in anvil materials at high pressures has to be established in order to characterize accurate material behavior. Although this approach is challenging, obtaining a full description of the governing material laws is extremely valuable beyond the measurement of shearing resistance. This holistic approach can take full advantage of the wealth of information provided by both the normal and

transverse velocity profiles obtained during PSPI experiments and provides a much more detailed view of the physics behind the observed wave profiles.

9.2 Future Work

Investigation of Precursor Decay

Figure 7.10 shows a significant precursor decay between the initial compression wave and the first reverberation inside the sample material in PSPI experiments CK-1807 and CK-1808. Currently, this behavior is not captured by the employed soda-lime glass constitutive model which motivates further investigation. PSPI experiments at different stress levels could shed light on the potential connection between the "failure wave" phenomenon and precursor decay in soda-lime glass. If "failure waves" constitute the primary mechanism for the observed precursor decay, PSPI experiments with an initial compression wave at normal stresses below the HEL of soda-lime glass or above 10 GPa should not exhibit this behavior.

Phase Transformations in Soda-Lime Glass

As discussed in Section 2.2, the phase transformation from amorphous silica glass to a crystalline high-pressure polymorph called stishovite has been observed using x-ray diffraction diagnostics at synchrotron [2] and x-ray free-electron laser facilities [6, 39]. Similar studies on soda-lime glass could illuminate to which extent compositional changes affect the kinetics and atomistic rearrangements of phase transformations. *In-situ* diffraction studies could reveal the formation of new and distinct phases forming at different pressure levels, which would have significant implications for modeling the behavior of soda-lime glass at high pressures.

Experimental

As the main objective of the HP-PSPI experiments is to extend the range of pressures at which material behavior can be observed, future work should focus on investigations to identify anvil materials that retain their strength above 20 GPa. Within the context of this work, PSPI experiments at pressures of 40 GPa could reveal the evolution of dynamic strength across the observed phase transformation to a higher-density crystalline phase in silica glass.

As the goal of achieving higher normal stresses favors materials with a high acoustic impedance, further study of tungsten carbide should be conducted to establish the upper-stress limit for different compositions, i.e. cobalt content, and grain size. Cemented tungsten carbide compounds with high cobalt content exhibit much-

increased failure strains [86], which could enable the characterization of materials at higher pressures, albeit with more inelastic deformation due to their reduced compressive strength. Extending the concept of accepting ductile anvil behavior, steel and tantalum anvils could be utilized assuming they retain most of their strength at high pressures. The relatively low strength of these materials, however, limits the range of materials that can be tested due to the spreading of shear waves in yielding anvils. Additionally, their lower impedance will require higher impact velocities, in comparison to tungsten carbide anvils, to achieve the desired normal stress.

As seen in Table 4.1, the HEL of sapphire can attain values of up to 22 GPa, which should enable the straightforward PSPI analysis for elastic anvils up to high normal stresses. Due to its pressure-insensitive refractive index and transparency to infrared light, *c*-cut sapphire also constitutes an ideal window material for the velocimetry diagnostics developed here and could enable normal and transverse velocity measurements directly at the sample-rear anvil interface [97]. Additionally, the higher refractive index of sapphire enables the utilization of finer diffraction gratings, which could provide a higher velocity resolution for the HTV diagnostic [62]. The observed scatter in sapphire's HEL [19] and unsteady waveforms during inelastic deformation could lead to additional difficulties in high-pressure PSPI experiments. Moreover, the lower impedance will lead to a more challenging experiment compared to tungsten carbide anvils at the same pressure level.

Simulation

The finite element simulations (Chapter 7) have hitherto relied on hardening and softening mechanisms that typically describe plastically deforming materials. However, the material models of both the tungsten carbide anvils and the soda-lime glass samples could benefit from constitutive relations specifically designed for brittle materials at high pressures and strain rates, such as the Johnson-Holmquist 2, JH-2 model [90]. Figure 9.1 shows the promise of the JH-2 model for modeling the behavior of tungsten carbide when compared to experimental observations in PSPI experiment CK-1806. The added complexity of this material description requires a sustained effort to accurately predict the response of tungsten carbide, but could, once calibrated for different experimental conditions, enable a more detailed inference of sample properties.

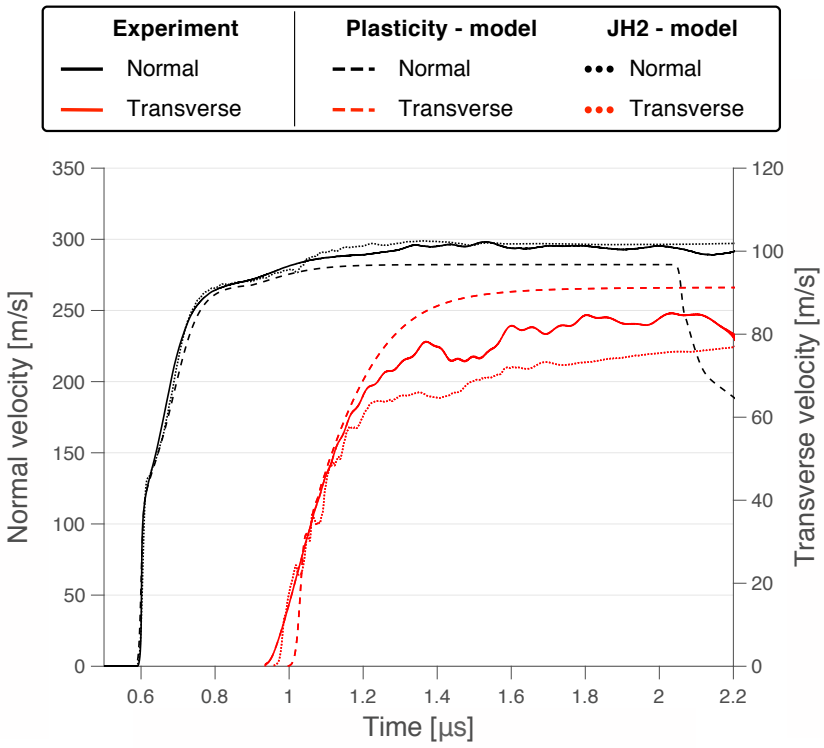

Figure 9.1: Comparison of normal and transverse velocity profiles obtained from velocimetry measurements during PSPI experiment CK-1806 with numerical results of the previously described plasticity approach and a JH-2 constitutive model.

BIBLIOGRAPHY

[1] D.R. Schmitt and T.J. Ahrens. “Shock temperatures in silica glass: Implications for modes of shock-induced deformation, phase transformation, and melting with pressure”. In: *Journal of Geophysical Research: Solid Earth* 94 (1989), pp. 5851–5871.

[2] S.J. Tracy, S.J. Turneaure, and T.S. Duffy. “In situ X-Ray diffraction of shock-compressed fused silica”. In: *Physical Review Letters* 120 (2018), p. 135702.

[3] S.E. Grunschel. “Pressure-shear plate impact experiments on high-purity aluminum at temperatures approaching melt”. PhD thesis. Brown University, 2009.

[4] E.B. Zaretsky and G.I. Kanel. “Effect of temperature, strain, and strain rate on the flow stress of aluminum under shock-wave compression”. In: *Journal of Applied Physics* 112 (2012), p. 073504.

[5] W.A. Spitzig and O. Richmond. “The effect of pressure on the flow stress of metals”. In: *Acta metallurgica* 32 (1984), pp. 457–463.

[6] A.E. Gleason et al. “Ultrafast visualization of crystallization and grain growth in shock-compressed SiO 2”. In: *Nature communications* 6 (2015), p. 8191.

[7] M. Dietenberger, M. Buyuk, and C. Kan. *Development of a high strain-rate dependent vehicle model*. National crash analysis center Virginia, Bamberg. 2005.

[8] T.D. Marusich and M. Ortiz. “Modelling and simulation of high-speed machining”. In: *International Journal for Numerical Methods in Engineering* 38 (1995), pp. 3675–3694.

[9] W. Tong, R.J. Clifton, and S. Huang. “Pressure-shear impact investigation of strain rate history effects in oxygen-free high-conductivity copper”. In: *Journal of the Mechanics and Physics of Solids* 40 (1992), pp. 1251–1294.

[10] S.H. Glenzer et al. “Symmetric inertial confinement fusion implosions at ultra-high laser energies”. In: *Science* 327 (2010), pp. 1228–1231.

[11] Z.M. Sternberger. “Determining strength of materials under dynamic loading conditions using hydrodynamic instabilities”. PhD thesis. California Institute of Technology, 2017.

[12] J.R. Asay and J. Lipkin. “A self-consistent technique for estimating the dynamic yield strength of a shock-loaded material”. In: *Journal of Applied Physics* 49 (1978), pp. 4242–4247.

[13] A.S. Abou-Sayed, R.J. Clifton, and L. Hermann. “The oblique-plate impact experiment”. In: *Experimental Mechanics* 16 (1976), pp. 127–132.

[14] J.F. Barnes et al. “Taylor instability in solids”. In: *Journal of Applied Physics* 45 (1974), pp. 727–732.

[15] J.L. Brown et al. “Flow strength of tantalum under ramp compression to 250 GPa”. In: *Journal of Applied Physics* 115 (2014), p. 043530.

[16] Z. Rosenberg. “Review on lateral stress measurements with piezoresistive gauges”. In: *AIP Conference Proceedings*. Vol. 505. 2000, pp. 1033–1038.

[17] W.D. Reinhart et al. *Pressure-shear experiments on granular materials*. Tech. rep. Sandia National Laboratories, 2011.

[18] N.K. Bourne and Z. Rosenberg. “The dynamic response of soda-lime glass”. In: *AIP Conference Proceedings*. Vol. 370. 1996, pp. 567–572.

[19] G.J. Kleiser, L.C. Chhabildas, and W.D. Reinhart. “Comparison of dynamic compression behavior of single crystal sapphire to polycrystalline alumina”. In: *International Journal of Impact Engineering* 38 (2011), pp. 473–479.

[20] W.D. Reinhart, L.C. Chhabildas, and T.J. Vogler. “Investigating phase transitions and strength in single-crystal sapphire using shock–reshock loading techniques”. In: *International journal of impact engineering* 33 (2006), pp. 655–669.

[21] J.R. Asay, L.C. Chhabildas, and D.P. Dandekar. “Shear strength of shock-loaded polycrystalline tungsten”. In: *Journal of Applied Physics* 51 (1980), pp. 4774–4783.

[22] H. Huang and J.R. Asay. “Reshock and release response of aluminum single crystal”. In: *Journal of Applied Physics* 101 (2007), p. 063550.

[23] T.J. Vogler, T. Ao, and J.R. Asay. “High-pressure strength of aluminum under quasi-isentropic loading”. In: *International Journal of Plasticity* 25 (2009), pp. 671–694.

[24] S. Sundaram. “Pressure-shear plate impact studies of alumina ceramics and the influence of an intergranular glassy phase”. PhD thesis. Brown University, 1998.

[25] S. Sundaram. “Shearing resistance of ceramic powder under high pressures and high shear rates”. PhD thesis. Brown University, 1994.

[26] R.J. Clifton and T. Jiao. “Pressure and Strain-Rate Sensitivity of an Elastomer: (1) Pressure-Shear Plate Impact Experiments; (2) Constitutive Modeling”. In: *Elastomeric polymers with high rate sensitivity: applications in blast, shock-wave, and penetration mechanics*. Ed. by R.G. Barsoum. William Andrew, 2015, pp. 17–65.

[27] K.T. Ramesh and R.J. Clifton. “A pressure-shear plate impact experiment for studying the rheology of lubricants at high pressures and high shearing rates”. In: *Journal of Tribology* 109 (1987), pp. 215–222.

[28] D.P. Dandekar and D.E. Grady. “Shock equation of state and dynamic strength of tungsten carbide”. In: *AIP Conference Proceedings*. Vol. 620. 2002, pp. 783–786.

[29] C.S. Alexander. *Dynamic response of soda-lime glass*. Tech. rep. Sandia National Lab.(SNL-NM), Albuquerque, NM (United States), 2007.

[30] T. Deschamps et al. “Elastic moduli of permanently densified silica glasses”. In: *Scientific reports* 4 (2014), p. 7193.

[31] Y. Liang, C.R. Miranda, and S. Scandolo. “Mechanical strength and coordination defects in compressed silica glass: Molecular dynamics simulations”. In: *Physical review B* 75 (2007), p. 024205.

[32] J. Wackerle. “Shock-wave compression of quartz”. In: *Journal of Applied Physics* 33 (1962), pp. 922–937.

[33] R. Yang and Z. Wu. “Elastic properties of stishovite and the CaCl2-type silica at the mantle temperature and pressure: An ab initio investigation”. In: *Earth and Planetary Science Letters* 404 (2014), pp. 14–21.

[34] A.R. Oganov, M.J. Gillan, and G.D. Price. “Structural stability of silica at high pressures and temperatures”. In: *Physical Review B* 71 (2005), p. 064104.

[35] H. Aramberri, R. Rurali, and J. Íñiguez. “Thermal conductivity changes across a structural phase transition: The case of high-pressure silica”. In: *Physical Review B* 96 (2017), p. 195201.

[36] S.M. Stishov and S.V. Popova. “A new dense modification of silica”. In: *Geochemistry* 10 (1961), pp. 923–926.

[37] D.E. Grady. “Shock deformation of brittle solids”. In: *Journal of Geophysical Research: Solid Earth* 85 (1980), pp. 913–924.

[38] A.V. Anan’in et al. “The effect of shock waves on silicon dioxide. I. Quartz”. In: *Combustion, Explosion and Shock Waves* 10 (1974), pp. 372–379.

[39] A.E. Gleason et al. “Time-resolved diffraction of shock-released SiO 2 and diaplectic glass formation”. In: *Nature communications* 8 (2017), p. 1481.

[40] Y. Shen et al. “Nanosecond homogeneous nucleation and crystal growth in shock-compressed SiO_2”. In: *Nature materials* 15 (2016), p. 60.

[41] S.R. Shieh, T.S. Duffy, and B. Li. “Strength and elasticity of SiO2 across the stishovite–CaCl2-type structural phase boundary”. In: *Physical Review Letters* 89 (2002), p. 255507.

[42] M. Millot et al. “Shock compression of stishovite and melting of silica at planetary interior conditions”. In: *Science* 347 (2015), pp. 418–420.

[43] C. Meade and R. Jeanloz. “Effect of a coordination change on the strength of amorphous SiO2”. In: *Science* 241 (1988), pp. 1072–1074.

[44] W. Schill et al. “The anomalous yield behavior of fused silica glass”. In: *Journal of the Mechanics and Physics of Solids* 113 (2018), pp. 105–125.

[45] G.I. Kanel, A.M. Molodets, and A.N. Dremin. “Investigation of singularities of glass strain under intense compression waves”. In: *Combustion, Explosion and Shock Waves* 13 (1977), pp. 772–777.

[46] R.J. Clifton. “Analysis of failure waves in glasses”. In: *Applied Mechanics Reviews* 46 (1993), pp. 540–546.

[47] N.K. Bourne, Z. Rosenberg, and J.E. Field. “High-speed photography of compressive failure waves in glasses”. In: *Journal of Applied Physics* 78 (1995), pp. 3736–3739.

[48] R.J. Clifton, M. Mello, and N.S. Brar. “Effect of shear on failure waves in soda lime glass”. In: *AIP Conference Proceedings*. Vol. 429. 1998, pp. 521–524.

[49] C. Hari Manoj Simha and Y.M. Gupta. “Time-dependent inelastic deformation of shocked soda-lime glass”. In: *Journal of Applied Physics* 96 (2004), pp. 1880–1890.

[50] D.E. Grady and L.C. Chhabildas. *Shock-wave properties of soda-lime glass*. Tech. rep. Sandia National Labs., Albuquerque, NM (United States), 1996.

[51] A.A. Wereszczak and C.E. Anderson Jr. “Borofloat and starphire float glasses: A comparison”. In: *International Journal of Applied Glass Science* 5 (2014), pp. 334–344.

[52] G.E. Duvall and R.A. Graham. “Phase transitions under shock-wave loading”. In: *Reviews of Modern Physics* 49 (1977), p. 523.

[53] S. Plimpton. “Fast parallel algorithms for short-range molecular dynamics”. In: *Journal of Computational Physics* 117 (1995), pp. 1–19.

[54] E.J. Reed et al. *A multi-scale approach to molecular dynamics simulations of shock waves*. Lawrence Livermore National Laboratory (LLNL), Livermore, CA (United States). 2004.

[55] M. Grujicic et al. “Densification and devitrification of fused silica induced by ballistic impact: a computational investigation”. In: *Journal of Nanomaterials* 16 (2015), p. 167.

[56] K. Kadau et al. “Microscopic view of structural phase transitions induced by shock waves”. In: *Science* 296 (2002), pp. 1681–1684.

[57] B.W.H. Van Beest, G. J. Kramer, and R.A. Van Santen. “Force fields for silicas and aluminophosphates based on ab initio calculations”. In: *Physical Review Letters* 64 (1990), p. 1955.

[58] R.W. Hockney and J.W. Eastwood. *Computer simulation using particles*. 1988.

[59] E.J. Reed, L.E. Fried, and J.D. Joannopoulos. “A method for tractable dynamical studies of single and double shock compression”. In: *Physical Review Letters* 90 (2003), p. 235503.

[60] K. Vollmayr, W. Kob, and K. Binder. “Cooling-rate effects in amorphous silica: A computer-simulation study”. In: *Physical Review B* 54 (1996), p. 15808.

[61] P. Kumar and R.J. Clifton. “Optical alignment of impact faces for plate impact experiments”. In: *Journal of Applied Physics* 48 (1977), pp. 1366–1367.

[62] C. Kettenbeil et al. “Heterodyne transverse velocimetry for pressure-shear plate impact experiments”. In: *Journal of Applied Physics* 123 (2018), p. 125902.

[63] R.W. Klopp, R.J. Clifton, and T.G. Shawki. “Pressure-shear impact and the dynamic viscoplastic response of metals”. In: *Mechanics of Materials* 4 (1985), pp. 375–385.

[64] K.S. Kim, R.J. Clifton, and P. Kumar. “A combined normal- and transverse-displacement interferometer with an application to impact of *y*-cut quartz”. In: *Journal of Applied Physics* 48 (1977), pp. 4132–4139.

[65] L.C. Chhabildas, H.J. Sutherland, and J.R. Asay. “A velocity interferometer technique to determine shear-wave particle velocity in shock-loaded solids”. In: *Journal of Applied Physics* 50 (1979), p. 5196.

[66] J. Wang, N.R. Sottos, and R.L. Weaver. “Mixed-mode failure of thin films using laser-generated shear waves”. In: *Experimental Mechanics* 43 (2003), pp. 323–330.

[67] C.S. Alexander, J.R. Asay, and T.A. Haill. “Magnetically applied pressure-shear: A new method for direct measurement of strength at high pressure”. In: *Journal of Applied Physics* 108 (2010), p. 126101.

[68] B. Zuanetti, T. Wang, and V. Prakash. “A compact fiber optics-based heterodyne combined normal and transverse displacement interferometer”. In: *Review of Scientific Instruments* 88 (2017), p. 033108.

[69] D.H. Dolan. “Accuracy and precision in photonic Doppler velocimetry”. In: *Review of Scientific Instruments* 81 (2010), p. 053905.

[70] T. Strand et al. “Factors to consider when choosing a probe for PDV”. In: *3rd Annual PDV Conference*. 2008.

[71] Anthony E. Siegman. *Lasers*. 1986.

[72] M. Mello et al. “Heterodyned fiber-optic PDV using diffracted beams for combined measurement of transverse and normal particle velocities in plate impact experiments”. In: *Shock Compression of Condensed Matter - 2017*. 2018.

[73] G. Walze. PhD thesis. Albert-Ludwigs-Universität Freiburg, 2005.

[74] D Gabor. “Theory of communication”. In: *Journal of the Institution of Electrical Engineers* 93 (1946), pp. 429–441.

[75] J.N. Johnson. “Shock propagation produced by planar impact in linearly elastic anisotropic media”. In: *Journal of Applied Physics* 42 (1971), pp. 5522–5530.

[76] P. Heyliger, H. Ledbetter, and S. Kim. “Elastic constants of natural quartz”. In: *The Journal of the Acoustical Society of America* 114 (2003), pp. 644–650.

[77] B.J. Jensen et al. “Accuracy limits and window corrections for photon Doppler velocimetry”. In: *Journal of Applied Physics* 101 (2007), p. 013523.

[78] M.H. Montgomery and D. O’Donoghue. “A derivation of the errors for least squares fitting of time series data”. In: *Delta Scuti Star Newsletter, NASA Astrophysics Data System* 13 (1999), p. 28.

[79] D.H. Dolan and T. Ao. *Release notes for SIRHEN version 0.4*. 2010.

[80] ASM International. Handbook Committee. *ASM Handbook: Mechanical testing and evaluation*. 2000.

[81] A. S. Abou-Sayed and R. J. Clifton. “Analysis of combined pressure-shear waves in an elastic/viscoplastic material”. In: *Journal of Applied Mechanics* 44 (1977), pp. 79–84.

[82] L.C. Chhabildas and J.W. Swegle. “Dynamic pressure-shear loading of materials using anisotropic crystals”. In: *Journal of Applied Physics* 51 (1980), pp. 4799–4807.

[83] B.W. Reed et al. “A unified approach for extracting strength information from nonsimple compression waves. Part I: Thermodynamics and numerical implementation”. In: *Journal of Applied Physics* 110 (2011), p. 113505.

[84] Rodney J. Clifton. Personal communication. 2018.

[85] Livermore Software Technology Corporation. *LS-DYNA keyword user’s manual*. 2016.

[86] T. Klünsner et al. “Effect of microstructure on fatigue properties of WC-Co hard metals”. In: *Procedia Engineering* 2 (2010), pp. 2001–2010.

[87] G.R. Johnson and W.H. Cook. “A constitutive model and data for metals subjected to large strains, strain rates, and high pressures”. In: *Proceedings of the 7th International Symposium On Ballistics*. 1983.

[88] J.W. Swegle and D.E. Grady. “Shock viscosity and the prediction of shock wave rise times”. In: *Journal of applied physics* 58 (1985), pp. 692–701.

[89] D. Steinberg et al. *Equation of state and strength properties of selected materials*. 1996.

[90] G.R. Johnson and T.J. Holmquist. “A computational constitutive model for brittle materials subjected to large strains, high strain rates and high pressures”. In: *Shock Wave and High-Strain-Rate Phenomena in Materials* (1992), pp. 1075–1081.

[91] J. Shen et al. “Stress relaxation of a soda lime silicate glass below the glass transition temperature”. In: *Journal of Non-Crystalline Solids* 324 (2003), pp. 277–288.

[92] Michael F Ashby. *Materials and the environment: eco-informed material choice*. 2012.

[93] W. Chen and G. Ravichandran. “Failure mode transition in ceramics under dynamic multiaxial compression”. In: *International Journal of Fracture* 101 (2000), pp. 141–159.

[94] D.E. Grady. “Shock-wave compression of brittle solids”. In: *Mechanics of Materials* 29 (1998), pp. 181–203.

[95] D.B. Hayes and R.A. Graham. “Yielding of shock-loaded x-cut quartz”. In: *Bulletin of the American Physical Society*. Vol. 23. 1978, pp. 70–70.

[96] T.J. Holmquist et al. *High strain rate properties and constitutive modeling of glass*. Sandia National Laboratories, Albuquerque, NM (United States). 1995.

[97] H.D. Espinosa. “Dynamic compression-shear loading with in-material interferometric measurements”. In: *Review of scientific instruments* 67 (1996), pp. 3931–3939.